

DETERMINING CRUSTAL THICKNESS BENEATH THE TRANSANTARCTIC
MOUNTAINS AND THE WILKES SUBGLACIAL BASIN USING
S-WAVE RECEIVER FUNCTIONS

by

LINDSEY METCALF KENYON

SAMANTHA E. HANSEN, COMMITTEE CHAIR

ANDREW M. GOODLIFFE

ANDREW A. NYBLADE

DELORES M. ROBINSON

A THESIS

Submitted in partial fulfillment of the requirements
for the degree of Master of Science in the
Department of Geological Sciences
in the Graduate School of
The University of Alabama

TUSCALOOSA, ALABAMA

2014

Copyright Lindsey Metcalf Kenyon 2014
ALL RIGHTS RESERVED

ABSTRACT

The Transantarctic Mountains (TAMs) are a ~4,000 km long mountain range, with elevations up to 4,500 m, which separate East and West Antarctica. Given the lack of compressional structures in the TAMs, the origin for these mountains is unclear, and many possible uplift mechanisms have been suggested. The formation of the Wilkes Subglacial Basin (WSB), which is situated inland and parallel to the TAMs, has also been widely debated. A key characteristic to distinguish between different origin models for the TAMs and the WSB is the thickness of the crust beneath these areas. A new 15-station seismic array deployed in the northern TAMs, called the Transantarctic Mountains Northern Network (TAMNNET), as well as 5 stations operated by the Korean Polar Research Institute (KOPRI), are used to investigate the crustal structure beneath a previously unexplored portion of the TAMs and the WSB. Data from the combined TAMNNET and KOPRI networks are analyzed using S-wave receiver functions (SRFs) to estimate the crustal thicknesses. Using both the timing of the conversion from the crust-mantle interface obtained with the SRFs and Rayleigh wave phase velocities, a grid search procedure is used to determine the crustal thickness and velocity beneath each station. Results indicate that the crust is 12-27 km thick near the Ross Sea coast, increasing to a maximum thickness of ~47 km beneath some portions of the TAMs. Further inland, beneath the East Antarctic craton and the WSB, the crust has an average thickness of ~42 km. Average crustal S-wave velocities range from 3.3-3.8 km/s, with the slowest velocities near the coast. These results support a flexural origin model, which jointly explains the uplift of the TAMs and the down-

warp of the WSB. Small variations in the crustal thickness may contribute to locally high topography, but crustal isostasy does not appear to play a major role in the overall support of the TAMs.

DEDICATION

This thesis is dedicated first to my parents, who push me to work hard but are always there if I ever need someone to fall back on. Second, to my friends and family who have encouraged and challenged me. And third to all the great teachers and advisors I've had through high school, undergraduate, and graduate school who have taught me how to challenge myself and achieve more than I thought I was capable of as a student and scientist.

LIST OF ABBREVIATIONS AND SYMBOLS

EA	East Antarctic
h	Height of extra elevation
KOPRI	Korean Polar Research Institute
PRFs	P-wave receiver functions
SRFs	S-wave receiver functions
T	Thickness of crust root
TAMNNET	Transantarctic Mountains Northern Network
TAMSEIS	Transantarctic Mountains Seismic Experiment
TAMs	Transantarctic Mountains
WARS	West Antarctic Rift system
WSB	Wilkes Subglacial Basin
ρ_c	Density of the crust
ρ_m	Density of the upper mantle
=	Equal to
*	Multiplied by
/	Divided by
<	Less than
>	Greater than
~	Approximately

ACKNOWLEDGMENTS

Thank you to my advisor, Sam Hansen, who is not only the best advisor imaginable, but who also is the hardest working, most kick-ass person I know. It would not have been possible for me to do this project (or complete it so soon) without her. Thanks to Jordan Graw for all the help, advice, conversations, time in the lab, and time in the field. I could not have done this project without the help of Brian DuBay, Doug Bloomquist, Paul Carpenter, and Yongcheol Park in Antarctica.

I am grateful to have received funding from Teaching Assistantships in the Department of Geological Sciences at The University of Alabama, from the Graduate Council Fellowship at The University of Alabama, and from Research Assistantships funded by the National Science Foundation.

Thank you to my family, friends, Will Weiner, former and current teachers/professors, and everyone in the Department of Geological Sciences at The University of Alabama. I appreciate your help, guidance, enthusiasm, and companionship, as it is what keeps me going on a daily basis.

CONTENTS

ABSTRACT	ii
DEDICATION	iv
LIST OF ABBREVIATIONS AND SYMBOLS	v
ACKNOWLEDGMENTS	vi
LIST OF TABLES	ix
LIST OF FIGURES	x
1.0 INTRODUCTION	1
2.0 BACKGROUND	5
2.1 Tectonic and Geologic History of Antarctica	5
2.2 Proposed Uplift Mechanisms for the TAMs	8
2.3 Proposed Formation and Structure of the Wilkes Subglacial Basin	11
3.0 DATA AND METHODS	13
3.1 Receiver Functions	14
3.2 Employed SRF technique	16
3.3 Estimating Ice Thickness	19
3.4 Estimating Crustal Thickness	21
3.5 Evaluating Additional Uncertainty	24
4.0 RESULTS	25
4.1 Ice Thicknesses	25

4.2 KOPRI Rock Stations	26
4.3 TAMNNET Ice Stations	31
4.4 Crustal S-wave Velocity	38
5.0 DISCUSSION.....	41
5.1 Crustal Thicknesses and Isostatic Compensation	41
5.2 TAMs Uplift Models and Formation of the WSB	43
5.3 Average Crustal Shear Velocities	46
5.4 Broader Significance.....	47
5.4.1 Comparison to Continental-scale Antarctic Models	47
5.4.2 Comparison to Other Cratonic Environments.....	48
6.0 CONCLUSIONS.....	50
REFERENCES	53
APPENDIX A.....	59
APPENDIX B.....	73

LIST OF TABLES

Table 1. Ice thicknesses 26

Table 2. Initial crustal shear velocities and crustal thicknesses..... 29

Table 3. Revised crustal shear velocities and crustal thicknesses 39

LIST OF FIGURES

Figure 1. Map of the TAMNNET and KOPRI stations	4
Figure 2. Simplified geologic history	7
Figure 3. TAMs uplift models	9
Figure 4. Crustal thickness from TAMSEIS.....	11
Figure 5. PRF and SRF conversion cartoon.....	15
Figure 6. Map of events used in SRFs	17
Figure 7. Profile lines of the TAMNNET and KOPRI stations.....	18
Figure 8. Stacked SRFs.....	19
Figure 9. Stacked PRFs.....	21
Figure 10. Data modeling and grid search results.....	23
Figure 11. KOPRI data from PRFs.....	30
Figure 12. Revised KP04 SRF stack.....	31
Figure 13. Moho topography along 5 profiles	33-37
Figure 14. Map of average crustal shear velocities.....	40

1.0 INTRODUCTION

Given its remote location and extreme weather conditions, Antarctica is a vastly unexplored continent. Its geology and tectonic history are difficult to determine since most of Antarctica is covered by large ice sheets. The few rock exposures that do exist are around the edges of the continent and in the Transantarctic Mountains (TAMs), a ~4,000 km long boundary between East and West Antarctica (Fig. 1, Robinson and Splettstoesser, 1984). The TAMs reach elevations of up to 4,500 m, making them comparable in both length and elevation to the Rocky Mountains (Enright, 2010). However, unlike most mountain ranges of this size, the TAMs were not formed in a compressional environment. Evidence shows that the uplift of the TAMs dates to ~55 Ma (Fitzgerald et al., 1986); however, the stratigraphic layers within the TAMs pre-date this uplift and remain nearly horizontal (Fitzgerald et al., 1986). Further inland, the Wilkes Subglacial Basin (WSB) is a depression that runs parallel to the TAMs (Drewry, 1976), and the formation of this feature also remains elusive. A variety of mechanisms have been proposed to explain the origin of the TAMs and the WSB, but additional observations are needed to further investigate their corresponding structure. Specifically, the crustal structure beneath the TAMs and the WSB, which can be estimated with geophysical approaches like gravity, magnetism, and seismology in particular, is key to differentiating between formation mechanisms associated with these tectonic features.

Previous seismic investigations of the TAMs have primarily been focused in the vicinity of Ross Island, in the central portion of the mountain range. For example, data from the

Transantarctic Mountains Seismic Experiment (TAMSEIS; Fig. 1), which operated between 2000 and 2003, have been analyzed with a variety of techniques to examine the structure beneath this area. However, even using the same data set, different TAMSEIS studies came to different conclusions about the crustal structure beneath the TAMs and the WSB and about which origin model is most plausible (*e.g.*, Lawrence et al., 2006a; Hansen et al., 2009). Further, along-strike investigations of the structure beneath the TAMs and WSB are needed to clarify the geologic processes associated with these features and how they relate to the overall tectonic history of Antarctica. Additionally, Antarctica is often used as a proxy for understanding global climate change. The history and behavior of Antarctica's ice sheets are closely linked to its tectonic structure. Those who study the cryosphere can use the crustal thickness estimates from the current work to help model future interactions between the crust and the ice sheet and to illuminate what impacts global climate change might have.

A central contention between origin models is whether or not the TAMs are underlain by thick crust (*i.e.* a crustal root) and how significant isostatic compensation is in supporting their uplift and elevation. To estimate crustal thickness, receiver functions are often employed. P-wave receiver functions (PRFs) are a common seismic method used to determine the depth to and velocity change across layers within the earth, such as the crust-mantle interface (Zhu and Kanamori, 2000). P-to-S wave conversions from such layers can be modeled to determine the corresponding crustal structure (Langston, 1977; 1979; Ammon et al., 1990; 1991). However, when a low velocity surface layer, such as ice, is present, the PRF signal of interest from discontinuities at depth can be masked by reverberations and noise within that slow layer (Zelt and Ellis, 1999; Julia et al., 2004; Kumar et al., 2005). In these cases, S-wave receiver functions (SRFs), which model S-to-P wave conversions from discontinuities at depth (Farra and Vinnik,

2000; Li et al., 2004; Hansen et al., 2009), are favorable. The time difference between the conversions of interest and reverberations in the slow surface layer make SRFs well-suited to imaging deeper structure.

To expand the investigation beneath the TAMs and the WSB, this study uses the SRF approach to estimate crustal thickness. Data are from a new seismic array called the Transantarctic Mountains Northern Network (TAMNNET, Fig. 1), which was deployed in November-December 2012, and from five stations operated by the Korean Polar Research Institute (KOPRI). These two networks provide seismic coverage of a previously unexplored portion of the northern TAMs and the WSB. Using a grid search procedure (Last et al., 1997), different velocity models are constructed to match the timing of S-to-P wave conversions from the crust-mantle interface beneath each station. The models are further constrained by Rayleigh wave phase velocities modeled using the TAMNNET data (Graw et al., 2014). Crustal thickness estimates beneath the northern TAMs will help elucidate whether a crustal root is present beneath the mountain range and whether there are any along-strike variations to the crustal structure between the central and northern TAMs. As part of this study, ice thicknesses and average crustal S-wave velocities are also determined. Combined with previous results from TAMSEIS, this study provides a cohesive set of evidence that constrains the origin models for the TAMs and the WSB.

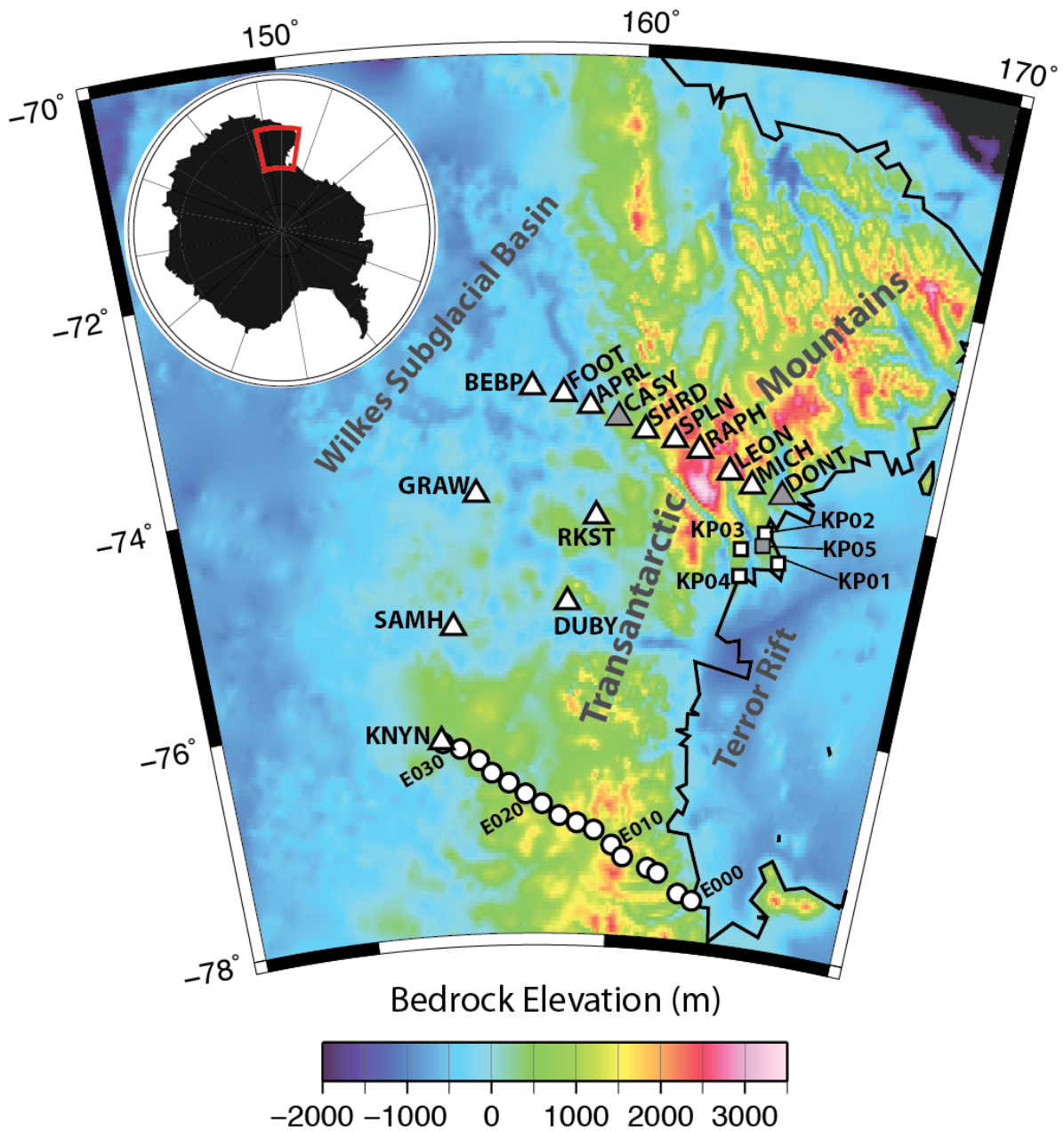


Figure 1. Map of the TAMNNET and KOPRI seismic stations. TAMNNET stations are shown as triangles, and KOPRI stations are shown as squares. For reference, stations along the E-W TAMSEIS profile are also shown (circles). Shapes with grey centers denote stations with poor signal-to-noise ratios, which were not analyzed. Bedrock elevations are from BEDMAP2 (Fretwell et al., 2013).

2.0 BACKGROUND

2.1 Tectonic and Geologic History of Antarctica

The tectonic history of Antarctica is an important part of global tectonic understanding; however, due to limited rock exposure from beneath the ice cap, discerning Antarctica's tectonic evolution has been difficult. Antarctica is central to the supercontinent reconstructions of both Rodinia (~750 Ma) and Pangaea (~250 Ma; Torsvik, 2003). In Meert (2003) and Torsvik (2003), the East Antarctic (EA) craton was attached to Australia and India through both supercontinent assemblages. East Antarctica's position within Gondwanaland (~550 Ma) is fairly well established. Australia, India, and Africa surrounded the outer edges of the EA craton and left behind rifted margins after separation (Fitzgerald, 2002). However, the opposite side of the EA craton, where the TAMs and West Antarctica eventually formed, is poorly constrained in terms of the number and timing of accretions as well as the positions of various micro-plates (Fitzgerald, 2002). There is evidence for East Antarctica acting as the overriding plate of a subduction zone during the Cambrian Ross Orogeny (~500 Ma; Federico et al., 2009). This boundary moved seaward with the accretion of terranes and transpression in the Paleozoic (Fitzgerald, 2002). Many of the micro-plates reorganized into modern day West Antarctica.

Extension in the West Antarctic Rift System (WARS) is thought to have initiated in the Cretaceous (~100 Ma; ten Brink et al., 1997; Fitzgerald, 2002). In part of the WARS, under the Ross Sea and the Ross Ice Shelf, there are several basins of similar but various depositional histories (Salvini et al., 1997). Generally, these basins indicate extension over a wide area

starting in the Late Cretaceous, followed by a second stage of focused extension in the Late Paleogene. This area of later extension is known as the Terror Rift, and it lies adjacent to the TAMs (Huerta and Harry, 2007). The Terror Rift terminates in active volcanoes at both ends, with Mt. Erebus to the south and Mt. Melbourne to the north (Storti et al., 2008).

The geologic history of the TAMs is inferred from various outcrops, particularly in the McMurdo Dry Valleys region. The oldest stratigraphy is Precambrian igneous and metamorphic rocks from the Beardmore Orogeny (Fig. 2; ten Brink et al., 1997). Cambrian meta-sedimentary rocks unconformably overlie the Precambrian rocks and are intruded by Cambrian-Ordovician syn- to post-tectonic granites from the Ross Orogeny, which were emplaced in the over-riding plate of the subduction zone that paralleled the present-day TAMs (Federico et al., 2009).

Erosion of these basement rocks, starting in the Ordovician and ending in the Devonian, created a distinct horizontal erosional surface called the Kukri Peneplain (Fitzgerald, 1986). Above this unconformity is a Devonian to Triassic sedimentary sequence called the Beacon Supergroup, which was deposited over an area centered on the present day TAMs (Fitzgerald, 1986). The sediments indicate a Devonian passive margin, followed by an upper Carboniferous-Triassic foreland basin (Fig. 2, Fitzgerald, 1986; Fitzgerald, 2002; Bialas et al., 2007). The Beacon Supergroup and basement are intruded by Jurassic dolerite dikes and sills and are overlain by basalt flows (Fitzgerald, 1986). The sills generally intruded parallel to the Kukri Peneplain (Fitzgerald, 1986). The peneplain, Jurassic sills and basalts, and the flat-lying Beacon sediments can therefore be used as an indicator of post-Jurassic tectonic movement. This Jurassic paleo-surface was buried up to ~4 km between 180 Ma and at least 80 Ma (Lisker and Laufer, 2013). There is a gap in the geologic record between ~136 Ma (Fig. 2) until the eruption of alkaline volcanic rock, which can be dated to 19 Ma (Fitzgerald, 1986). The Kukri Peneplain and the

sediments of the Beacon Supergroup show no evidence of folding or reverse faulting associated with a compressional mountain range. Today, the Kukri Peneplain is nearly horizontal, with a gentle dip to the west, away from the coast (Fitzgerald, 1986).

Era	Period	Age (10 ⁶ years)	Duration	Events
Cenozoic	Q	2		Cenozoic volcanism
	T			Uplift of Transantarctic Mountains
Mesozoic	K	65		Ferrar intrusions, tholeiites
	J	136		Gondwana event
	Tr	190		
	P	225		
Paleozoic	P	280		Deposition of Beacon Supergroup
	P	310		
	M	345		
	D	395		
	S	430		Kukri peneplain
	O	500		
	€	600		Ross Orogeny
		600		Beardmore Orogeny
Pre-cambrian	p€	1000		"Nimrod Orogeny"
		2500		

Figure 2. Simplified geologic-tectonic history of the central TAMs from Kalamarides et al. (1987).

2.2 Proposed Uplift Mechanisms for the TAMs

The large gap in the geologic record during the time when the TAMs formed has led to many questions about the amount and timing of deposition, uplift, and erosion associated with the formation of the mountains. Sediments in the Ross Sea are dated to ~30 Ma (Salvini et al., 1997), but a ~100 million year gap in the geologic record for the region remains. Therefore, other methods must be utilized to obtain uplift ages for the TAMs. For example, apatite fission track dating indicates that the uplift of the TAMs started by ~55 Ma and that some areas near the coast were uplifted by as much as ~6 km (Fitzgerald, 1986; 1992). This ~6 km uplift estimate is supported by evidence that the Kukri Peneplain was buried at ~4 km depth at 80 Ma (Lisker and Laufer, 2013) but can currently be found at elevations 500-4,000 m above sea level (Fitzgerald, 1986).

Numerous models have been proposed to explain how and why the TAMs were uplifted (Fig. 3). Fitzgerald (1986) suggested passive rifting in a simple shear regime with a shallow crustal penetrative detachment zone. The westward-dipping, asymmetrical detachment fault would have various depths of extensional strain that would jointly explain the uplift of the TAMs and the rifting and subsidence in the adjacent Ross Sea. Stern and ten Brink (1989) modeled a steep fault, dipping in the opposite direction and argued for a stress-free, decoupled edge of flexure along the East Antarctic plate (Fig. 3a). Flexure along an uplifted free edge can also be used to explain the presence of the WSB (Stern and ten Brink, 1989). In this model, the free edge of the plate is supported by a buoyant thermal load from hotter than normal mantle beneath the WARS, and uplift would subsequently be enhanced by erosion and Vening-Meinesz isostasy. ten Brink and Stern (1992) modeled the flexure with lithospheric rigidity decreasing toward the coast, and ten Brink et al. (1997) attributed the decoupled edge of the plate to newly applied

trans-tensional motion from a plate motion reorganization, causing the plate to break and allowing the TAMs to uplift independently of the rifting in the WARS.

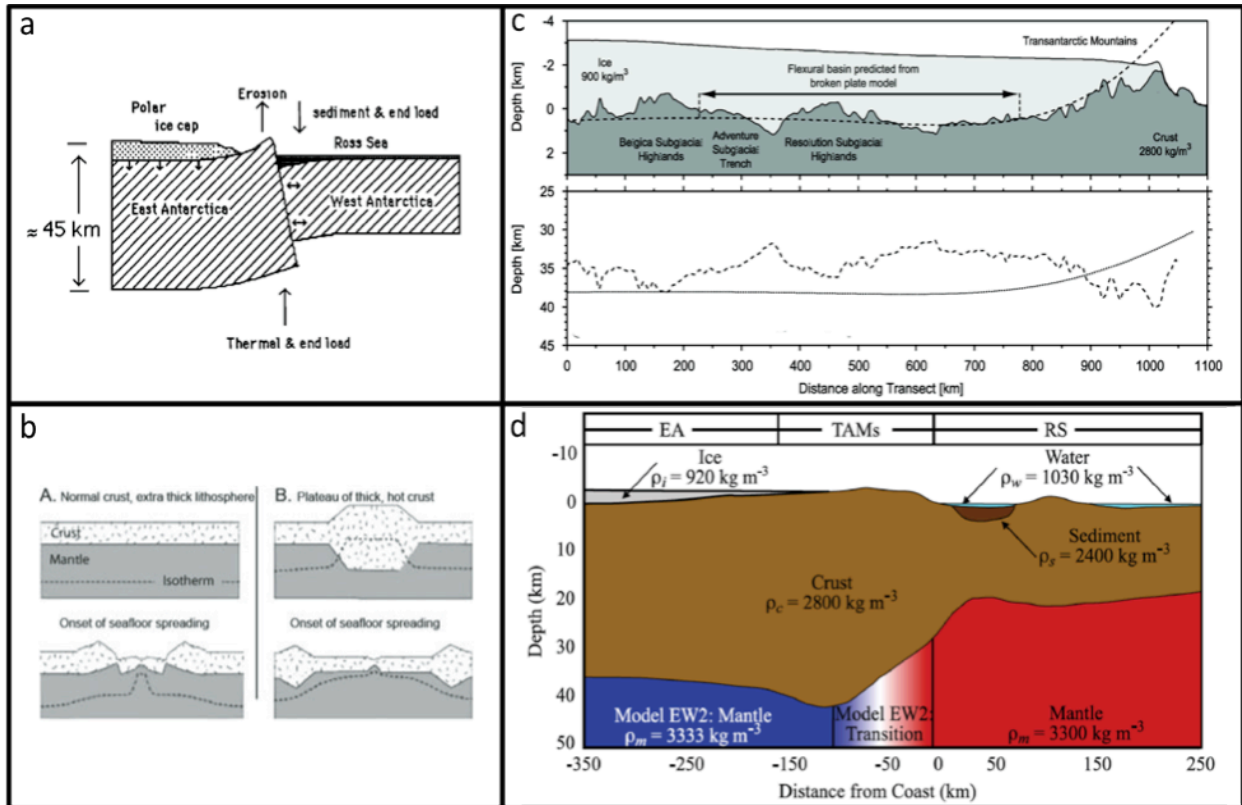


Figure 3. Various uplift models that have been proposed for the TAMs. (a) Stern and ten Brink (1989) flexural model. (b) Bialas et al. (2007) collapsed plateau model, with a ~5 km crustal root. (c) Studinger et al. (2004) gravity modeling, which requires a ~4 km crustal root. (d) Lawrence et al. (2006a) model, which includes a combination of a ~5 km root for isostasy, flexural uplift, and thermal support.

The thermal buoyancy and uplift associated with the flexure model is also supported by Smith and Drewry (1984). In their model, the EA craton moved over hot asthenosphere, causing phase changes in the upper mantle. Slow seismic velocities below West Antarctica are observed in many studies (*e.g.*, Banister et al., 2000; Ritzwoller et al., 2001; Morelli and Danesi, 2004; Watson et al., 2006; Lawrence et al, 2006b), and these slow velocities are attributed to a warm

upper mantle associated with rifting in the WARS. The source of the warm upper mantle has also been attributed to a mantle plume (Morelli and Danesi, 2004), in which case the slow velocities may not be consistent along the entire edge of the EA craton. Instead, this would suggest variability in the uplift mechanism along-strike in the TAMs. In contrast, Huerta and Harry (2007) contended that the heat and rifting in the WARS does not require a hotspot nor any trans-tensional motion, but rather the heat generated by thickened crust.

Seismic investigations using TAMSEIS data show that the slow velocities beneath West Antarctica extend ~50-100 km beneath the central TAMs before meeting faster velocity (colder and denser) upper mantle below East Antarctica (*e.g.*, Watson et al., 2006; Lawrence et al., 2006b). More recent studies show these slow velocities also likely extend beneath Victoria Land and the northern TAMs (Graw et al., 2014; Hansen et al., 2014).

Studinger et al. (2004) modeled an observed gravity profile and required a ~4 km crustal root beneath the TAMs to fit the data (Fig. 3c). They confirmed that such a root alone would not provide enough isostatic support for the TAMs and that erosional uplift would also be required. However, their model does not include the thermal load suggested by the flexure model (Studinger et al., 2004; Stern and ten Brink, 1989). Studinger et al. (2004) suggested the possibility of a collapsed plateau, which Bialas et al. (2007) also suggested as an explanation for the presence of a crustal root (Fig. 3b). Lawrence et al. (2006a) indicated a 5 km root beneath the central TAMs and invoked a combination of crustal isostasy, flexure support from warm upper mantle, and erosion to explain the TAMs uplift (Fig. 3d). In contrast, Hansen et al. (2009) indicated that there can only be a 2-3 km root beneath the central TAMs (Fig. 4), and this study favors flexure and thermal loading to explain the TAMs uplift since such a small root would contribute little isostatic compensation for the TAMs.

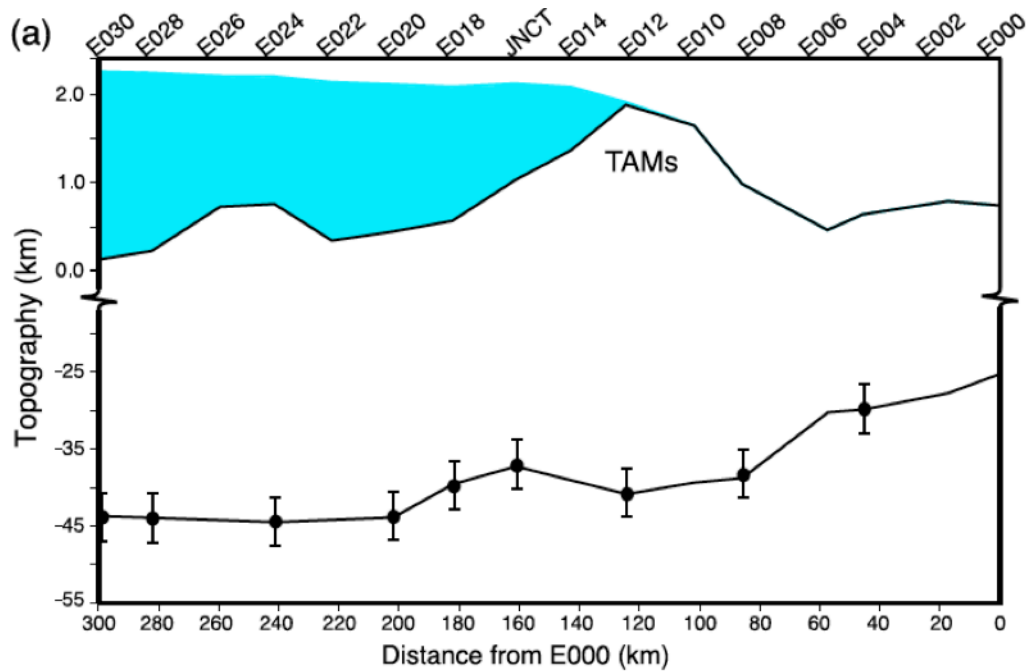


Figure 4. Crustal thickness estimates from Hansen et al. (2009) along the E-W TAMSEIS profile. The location of this profile is shown in Figure 1.

2.3 Proposed Formation and Structure of the Wilkes Subglacial Basin

The WSB is located on the inland side of the TAMs, parallel to the mountain range (Fig. 1). The width of the WSB changes from ~600 km at its north end to ~100 km at about 84° latitude (Ferraccioli et al., 2001). Much like the TAMs uplift, the structure and formation of the WSB and its relation to the TAMs has remained elusive. Stern and ten Brink (1989) suggested that the WSB is the inland down-warp of the crust associated with the flexure that uplifted the TAMs. This would mean the two features formed at the same time and that the WSB crustal thickness should be equal to or slightly thicker than the crust beneath the TAMs. ten Brink and Stern (1992) suggested that there is similar crustal thickness beneath both regions and that there

is no Cenozoic sedimentation in the WSB, indicating that it could not have been formed from a failure of the crust to rebound after partial ice cap melting.

More recent geophysical studies have proposed alternative ideas for the formation and structure of the WSB; specifically a structural, rather than a flexural, control for the formation of the basin. Ferraccioli et al. (2001) suggested the WSB is associated with extended or rifted crust with 1-4 km of sedimentary infill. Studinger et al. (2004) supported the idea of extended crust, citing gravitational evidence for thinner crust below the basin compared to the crust beneath the TAMs. However, contrary to Ferraccioli et al. (2001), Studinger et al. (2004) showed no evidence for sediments any thicker than 1 km in the WSB. Ferraccioli et al. (2009) continued to support the structural control of the basin and suggested the whole basin was part of the Ross Orogeny deformation belt, where a fold-and-thrust belt was subjected to back-arc rifting, resulting in thin crust (~31 km). This would mean the undeformed EA craton only exists at the far edge of the WSB, away from the TAMs.

The crustal thickness beneath the TAMs and WSB is a key constraint in determining which of the proposed origin models are most plausible. Differences in crustal thickness may contribute to uplift in the TAMs and the down-warp in the WSB. Previous seismic investigations (*e.g.*, Bannister et al., 2003; Watson et al., 2006; Lawrence et al., 2006a; 2006b; Hansen et al., 2009; Pyle et al., 2010) have only examined a small portion of these tectonic provinces, leading to uncertainties about the crustal structure beneath other sections of the WSB and the TAMs. The current study focuses on investigating the crustal structure beneath the northern TAMs and eastern WSB to assess along-strike variations and to determine which models best explain the observed structure.

3.0 DATA AND METHODS

To investigate the validity of the various origin models for the TAMs and the WSB, a new seismic array called TAMNNET was deployed in Victoria Land across the northern TAMs (Fig. 1). The TAMNNET array is supplemented by 5 stations, which are operated by KOPRI (Fig. 1). KOPRI stations KP01, KP02, and KP03 were deployed in late 2011. All the TAMNNET stations, along with KOPRI stations KP04 and KP05, were deployed in November-December 2012. TAMNNET stations DUBY, GRAW, and KNYN are instrumented with Guralp CMG-3T broadband seismometers, while KOPRI stations KP01, KP02, KP03, and KP04 have Nanometrics Trillium compact broadband seismometers. All other stations have Nanometrics Trillium 240 broadband seismometers.

Ten of the TAMNNET stations were deployed in a linear transect across the TAMs, starting near the coast ~50 km north of Mt. Melbourne and extending over the mountains and into the WSB (Fig. 1). One station (KNYN) reoccupies the former location of previously deployed station E030 from the TAMSEIS array. The four remaining TAMNNET stations were deployed to fill in the area between the current TAMNNET transect and the former E-W TAMSEIS transect (Fig. 1). Two stations (GRAW and SAMH) are located between the end of the TAMNNET transect and station KNYN, creating a profile along which an examination of the structure behind the TAMs can be made. Two additional stations (RKST and DUBY) are located about halfway between the coast and the most inland stations, providing a profile along-strike of the TAMs, in line with station SHRD on the TAMNNET transect (Fig. 1). The KOPRI stations

are positioned on and around Mt. Melbourne in Terra Nova Bay and are all within 40 km of the coast.

3.1 Receiver Functions

Receiver functions are widely used in seismology to identify subsurface interfaces between layers in the Earth (Langston, 1977, 1979; Ammon et al., 1990, 1991). Most commonly used are PRFs, which are computed using the arrival time of the original P-wave from an earthquake as well as the delayed arrivals of converted phases from the discontinuities of interest. The change in density and velocity between subsurface layers results in the transformation of one type of wave into another. At any particular interface (at a given depth), an incoming P-wave can be both transmitted as a continuing P-wave and can partially be converted to an S-wave. Since P-waves travel faster than S-waves, the timing difference between these phases can be exploited. That is, the time difference between the direct P- and P-to-S converted waves depends on the depth of the discontinuity and the overlying velocity structure. By modeling this time difference, the depth to the interface can be determined.

SRFs are based on the same principles as PRFs (Fig. 5). The main difference is that for SRFs, the method instead uses the arrival times of the direct S-wave and the S-to-P conversions from subsurface discontinuities. As with PRFs, the amplitude and relative timing of the converted wave indicate the amount of velocity change across and the depth of the corresponding interface, respectively. In this study, the discontinuity of interest is the mantle-to-crust transition, which is indicated by a large change in seismic velocity known as the Mohorovičić discontinuity (Moho). The large drop in seismic velocity as it travels from the mantle to the crust causes both P-to-S and S-to-P conversions of observable amplitude. However, other interfaces between the

Moho and the Earth's surface also cause conversions. In Antarctica, the crust-ice interface marks a particularly large velocity change that results in large amplitude conversions. The ice is a slow velocity layer, and it causes both the direct arrivals and conversions to reverberate within this layer, making the P-to-S conversion from the Moho on PRFs particularly difficult to discern. The Moho P-to-S conversion arrives at the same time as the ice reverberations, making it very difficult to correctly identify. Alternatively, SRFs do not suffer from this problem. Since S-waves travel slower than P-waves, the S-to-P conversion from the Moho arrives before the direct S-wave and the ice reverberations, making the converted wave more identifiable.

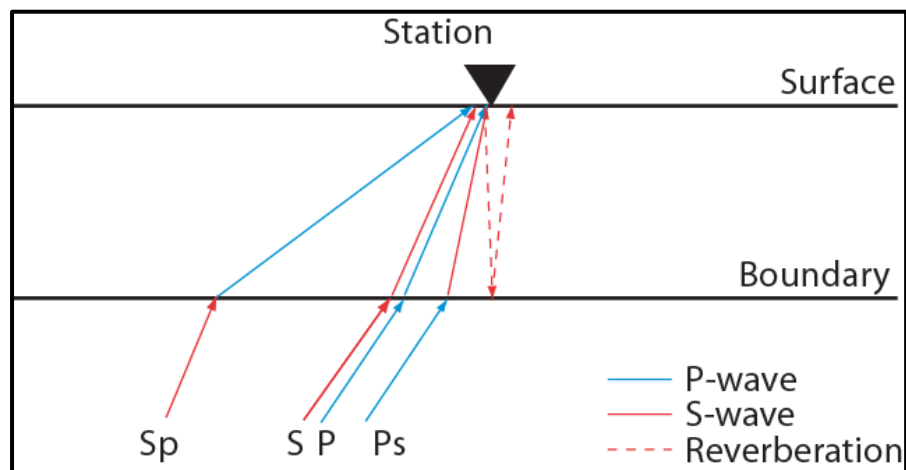


Figure 5. Cartoon illustrating different seismic phases and their conversions at subsurface discontinuities. PRFs examine P-to-S-wave (Ps) conversions while SRFs examine S-to-P (Sp) conversions. Reverberations in low velocity surface layers, such as ice, can mask the conversions of interest on PRFs.

Using SRFs instead of PRFs does have some significant challenges. The S-to-P conversions on the SRFs still arrive after the direct P-wave, so the corresponding data can be noisy. As a result, the data need to be culled so that only receiver functions with high signal-to-noise ratios are used. SRFs are also lower frequency than PRFs due to the inherent properties of

S-waves, resulting in lower resolution of the corresponding receiver functions, such that thin subsurface layers are difficult to detect. However, the resolution is sufficient to resolve crustal thickness, which is the primary goal of this study.

3.2 Employed SRF Technique

One year of seismic data from the TAMNNET stations was available to generate SRFs. Earthquakes were limited to magnitudes of 5.5 or larger, depths less than 200 km, and distances between 60-80° to optimize the signal-to-noise ratio and to prevent the interference of other arriving phases (Wilson et al., 2006). The data were decimated from 40 samples per second (sps) to 20 sps for compatibility with the receiver function software. After rotating the data from the North-East-Vertical orientation to Radial-Transverse-Vertical, the onset of the S-wave arrival was handpicked for each earthquake recorded at each station. An iterative time domain deconvolution was then used to generate the SRFs, using the vertical and radial components of the seismic data (Ligorria and Ammon, 1999). Because the S-to-P conversion of interest arrives before the direct S-wave, the seismic records must be flipped in time prior to deconvolution. The frequency content of the SRF is controlled by a Gaussian width factor, which was set to 1.0. The S-to-P conversion from the ice-crust interface is still present in the response; however, the wide Gaussian width factor used smooths this signal with the direct S-wave. This can shift the timing of the direct S-wave arrival later from its expected position at 0 s.

One SRF is generated for each earthquake recorded at each station. To help improve the signal-to-noise ratio, the SRFs for each station are culled and stacked. A total of 106 events were used to generate the stacked SRFs (Fig. 6), but the individual responses used varied from one station to another (see Appendix A). The comprehensive station stack is then used to obtain the

timing difference between the direct S-wave and the S-to-P conversion from the Moho. Stacked SRFs are shown along five profiles (Figs. 7-8). It should be noted that stations DONT, CASY, and KP05 did not have enough data with high signal-to-noise ratios to produce an adequate SRF stack; therefore, these stations are not used in further SRF analysis.

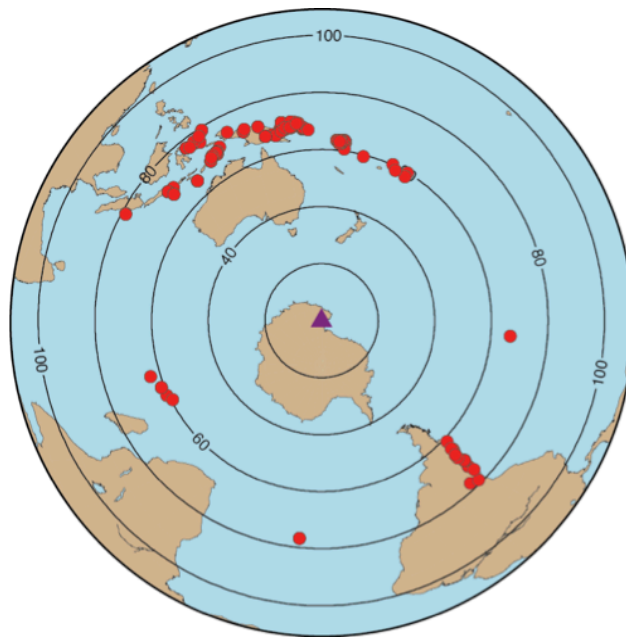


Figure 6. Map of events (red dots) meeting selection criteria, as described in the text, which were used to generate the SRF stacks (Fig. 8). The center of the TAMNNET array is marked with a triangle. Concentric lines mark great circle distances from the TAMNNET

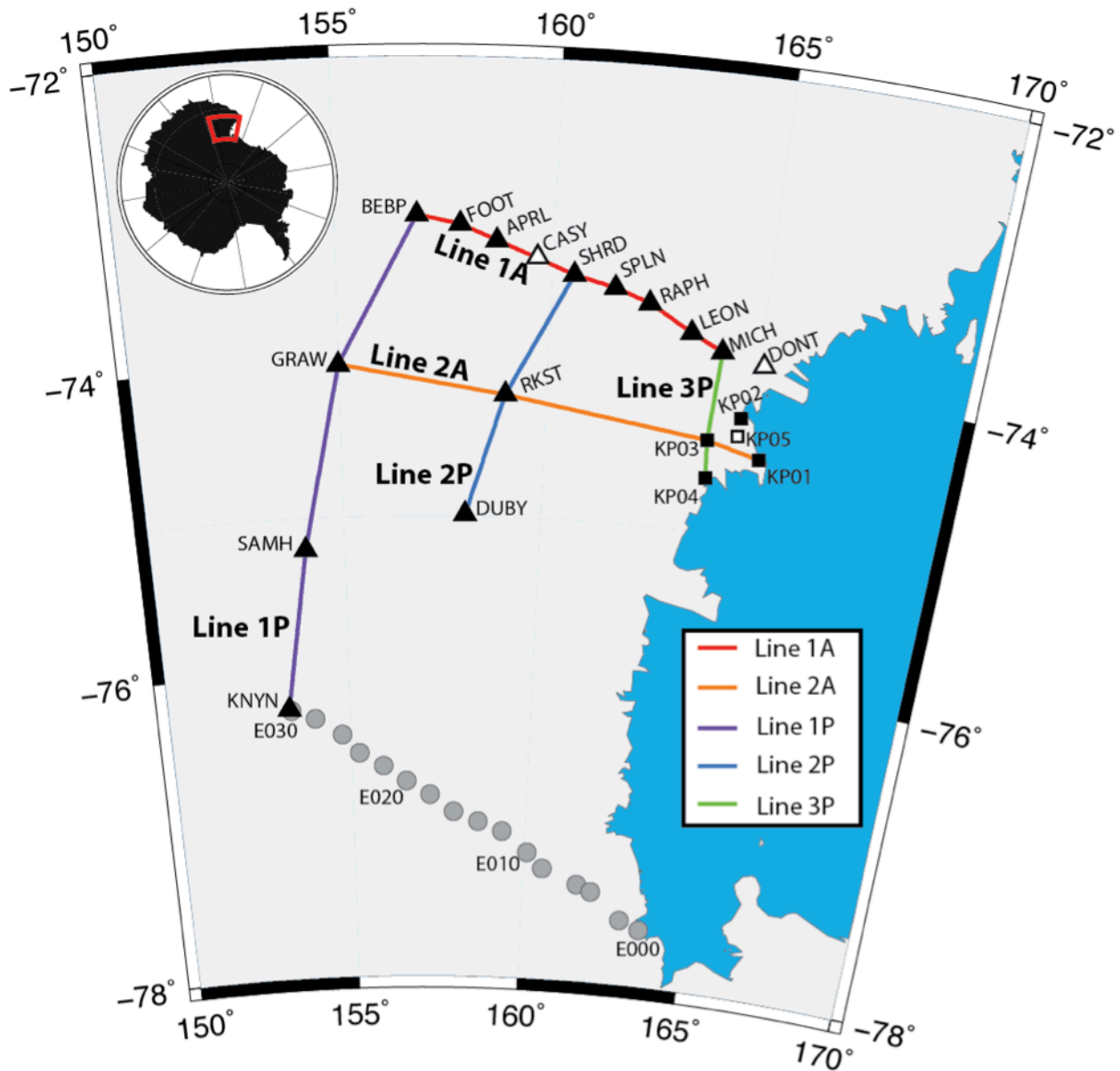


Figure 7. Profile lines of the TAMNNET and KOPRI stations. TAMNNET stations are marked as triangles, and KOPRI stations are marked as squares. For reference, stations along the E-W TAMSEIS profile are also shown (circles). Stations with poor signal-to-noise ratios that were not analyzed are shown with white centers. Lines 1A and 2A are perpendicular to the TAMs. Lines 1P, 2P, and 3P are parallel to the TAMs.

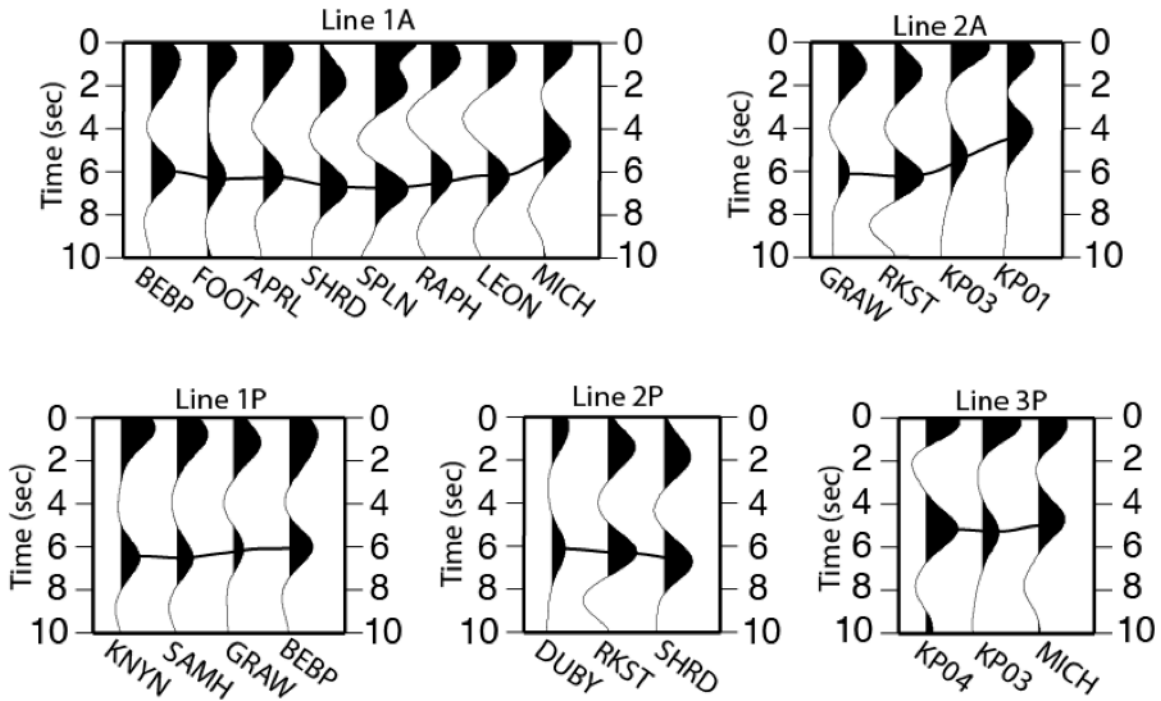


Figure 8. Stacked SRFs along the profiles shown in Figure 7. The black line denotes the S-to-P Moho conversion beneath each station.

3.3 Estimating Ice Thickness

To model the subsurface structure beneath each station, the corresponding ice thickness must also be determined. PRFs were employed for this purpose. The PRF approach used in this study is almost identical to the SRF method described above. However, for the PRFs, earthquake magnitudes and distances were restricted to 5.5 or larger and 30-90°, respectively. PRF responses were computed for all 15 TAMNNET stations using a Gaussian width factor between 2.1-3.5.

The velocity of the ice must be estimated to model the ice thickness from the PRFs. Therefore, ice thicknesses from radar data were also examined. Unfortunately, there was little radar data available over our study area, but the closest radar-determined ice thickness measurement was approximately 3.5 km from station GRAW. To estimate the ice velocity for

our study region, synthetic PRFs were generated to find the S-wave velocity (V_s) that provides the best match to the observed PRF at station GRAW. Given the ice thickness from the radar data, the best PRF timing match was obtained with $V_s = 1.9$ km/s for the ice layer, which matches accepted ice sheet V_s values (*e.g.*, Kim et al., 2007; Hansen et al., 2010). The ice V_s was fixed at 1.9 km/s and synthetic PRFs were then generated for the other stations to estimate the corresponding ice thicknesses. The ice thickness estimates from the PRFs were also compared to those from the BEDMAP2 model (Fretwell et al., 2013), and there is generally good agreement between the two datasets.

It should be noted that the PRFs for several stations (DONT, MICH, RAPH, SHRD, and SPLN) did not display a clear P-to-S conversion from the ice-crust interface. These stations have ice thicknesses less than 1 km in the BEDMAP2 model, and resolving layers this thin with receiver functions is difficult. Therefore, for these 5 TAMNNET stations, the ice thickness was taken directly from BEDMAP2 (Fretwell et al., 2013). All of the KOPRI stations were located on rock, so there is no corresponding ice thickness for these stations. A summary of the ice thicknesses is provided in Table 1. PRFs for stations with ice thickness greater than 1 km are shown in Figure 9.

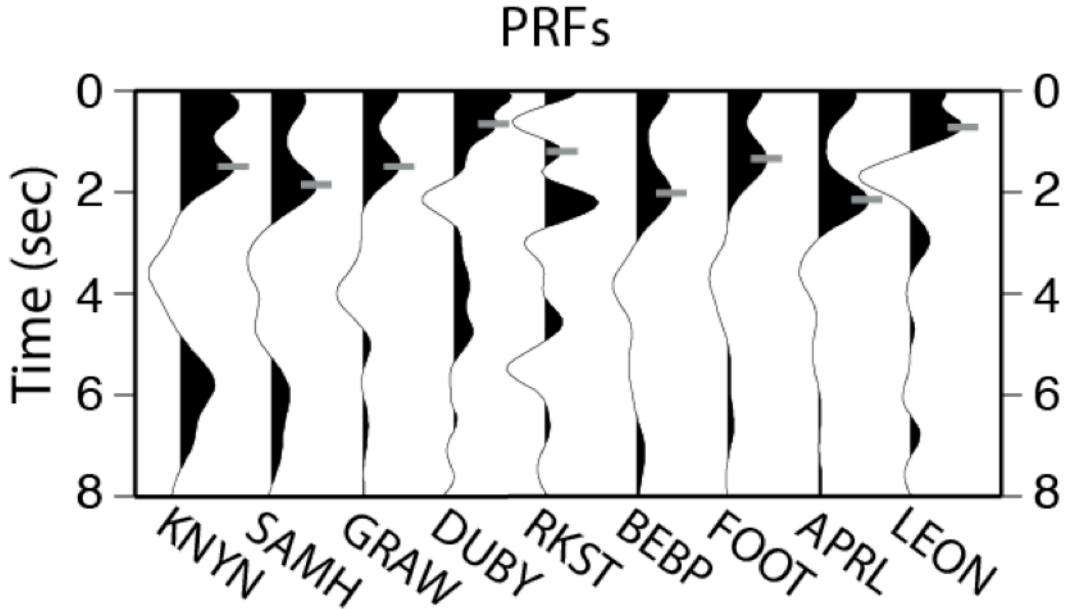


Figure 9. Stacked PRFs from all applicable stations (i.e. where the ice thickness could be resolved). Note that these are not plotted along a profile. P-to-S conversions from the bottom of the ice sheet are marked with grey tick marks and were used to model the ice thickness.

3.4 Estimating Crustal Thickness

To estimate the crustal thickness beneath each station, a grid search method based on Last et al. (1997) is used. Following this approach, a variety of velocity models are created for each station. Each model includes an ice layer (where appropriate), a two-layer crust, and an upper mantle half space. Similar to the PRFs (see section 3.3), the ice V_s is fixed at 1.9 km/s, with the ice density and Poisson ratio fixed at 0.92 g/cm³ and 0.33, respectively. The ice thickness for each station is based on the PRF results or BEDMAP2 (Fretwell et al., 2013), as described above. For the KOPRI stations, no ice layer is included. All models also have a fixed mantle velocity of 4.5 km/s, and the Poisson ratios for the crust and mantle are 0.25 and 0.28, respectively. The average crustal V_s was allowed to vary from 3.3 to 3.9 km/s in 0.05 km/s increments. Similarly, the crustal thickness was varied from 20 km to 60 km in 1 km increments.

For each examined velocity model, a synthetic dispersion curve is calculated at periods of 18, 20, 22, 25, 27, and 30 s. These calculated dispersion values are compared to smoothed dispersion curves from a Rayleigh wave surface wave inversion (Graw et al., 2014). To be conservative, models that match the dispersion data within an error of ± 0.09 km/s are retained. Each retained model is then further examined by comparing its predicted Moho S-to-P conversion time to that observed on the stacked SRF. For a given station, the depth and distance of each event contributing to the SRF stack is used to determine an average ray parameter, which is then used to compute the vertical slowness for each layer in the velocity model and ultimately to predict conversion timing. Predicted times that match the observed SRF timing within ± 0.4 s are accepted. The suite of models that fit both the dispersion and SRF data within error are used to determine the average crustal V_s and thickness beneath a given station. An example of this data modeling is shown in Figure 10, and results for the remaining stations are included in Appendix B.

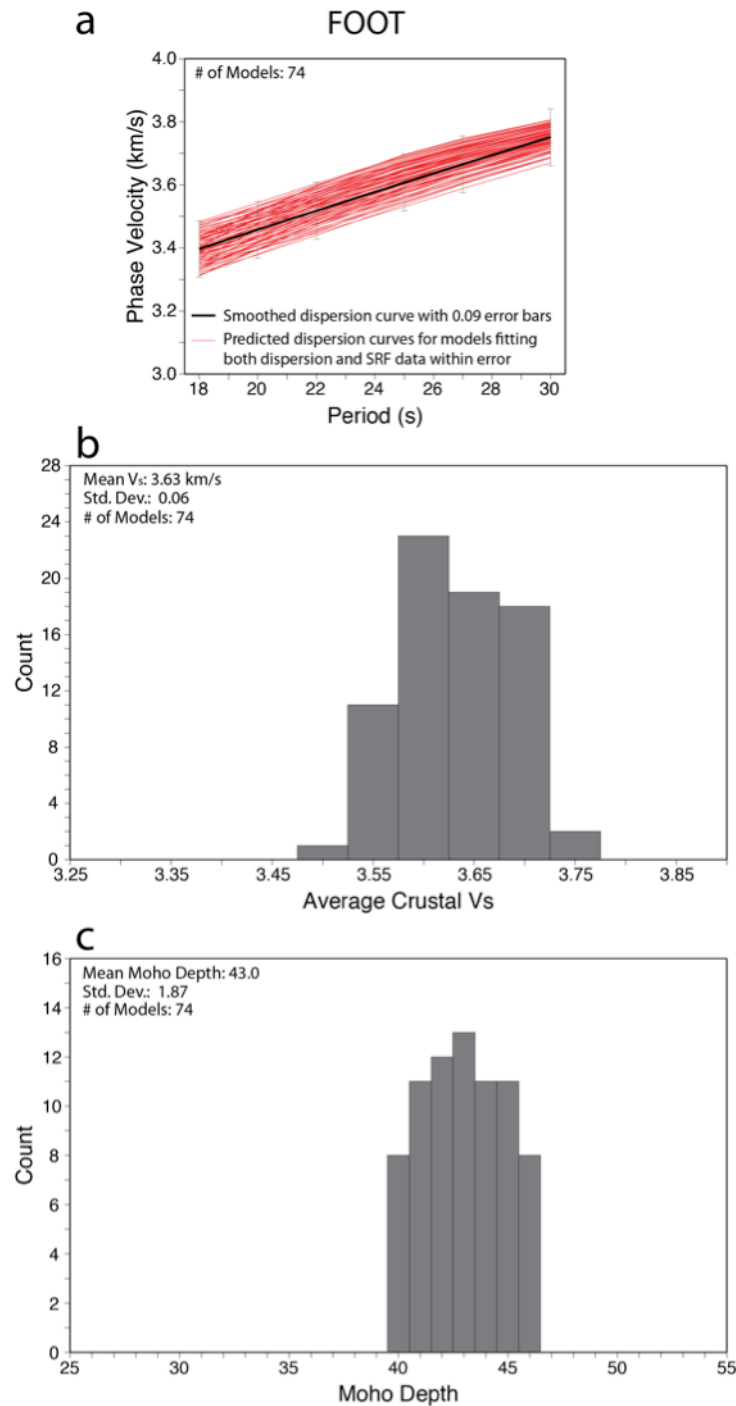


Figure 10. Data modeling and grid search results, using station FOOT as an example. (a) Red lines show Rayleigh wave phase velocity dispersion curves for models that fit both the dispersion data (black line; Graw et al., 2014) within 0.09 km/s and the Moho S-to-P conversion time within 0.4 s. (b) Histogram of mean crustal shear velocities encompassed by the “fit” models from (a). (c) Histogram of Moho depths encompassed by the “fit” models from (a). Note that the Moho depths include the ice layer.

3.5 Evaluating Additional Uncertainty

As described above, the range of models that match both the dispersion data and the SRF timing in the grid search provide some estimate of error. The standard deviation for the average crustal thickness across all stations is ~ 2 km, while the standard deviation for the average crustal V_s is ~ 0.06 km/s (see Fig. 10 for an example of the variability of results). However, uncertainty can also arise from the fixed parameters used in the grid search. To account for this, the ice thickness, ice velocity, and crustal Poisson's ratio were varied within reasonable limits to assess the corresponding model differences. As described in section 3.3, the ice thickness for most stations was obtained using PRF modeling. Comparing these ice thickness values to those from BEDMAP2 (Fretwell et al., 2013), the average ice thickness differed by ~ 0.2 km. Previous studies indicate that ice V_s values can vary but generally fall between 1.5-2.0 km/s (Kim et al., 2007). In Antarctica, crustal Poisson's ratios have been estimated between 0.24 and 0.27 (Finotello, 2009; Hansen et al., 2010). By setting the ice V_s to 2.0 km/s, decreasing the ice thickness by 0.2 km, and setting the crustal Poisson's ratio to 0.24, the maximum crustal thickness for a given station associated with these parameter uncertainties can be determined. Similarly, the minimum crustal thickness estimate can be found by increasing the ice thickness by 0.2 km, setting the ice V_s to 1.5 km/s, and setting the crustal Poisson's ratio to 0.27. Using these parameter variations in the grid search, the average crustal thickness and crustal V_s uncertainties are ± 2 km and ± 0.04 km/s, respectively. Combining this with the standard deviations from the original grid search results, it is estimated that the crustal thickness is resolved to within ± 4 km and that the average crustal V_s is resolved to within ± 0.1 km/s.

4.0 RESULTS

The results from this study offer new insights into the crustal structure beneath the TAMs and the WSB. Other than station KNYN, all examined stations are located within a previously unexamined portion of these tectonic domains. The following subsections describe the resulting estimates of ice thickness, crustal thickness, and average crustal shear wave velocity beneath the TAMNNET and KOPRI stations.

4.1 Ice Thicknesses

Ice thicknesses are summarized in Table 1. The ice thickness across the TAMNNET array varies from 0.10 km at station RAPH to 2.85 km at station APRL. Generally, stations deployed within the TAMs are underlain by the least amount of ice. A notable exception is station LEON, which was located on a deep (1.05 km) glacial valley. Stations RKST and DUBY (Fig. 1) have ice thicknesses less than 2 km. Sites located further on the East Antarctic plateau are underlain by thicker ice, averaging 2.38 km.

Station name	Latitude (°)	Longitude (°)	PRF Ice thickness (km)	BEDMAP2 Ice thickness (km)
KP01	-74.4866	165.2897	0.0	0
KP02	-74.2319	164.7334	0.0	0
KP03	-74.3995	163.9708	0.0	0
KP04	-74.6448	164.0360	0.0	0
KP05	-74.3495	164.6904	0.0	0
MICH	-73.8171	164.0998	-	0.30
LEON	-73.7134	163.3278	1.05	1.15
RAPH	-73.5473	162.2885	-	0.10
SPLN	-73.4662	161.4712	-	0.45
SHRD	-73.3989	160.4988	-	0.20
APRL	-73.1949	158.7034	2.85	2.85
FOOT	-73.0934	157.8534	2.05	2.40
BEBP	-73.0325	156.8690	2.70	2.90
RKST	-74.2011	159.0018	1.60	1.70
DUBY	-74.9853	158.0773	1.05	0.90
SAMH	-75.2030	153.9968	2.50	2.00
GRAW	-74.0042	154.9887	2.05	2.50
KNYN	-76.2374	153.3270	2.10	1.85

Table 1. Summary of ice thickness estimates. BEDMAP2 (Fretwell et al., 2013) values are shown for comparison and are used at stations where PRFs could not resolve the ice thickness.

4.2 KOPRI Rock Stations

Using the SRF analysis described in section 3.2, crustal thicknesses of ~30-40 km were found beneath the KOPRI stations (Table 2). As mentioned above, the KOPRI stations as well as nearby station TNV (Fig. 11a) were all deployed on rock, with no associated ice layer.

Therefore, others have examined the crustal structure beneath these stations with the traditional PRF approach. Both Finotello et al. (2009) and Lawrence et al. (2006a) estimated the crustal thickness beneath station TNV, which is very close to station KP04 (Fig. 11a), and Park (2014, personal communication) estimated the crustal structure beneath station TNV as well as beneath all the KOPRI stations. The results from these three studies are fairly consistent with one another, indicating ~18-20 km thick crust beneath TNV (with error estimates of ± 2 km, ± 5 km,

and ± 0.4 km from Lawrence et al. 2006a, Finotello et al., 2009, and Park, 2014, respectively). Beneath the KOPRI stations, the crustal thickness ranges between ~ 13 -27 km (Fig. 11a; Park, 2014, personal communication). These crustal thickness estimates are much thinner than those obtained in the current SRF study; therefore, this discrepancy needs to be addressed.

As mentioned in section 3.2, the 1.0 Gaussian width factor used in the SRF analysis is fairly wide and can smear the direct S-wave signal with S-to-P conversions from shallow discontinuities. To assess if the Moho discrepancy between the original SRF results and those from previous studies (Lawrence et al., 2006a; Finotello et al., 2009; Park, 2014, personal communication) results from the Gaussian width factor used, a different value (1.5) was examined, using station KP04 as a test case. With this new Gaussian factor, higher frequency signal could be examined, revealing a more coherent Moho conversion with a smaller SRF timing (Fig. 12) that is comparable to the conversion timings found in previous PRF studies (Lawrence et al., 2006a; Finotello et al., 2009; Park, 2014, personal communication). This indicates that the original Gaussian width factor used was too wide to highlight the shallow crustal discontinuity beneath these stations, placing important constraints on the SRF imaging limits for shallow crustal structure.

Using the revised SRF timing, the grid search procedure outlined in section 3.4 was repeated to assess the associated crustal structure beneath station KP04. However, no model could be found that simultaneously fit the dispersion data provided by Graw et al. (2014) and the revised (smaller) SRF timing. It should be noted that the dispersion data available are limited to a minimum period of 18 sec, which is primarily sensitive to structure at ~ 30 km depth (Graw et al., 2014). That is, shorter period dispersion data would be needed to provide sensitivity to such shallow crustal structure (~ 20 km). This is evident, for example, if one compares the current SRF

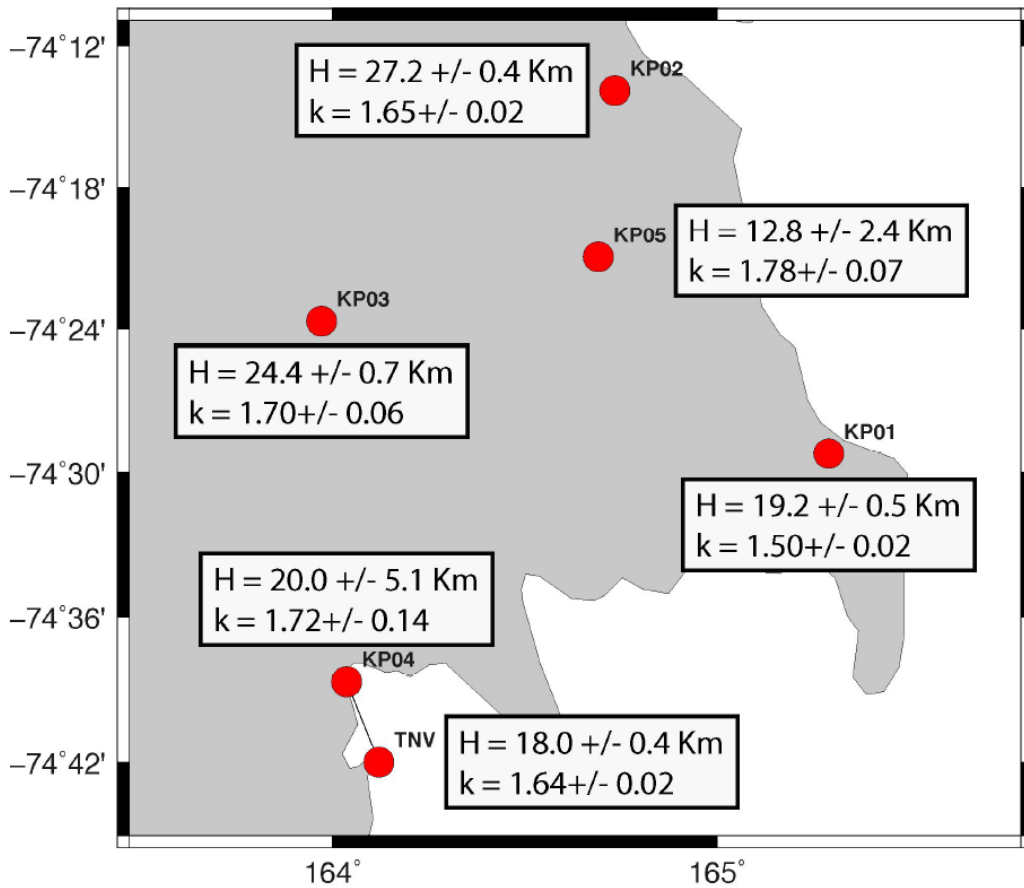
analysis to that from Hansen et al. (2009), where they were able to image shallower crustal structure using 16 sec dispersion data from ambient noise tomography. Therefore, an alternative approach was needed to estimate the average crustal velocity beneath the coastal KOPRI stations.

Lawrence et al. (2006a) used a joint inversion of PRFs and Rayleigh wave phase velocities to estimate the crustal structure beneath station TNV, where they found an average crustal velocity of ~ 3.4 km/s. This agrees well with recent work from Park (2014, personal communication), who found average crustal velocities of ~ 3.3 - 3.5 km/s beneath station KP04 (Fig. 11b) as well as beneath the other KOPRI stations. These velocity estimates also match the average crustal velocity found at TAMNNET station MICH in the current study, which is close to the Ross Sea coastline (see section 4.4). These velocity estimates (3.3-3.5 km/s) were used in a new grid search to predict the SRF conversion timing from the Moho beneath station KP04. Similar to before, models that fit the timing within error (± 0.4 s) were retained. All accepted models have crustal thicknesses between 14-19 km, which agrees well with the previous PRF estimates (Lawrence et al., 2006a; Finotello et al., 2009; Park, 2014, personal communication). Given this consistency, along with the lack of short period dispersion data constraints, the crustal thicknesses determined by the PRF analysis (Fig. 11a; Table 3; Park, 2014, personal communication) will instead be analyzed for the KOPRI rock stations, as opposed to the original SRF-derived thicknesses.

Station name	Mean crustal V_s (km/s)	Std. dev. of mean crustal V_s	Mean Moho depth, with ice thickness (km)	Std. dev. of mean Moho depth
KP01	3.41	0.07	29.8	1.65
KP02	3.60	0.06	39.6	1.91
KP03	3.59	0.06	38.7	1.92
KP04	3.57	0.06	37.7	1.99
MICH	3.49	0.07	33.9	1.90
LEON	3.64	0.06	40.7	1.86
RAPH	3.66	0.05	46.0	1.86
SPLN	3.64	0.05	49.7	2.02
SHRD	3.71	0.02	49.4	1.67
APRL	3.61	0.06	41.6	1.96
FOOT	3.63	0.06	43.0	1.87
BEBP	3.73	0.05	41.1	1.72
RKST	3.70	0.04	43.8	1.89
DUBY	3.75	0.06	44.2	1.96
SAMH	3.72	0.05	45.8	1.87
GRAW	3.77	0.06	43.1	1.88
KNYN	3.71	0.06	46.2	1.95

Table 2. Summary of mean crustal V_s and mean crustal thickness beneath each station as well as associated standard deviations found with the SRF and grid search method. Note that the crustal thicknesses include the thickness of the ice layer.

a)



b)

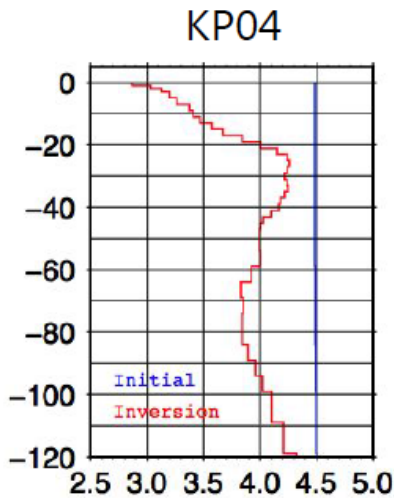


Figure 11. Seismic analysis results for the KOPRI stations and station TNV, provided by Park (2014, personal communication). (a) Map showing the PRF-determined crustal thicknesses (H) and associated errors for each station. (b) Shear-wave velocity versus depth plot for station KP04, which was used to estimate the average crustal V_s beneath this station.

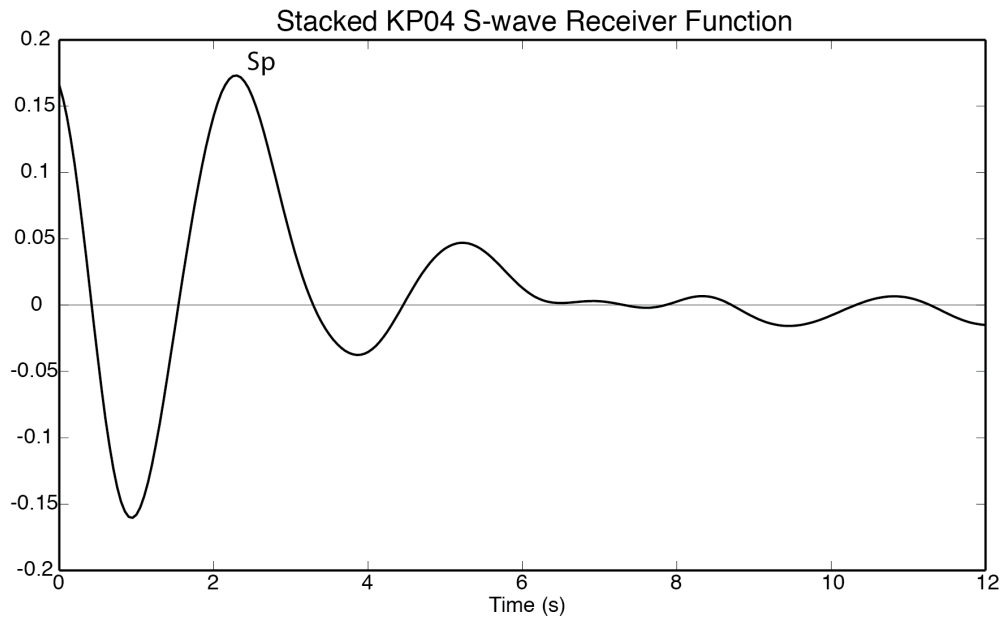


Figure 12. SRF stack for KOPRI station KP04, using the new Gaussian width factor of 1.5. The Sp Moho conversion is labeled. Note the earlier arrival compared to that seen in Figure 8.

4.3 TAMNNET Ice Stations

Crustal thickness estimates from the SRF analysis of the TAMNNET stations are summarized in Tables 2 and 3. In Table 3, the Moho depths are reported relative to sea level. These values were calculated using the total depth (including ice thickness) to the crust-mantle interface, which was determined from the grid search, minus the corresponding station elevation. The total crustal thicknesses are also reported (see Table 3 for further details).

The crustal structure beneath the five profiles shown in Figure 7 is also highlighted (Fig. 13). These profile locations were selected based on the station configuration and usefulness for comparisons. Two profiles extend across the TAMs, with three additional profiles parallel to the

mountain range. Profile 1A begins at the coast and crosses the TAMs, giving the most comprehensive view of how the crustal thickness changes from the TAMs front to the edge of the WSB. Line 2A runs parallel to Line 1A. While the station spacing along Line 2A is not as dense, this profile was chosen to verify the lateral continuity of the results from Line 1A. Line 1P is perpendicular to both Lines 1A and 2A and extends between the furthest inland stations. Line 2P is located halfway between Line 1P and the coast, situated approximately over the center of the TAMs. Line 3P, which is closest to the coast, is not very long, but it is used as a comparison to Lines 1P and 2P.

Along Line 1A (Fig. 13a), the Moho depth increases from 33 km near the coast to 47 km under the TAMs. The crust then shallows somewhat to an average depth of ~40 km beneath the WSB. Line 2A starts closer to the coast and shows thinner crust in that area, but the crust still thickens inland, from 20 to 25 km over a horizontal distance of 40 km. Beneath the rest of profile 2A (Fig. 13b), the Moho depth increases to ~41 km and then remains fairly constant. This verifies the general trend of Line 1A, with thinner crust near the Ross Sea coastline that deepens and then maintains a relatively constant depth of ~40 km beneath the WSB. Line 1P (Fig. 13c) shows a slight, continuous increase in the Moho depth from station BEBP in the north to station KNYN in the south, with the Moho at 39 km and 44 km depth, respectively. Line 2P (Fig. 13d), unlike Line 1P, shows the thickest crust at its northern end beneath station SHRD (~47 km), with slightly thinner crust (~42 km) to the south beneath stations RKST and DUBY. Line 3P (Fig. 13e) displays thinner crust than both Lines 1P and 2P, with the Moho at 20 km depth beneath station KP04 and at 33 km depth beneath station MICH. The average crustal thicknesses along Lines 1P, 2P, and 3P are ~42 km, ~44 km, and ~26 km, respectively.

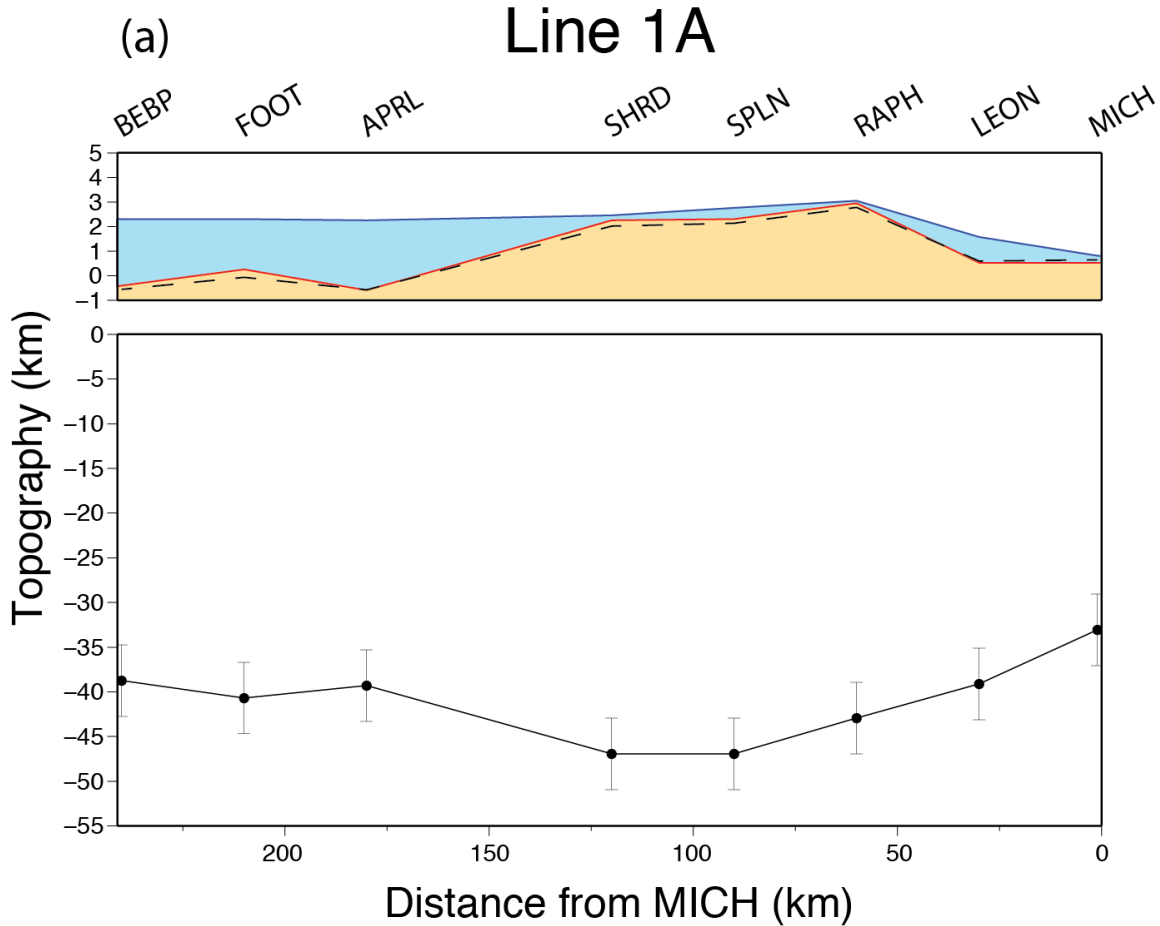


Figure 13. Moho topography along the five examined profiles (Fig. 7). For all plots, the blue shaded area represents the ice layer, as determined by the PRFs or from BEDMAP2 (Fretwell et al., 2013). The tan shaded area represents bedrock topography. Bedrock elevations were determined by subtracting the ice thickness from the station elevation. Note that some bedrock elevations are below sea level. The black dashed line represents the bedrock topography from BEDMAP2 (Fretwell et al., 2013). Moho depth estimates are plotted as black dots with ± 4 km error bar, as discussed in the text.

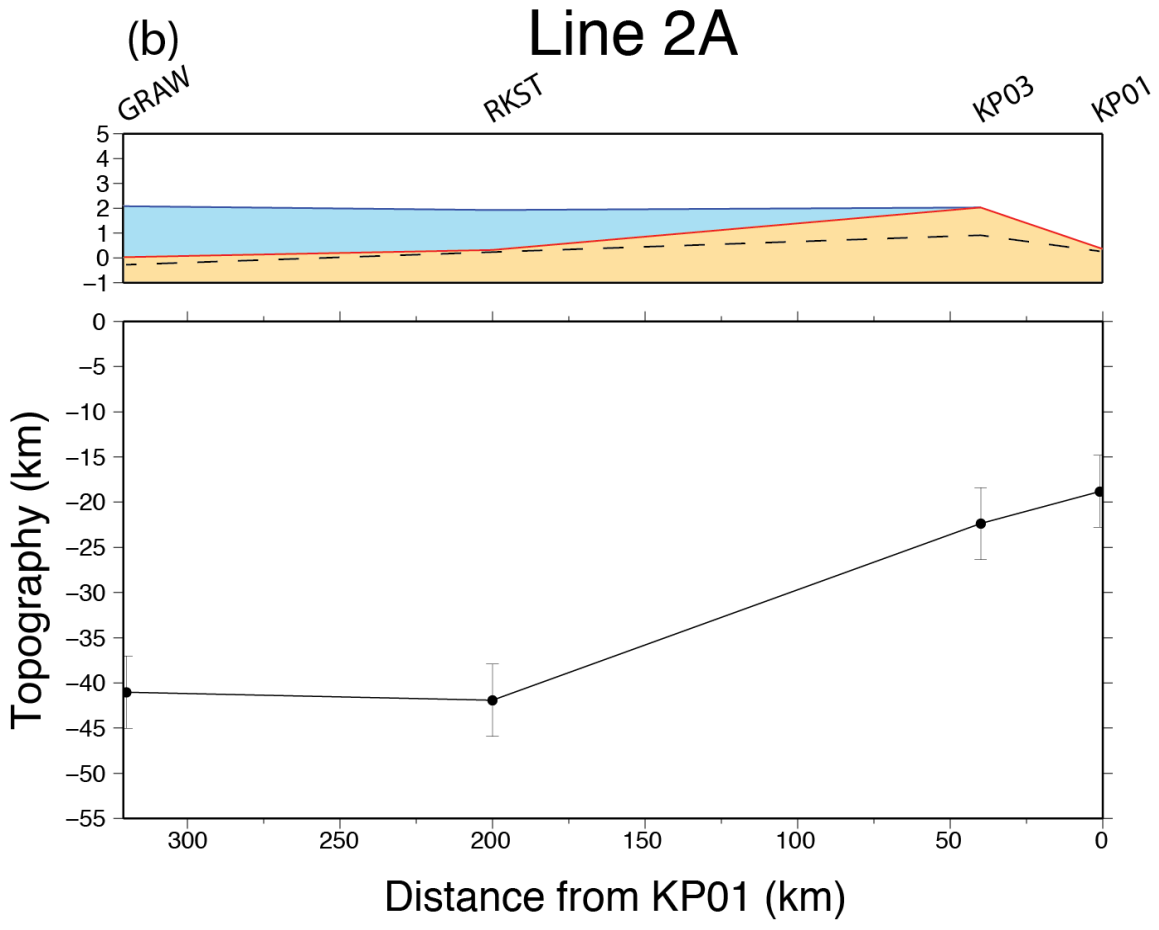


Figure 13. Continued

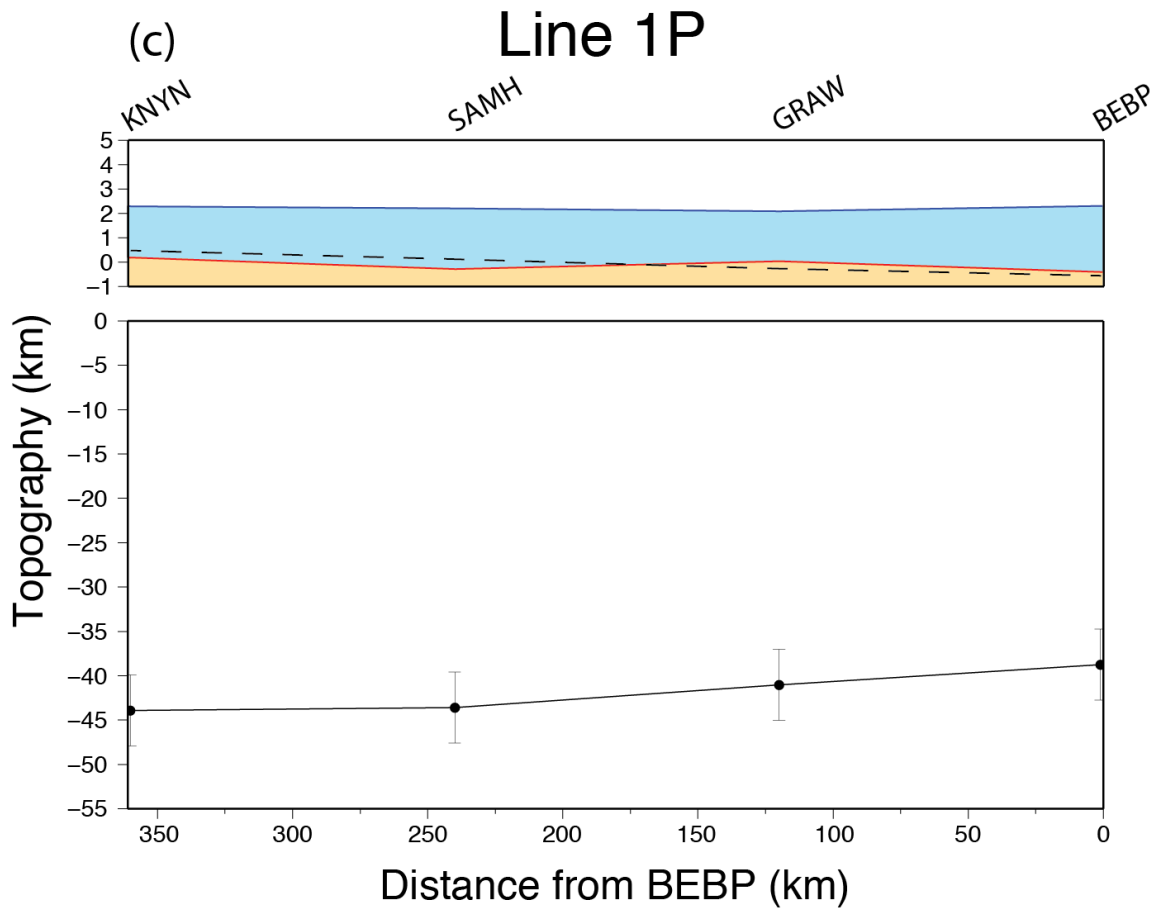


Figure 13. Continued

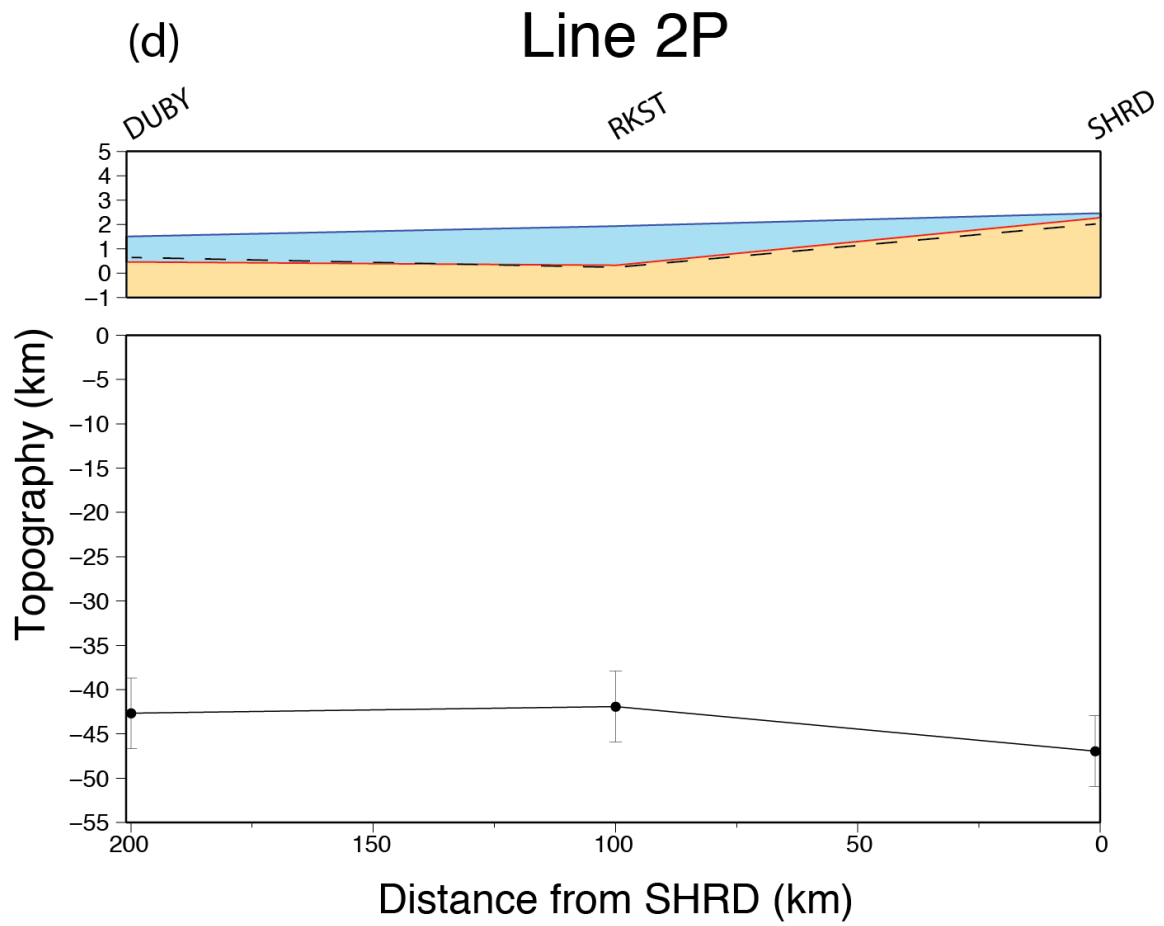


Figure 13. Continued

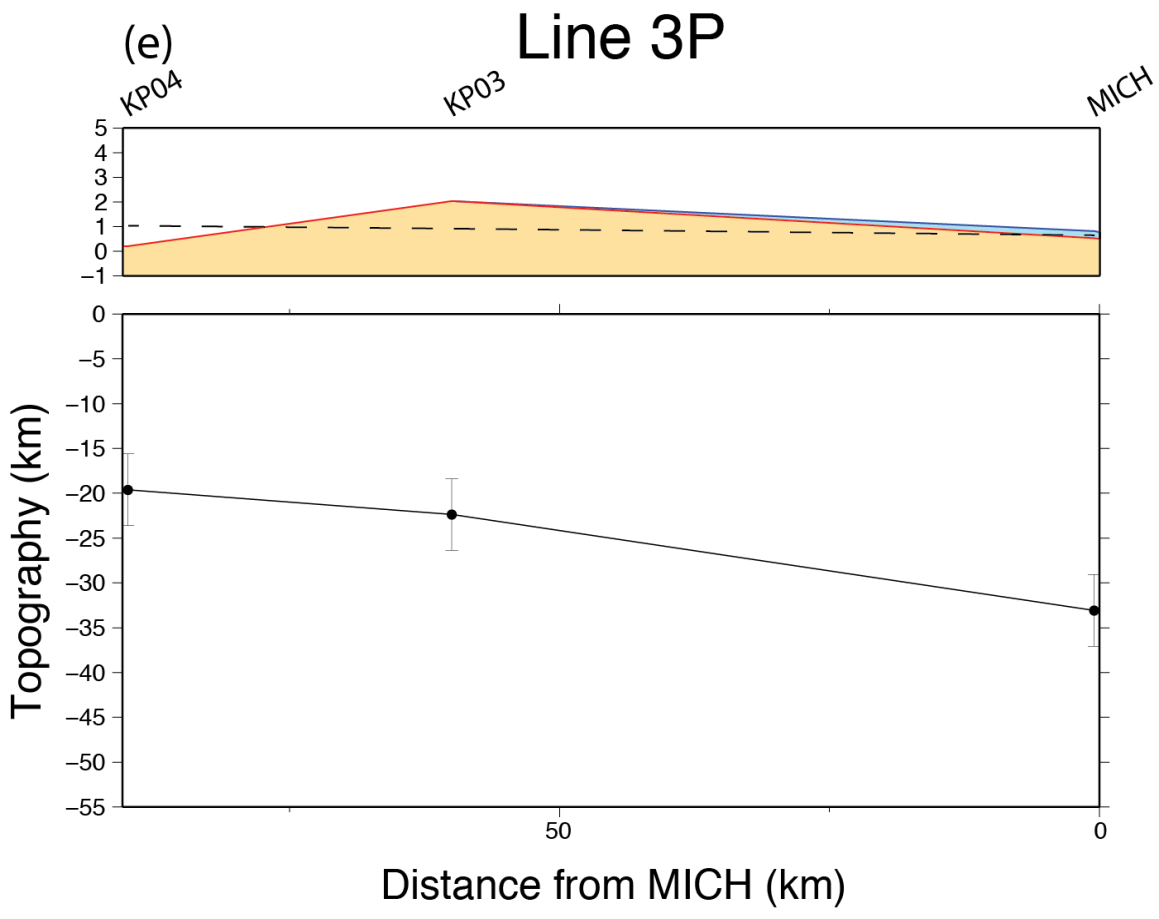


Figure 13. Continued

All profiles indicate thinner crust near the coast that thickens inland. Moho depths directly under the TAMs are variable, between 42 and 47 km, but this variation could be accounted for with the ± 4 km uncertainty associated with the crustal thickness estimates. Behind the TAMs, beneath the East Antarctic plateau, the crust maintains a thickness of ~ 40 km.

4.4 Crustal S-wave Velocity

The average crustal shear velocities are summarized in Figure 14 and Table 3. The minimum average crustal V_s for the TAMNET stations is 3.49 km/s, found beneath station MICH. The maximum average V_s is 3.77 km/s beneath station GRAW. As noted in section 4.2, the velocities beneath the KOPRI stations are taken from Park (2014, personal communication). Generally, lower crustal V_s values are observed near the coast, with higher crustal V_s values further inland. Station MICH and all the KOPRI stations have V_s values at or below 3.5 km/s. Stations LEON, RAPH, SPLN, APRL, and FOOT, which are located in the middle of the TAMNET transect, have average crustal V_s between 3.6 and 3.7 km/s. Station SHRD has a slightly higher V_s of 3.71 km/s. All other stations are on the East Antarctic plateau and have average crustal V_s larger than 3.7 km/s.

Station name	Mean crustal V_s (km/s)	Mean Moho depth, with ice thickness (km)	Mean Moho depth below sea level (km)	Station elevation (km)	Total crustal thickness (km)	Error (\pm value in km)
KP01	3.45	19.2	18.79	0.41	19.2	0.5
KP02	3.40	27.2	26.54	0.66	27.2	0.4
KP03	3.45	24.4	22.4	2.02	24.4	0.7
KP04	3.40	20	19.8	0.20	20	5.1
KP05	3.35	12.8	10.09	2.71	12.8	2.4
MICH	3.49	33.9	33.1	0.82	33.6	4
LEON	3.64	40.7	39.1	1.57	39.7	4
RAPH	3.66	46.0	42.9	3.05	45.9	4
SPLN	3.64	49.7	47	2.75	49.3	4
SHRD	3.71	49.4	46.9	2.46	49.2	4
APRL	3.61	41.6	39.3	2.26	38.8	4
FOOT	3.63	43.0	40.7	2.31	40.15	4
BEBP	3.73	41.1	38.8	2.30	38.4	4
RKST	3.70	43.8	41.9	1.93	42.2	4
DUBY	3.75	44.2	42.7	1.51	43.2	4
SAMH	3.72	45.8	43.6	2.21	43.3	4
GRAW	3.77	43.1	41	2.09	41.1	4
KNYN	3.71	46.2	43.9	2.29	44.1	4

Table 3. Summary of mean crustal V_s and mean crustal thickness beneath each station. The Moho depth below sea level listed was found by subtracting the corresponding station elevation from the mean Moho depth. Total crustal thickness is the mean Moho depth, minus the ice thickness. V_s values for the KOPRI stations are from Park (2014, personal communication).

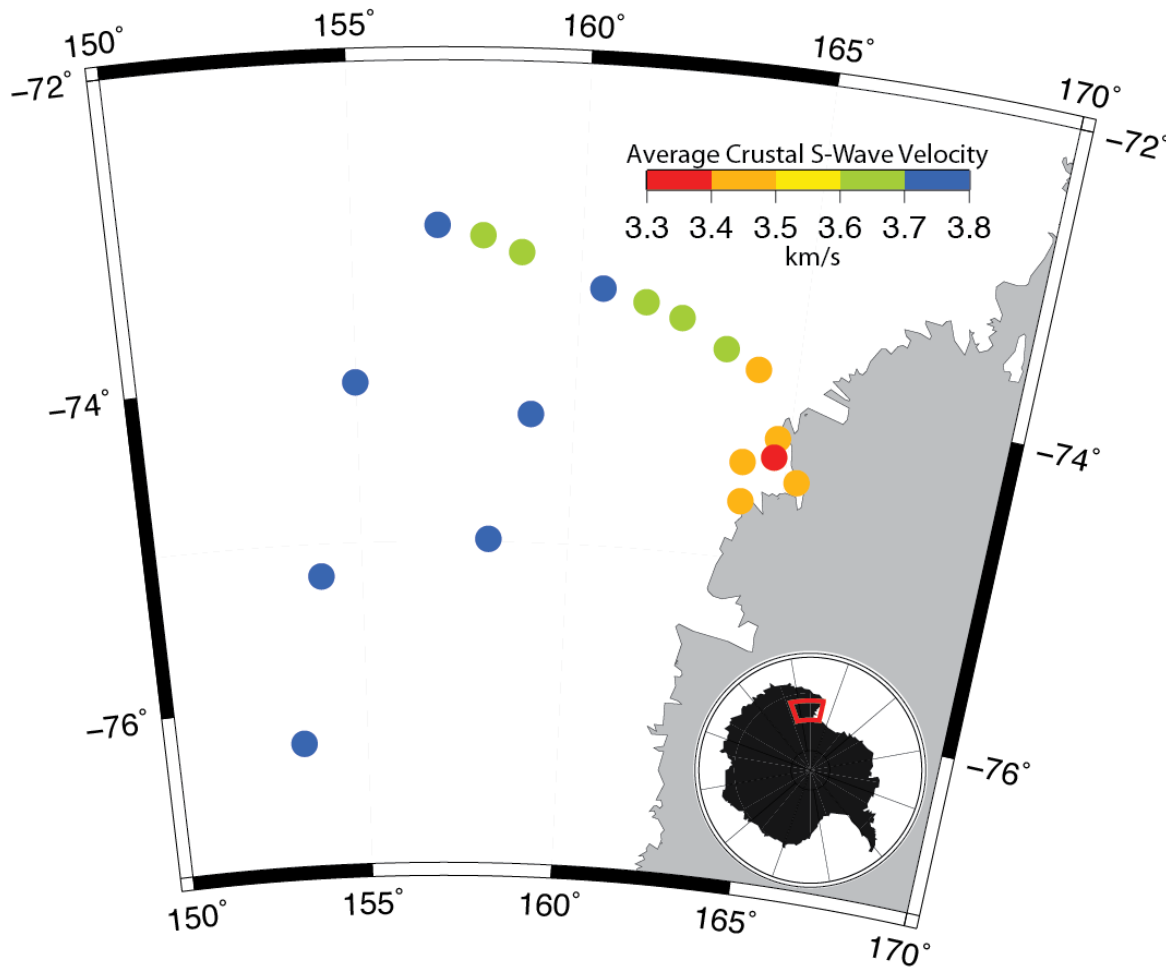


Figure 14. Average crustal shear velocities beneath the TammNet and KOPRI stations, plotted as circles where the colors correspond to velocity in km/s.

5.0 DISCUSSION

5.1 Crustal Thicknesses and Isostatic Compensation

Generally, the crustal thickness estimates from the current study well match those from previous studies in the central TAMs. For instance, using a methodology similar to that employed here, Hansen et al. (2009) showed ~25 km thick crust near the Ross Sea coast and ~44 km thick crust at the inland end of the E-W TAMSEIS profile (Fig. 1). The Moho depth beneath station KP01 near the coast is ~20 km, and the Moho depth beneath station KNYN, which again reoccupies the station position at the end of the E-W TAMSEIS profile, matches the 44 km estimate from Hansen et al. (2009). ten Brink et al. (1993) suggested the crust is 30-35 km deep ~40 km inland from the Ross Sea, and Bannister et al. (2003) reported thin (~20 km) crust 30 km inland from the coast. Bannister et al. (2003) also extended their observations further inland to a horizontal distance of ~85 km from the Ross Sea, where a crustal thickness of 36-40 km was found. Again, these estimates are consistent with the results shown in Figures 13a and 13b (Lines 1A and 2A).

However, some variations in the crustal structure are observed between the central and northern TAMs. The E-W TAMSEIS profile and TAMMNET Line 1A have similar lengths and cross the TAMs in parallel transects (Fig. 1). As described above, both profiles show similar crustal thickening trends from the Ross Sea coast and into the EA craton. Yet, in the middle of TAMMNET Line 1A (Fig. 13a), the Moho depth (relative to sea level) reaches up to $\sim 47 \pm 4$ km. This is seen, for example, beneath stations RAPH, SPLN, and SHRD, and these crustal estimates

are somewhat deeper than the $\sim 41 \pm 3$ km Moho depth reported by Hansen et al. (2009) beneath the middle of the E-W TAMSEIS line. The margins of error for these deepest depths on each profile overlap slightly, but the difference in crustal thickness between the two is significant. It should be noted though that this increased Moho depth under the TAMs seen along TAMNNET Line 1A does not appear to trend along-strike of the TAMs. That is, it is not observed beneath the other stations on Line 2P, which intersects with Line 1A at the deepest observation point before extending south toward the E-W TAMSEIS profile (Figs. 7 and 13d).

An examination of the surface topography differences between TAMNNET Line 1A and the E-W TAMSEIS profile is explored to assess the crustal discrepancies between these two transects. The average elevation of the three TAMNNET stations with deeper Moho estimates (i.e. stations RAPH, SPLN, and SHRD) is 2,750 m, with a maximum elevation at station RAPH of 3,050 m. These elevations are ~ 1 km higher than any of the station elevations along the E-W TAMSEIS profile (Hansen et al., 2009). The following equation is used to roughly estimate the additional crustal root thickness expected for an additional ~ 1 km of elevation, assuming Airy isostatic compensation (Turcotte and Schubert, 2002):

$$T = (\rho_c * h) / (\rho_m - \rho_c)$$

In this equation, T is the thickness of the crustal root, h is the height of the topography, ρ_c is the density of the crust, and ρ_m is the density of the mantle. Estimating the crustal and mantle densities as 2.8 and 3.3 g/cm³, respectively, a topographic change of 1 km is associated with a 5.6 km root. This is a close match to the change in crustal thickness observed beneath the TAMs between TAMSEIS (~ 41 km) and TAMNNET (~ 47 km).

The above equation can also be used to estimate the thickness of the crustal root needed to completely isostatically compensate the total TAMs elevation, using Airy isostasy. As a

separate examination of the potential isostatic compensation of the TAMs beneath TAMNNET, we investigate the total thickness that would be required to support the observed topography in isostatic equilibrium. For context, we will assume the average crustal thickness that is already isostatically compensated is represented by the Moho depths observed beneath the EA craton, where crustal elevations are near sea level. Since there is no significant bedrock topography requiring isostatic compensation on Line 1P (Fig. 13c), the average crustal thickness of ~ 42 km from beneath those stations is used as a reference thickness. At station RAPH, there is a total elevation of $\sim 3,000$ m or, in other words, an extra 3 km of elevation. Using this value in the above equation, a total crustal thickness of ~ 59 km would be needed to support these high elevations. This is well outside the observed crustal thickness and error estimate of $\sim 43 \pm 4$ km beneath station RAPH. Similar calculations for the elevations at stations SHRD and SPLN, where the deepest Moho is observed (Table 3), would require total crustal thicknesses of ~ 55 km and ~ 57 km, respectively. Again, this is much thicker than the ~ 47 km indicated by the results and demonstrates that the observed high topography is not in isostatic equilibrium since it would require an additional ~ 8 km or more of crustal root, which is not observed.

5.2 TAMs Uplift Models and Formation of the WSB

The lack of a crustal root thick enough to fully isostatically compensate the observed elevations is clear. However, the uncertainty associated with the crustal thickness estimates makes it difficult to assess if a small (3-5 km) root is present beneath the TAMs, and the somewhat thicker crust beneath Line 1A (Fig. 13a) indicates that this may be a possibility. Studinger et al. (2004), Lawrence et al. (2006a), and Bialas et al. (2007) suggested that a 4-5 km thick crustal root may be present beneath the mountain range. Studinger et al. (2004) used this

small root to model Airy isostasy, although they acknowledged that erosional unloading would also be necessary to explain the TAMs uplift since such a small root is not sufficient to support the observed elevations. They suggested this root may have resulted from a collapsed plateau, which was also investigated by Bialas et al. (2007). That is, the root could be a remnant of the edge of a ~55 km thick collapsed plateau, where erosional denudation shrank the root and resulted in higher elevations in the TAMs. Lawrence et al. (2006a) suggested a small root beneath the TAMs could contribute to their uplift model, which combines thermal loading, flexure, erosion, and isostatic support.

If a small (4-5 km) root does play an important role in supporting the high mountain elevations, it should be a continuous feature along-strike of the TAMs. However, as shown in this study, that does not seem to be the case. The thick (~47 km) crust that may be associated with such a root is only observed beneath the middle of TAMNNET Line 1A (Fig. 13a), and it does not continue to the south along Line 2P (Fig. 13d), which extends along the TAMs. This is inconsistent with the plateau collapse and associated uplift models put forth by Studinger et al. (2004) and Bialas et al. (2007). The Lawrence et al. (2006a) model may be consistent with the observations, where a small root could locally contribute to higher elevations, but this would not be an applicable model for the whole length of the TAMs. Instead, small variations in crustal thickness, such as those observed between the TAMNNET and TAMSEIS profiles (section 5.1), are more likely associated with local topographic variability.

A further difference between the results of Studinger et al. (2004), Lawrence et al. (2006a), and those from the current study are the crustal thicknesses beneath the EA craton, at the edge of the WSB. Both Studinger et al. (2004) and Lawrence et al. (2006a) indicated ~35 km thick crust beneath the WSB. Similar estimates were made by Ferraccioli et al. (2001; 31 ± 2

km), who argued that the thin crust provides evidence for rifting or extension in the WSB. The average crustal thickness of $\sim 42 \pm 4$ km observed in the current study is about 10 km thicker than these previous studies indicated. This contradicts the claim that thin crust is present, and thus does not support a rifted or extended origin for the WSB, where thinned crust is the main evidence cited to support the idea.

The current study, along with Hansen et al. (2009), indicates uniform crustal thickness (~ 42 - 44 km) beneath the northern and central TAMs, respectively, and beneath the EA plateau. This suggests that there is little variability in the crustal structure along-strike of the TAMs. Stern and ten Brink (1989) indicated that a uniform, ~ 45 km thick crust is consistent with a flexural uplift model for the TAMs. Additionally, this model indicates that the lithospheric thickness would be thinner near the coast, at the free edge of the East Antarctic plate (Stern and ten Brink, 1989; ten Brink and Stern, 1992; ten Brink et al. 1997). As is seen from the examined profiles (Fig. 13), the current observations agree with this component of the flexure model as well. The flexural model can also explain the structure of the WSB, where the basin is a down-warp caused by the uplift of the TAMs and is underlain by crust of comparable thickness (Stern and ten Brink, 1989; ten Brink and Stern, 1992; ten Brink et al., 1997).

The thermal load required by the flexural uplift model has also been supported by previous tomographic studies (Bannister et al., 2000; Morelli and Danesi, 2004; Watson et al., 2006; Lawrence et al., 2006b), which show slow and presumably hot upper mantle adjacent to the central TAMs in West Antarctica, extending beneath the TAMs front. Recent results from Hansen et al. (2014) and Graw et al. (2014) based on the TAMNNET data suggest these slow, hot mantle perturbations continue beneath the northern TAMs as well, coincident with Terror Rift. Taking all of these observations into account, including those from the current study, the

crustal thickness estimates best support a flexural model for the formation of the TAMs and WSB.

5.3 Average Crustal Shear Velocities

The mean crustal shear-wave velocities from the current study are also generally consistent with Hansen et al. (2009), who found average crustal V_s ranging between 3.6 and 3.7 km/s. The mid-crustal velocities (3.4-3.8 km/s) found by Bannister et al. (2003) are also consistent with the findings presented here. Pyle et al. (2010) generated S-wave velocity models for the TAMs, the Ross Sea, and the EA craton between 0-45 km depth. While these models are more detailed than the average crustal shear velocities determined in the current study, the crustal velocities beneath the TAMs and the EA craton range between 3.3-3.9 km/s (Pyle et al., 2010). These estimates match the average values found beneath TAMNNET, which range from 3.4-3.8 km/s. As mentioned in section 4.2, the inferred velocities beneath the KOPRI stations (3.3-3.5 km/s) were taken from Park (2014, personal communication), and these values are well matched with those from Finotello et al. (2009) and Lawrence et al. (2006a).

It is difficult to draw any direct conclusions about the uplift of the TAMs or the formation of the WSB from the average crustal S-wave velocities alone. However, noticeably slower crustal velocities are observed beneath stations within 50 km of the coast (Fig. 14). This is noteworthy since this area coincides with the slow, warm upper mantle that is interpreted to have spread beneath the TAMs front, as described in the previous section (Bannister et al., 2000; Morelli and Danesi, 2004; Watson et al., 2006; Hansen et al., 2014; Graw et al., 2014). It is possible that these warm upper mantle temperatures may also affect crustal velocities. That is, the crust would be slowly heated and weakened by this upper mantle heat source, thus lowering

the associated crustal velocities. Similar to the observed crustal structure, this explanation is consistent with the flexure model for the TAMs uplift, where the effective lithospheric thickness decreases near the coast (Stern and ten Brink, 1989; ten Brink and Stern, 1992; ten Brink et al., 1997).

5.4 Broader Significance

5.4.1 Comparison to Continental-scale Antarctic Models

The results from the current study can also be compared to continental-scale models of crustal thickness beneath Antarctica, most of which have been published in the last 5 years. These models have been generated using a variety of techniques. For example, Block et al. (2009) inverted Gravity Recovery and Climate Experiment (GRACE) satellite data to estimate Moho depth beneath both East and West Antarctica. Baranov and Morelli (2013) used a gridded model of previously published, seismically-determined crustal thicknesses to develop their continental-scale model, and O'Donnell and Nyblade (2014) combined previously acquired seismic data with multiple gravity satellite acquisitions. Overall, the crustal thickness estimates from TAMNNET agree well with these continental studies. The ~42 km thick crust beneath the EA craton found here is similar to the average EA crustal thicknesses of 40 km, 39 km, and 41 km reported by Block et al. (2009), Baranov and Morelli (2013), and O'Donnell and Nyblade (2014), respectively.

The increased crustal thickness beneath TAMNNET Line 1A observed in this study also generally agrees with the three continental-scale models outlined above; however, there are differences in the maximum measured thicknesses. Block et al. (2009) indicated that the maximum crustal thickness in the vicinity of TAMNNET is ~40-42 km, rather than ~47 km. It

should be noted that their map was derived using long wavelength features, so a crustal root of limited lateral extent may be too small for their model to resolve. Similarly, Baranov and Morelli (2013) reported a maximum crustal thickness near TAMNNET of ~40 km. This study incorporated crustal thickness estimates from Lawrence et al. (2006a). Hansen et al. (2009) showed that the crustal estimates beneath ice stations from Lawrence et al. (2006a) are too thin (by up to 9 km), likely due to problematic velocities used in their inversion. Therefore, this may have potentially skewed the Baranov and Morelli (2013) model and could account for the thinner values beneath the TAMs. The crustal thicknesses reported by O'Donnell and Nyblade (2014) are consistent with the current study, with a maximum thickness under the TAMs of ~45 km.

Crustal thicknesses beneath the WSB vary quite a bit between the continental-scale models. Block et al. (2009) and Baranov and Morelli (2013) both indicated thin WSB crust (~31-35 km), similar to Lawrence et al. (2006a) and Ferraccioli et al. (2001). However, O'Donnell and Nyblade (2014) found no difference in the crustal thickness between the EA craton and the WSB, with both regions having a thickness of ~40 km. This later estimate agrees with the crustal thickness of ~38-44 km found inland, behind the TAMs in the current study. Overall, while some differences in the crustal thickness values beneath the TAMs and WSB are observed between the current study and previous continental-scale models, the general structure and Moho depth, particularly beneath the TAMs and the EA craton, agree with one another. The results from the current TAMNNET study provide important confirmation for these broader-scale studies.

5.4.2 Comparison to Other Cratonic Environments

The crustal thickness estimates beneath the EA craton reported here are also consistent with those of other Precambrian terrains. As shown in Table 3, the total crustal thickness under East Antarctica ranges from ~38-44 km, averaging ~42 km. When, for instance, these values are

compared to the 36-46 km thick Archean crust in Australia (Reading et al., 2003; Goleby et al., 2004) and the 32-45 km thick Archean crust in Africa (Kgaswane et al., 2009; Nair et al., 2006), it is clear that the range and average thickness of the East Antarctic crust is consistent with both regions. Some studies have suggested that there are significant crustal thickness differences between Archean- and Proterozoic-aged crust. For example, Nguuri et al. (2001) observed crustal thicknesses between 35-40 km beneath Archean terrains in Africa but 45-50 km thick crust beneath Proterozoic regions. Mooney et al. (1998), who examined the crustal structure globally, also found Archean crust to be thinner (~40 km) than Proterozoic crust (42-46 km). However, other studies find no thickness differences between Precambrian crust of different age (e.g., Rudnick and Gao, 2003). Taking the full range of EA craton crustal thicknesses beneath TAMNNET into account, it is difficult to assess a specific, corresponding age associated with the study area. Regardless, the estimated crustal thicknesses determined in this study fit well within the global values for Precambrian crust.

6.0 CONCLUSIONS

Using SRFs, PRFs, and Rayleigh wave phase velocities, this study estimates the crustal thickness and average crustal shear-wave velocities beneath the northern TAMs and WSB. Ice thicknesses have also been determined as part of the analysis, from both PRFs and the BEDMAP2 model (Fretwell et al., 2013). Data are from the newly deployed TAMNNET array and five stations operated by KOPRI. The findings from this study provide new constraints on the crustal structure beneath a previously unexplored portion of the northern TAMs and, when compared to previous investigations further to the south, provide insight into along-strike variations. A better understanding of the tectonic structure of the TAMs and WSB, as well as of Antarctica in general, is beneficial to the study of non-compressional mountain uplift, supercontinent reconstruction, and can be used by other scientists for climate and ice sheet modeling. Crustal thicknesses, in particular, are a necessary constraint for modeling the long-term changes in the ice sheets covering Antarctica.

Ice thicknesses range between 0 and 2.85 km across the study area. The crust is thin (13-30 km) near the Ross Sea coast but is consistently thicker (~42 km) inland beneath the EA craton and the WSB. A crustal thickness of ~47 km is observed beneath the higher elevations in the TAMs, but this increased thickness is not a continuous feature along-strike of the mountain range. S-wave velocities range from 3.3 – 3.8 km/s, with slower velocities found only in the vicinity of the Ross Sea coast.

Given the results of this study, it has been concluded that a flexural model, where East Antarctica is an elastic plate with a free edge beneath the TAMs (Stern and ten Brink, 1989; ten Brink and Stern, 1992; ten Brink et al., 1997), best explains both the uplift of the mountain range and the formation of the WSB. This conclusion is supported by multiple lines of evidence. First, no crustal root of sufficient thickness is present to completely isostatically support the TAMs. Given the elevations along the TAMNET profiles, such isostatic support would require an additional ~8-10 km of crust under the TAMs, which is not observed. Second, a small root (3-5 km) is present under the TAMs, as is indicated by the thicker crust beneath TAMNET Line 1A (Fig. 13a); however, since this is not a continuous feature along-strike, it does not support uplift models which require a consistent root beneath the TAMs. Third, the observed crustal thickness (~42 km) beneath the WSB is thicker than that indicated by previous studies (Ferraccioli et al., 2001; Studinger et al., 2004; Lawrence et al., 2006a), which suggested the WSB is associated with rifting. Instead, the uniform crustal thickness seen beneath the EA craton and WSB in this study is consistent with the flexure model, where the WSB down-warped in relation to the uplift of the TAMs. Finally, the lower average V_s near the coast (Fig. 14) may reflect weakened crust, heated from anomalously warm upper mantle in adjacent West Antarctica, which would provide the required thermal load for the flexure model (Bannister et al., 2000; Morelli and Danesi, 2004; Watson et al., 2006; Hansen et al., 2014; Graw et al., 2014).

The flexure model supported by the current results was also supported by Hansen et al. (2009), who examined the crustal structure beneath the TAMSEIS array further to the south. Both studies observe thin crust near the Ross Sea coast, with thicker crust inland, and these findings closely match the expected crustal structure described by Stern and ten Brink (1989), ten Brink and Stern (1992), and ten Brink et al. (1997). Locally thicker crust (~47 km) beneath

the TAMNNET array can explain the extra topography beneath the northern TAMs as compared to the TAMSEIS counterpart in the central TAMs.

REFERENCES

- Ammon, C. J., (1991). The Isolation of Receiver Effects from Teleseismic P Waveforms. *Bulletin of the Seismological Society of America*, 81(6), 2504-2510.
- Ammon, C. J., G. E. Randall, G. Zandt, (1990). On the Nonuniqueness of Receiver Function Inversions. *Journal of Geophysical Research-Solid Earth and Planets*, 95(B10), 15303-15318. doi: 10.1029/JB095iB10p15303.
- Bannister, S., R. K. Snieder and M. L. Passier, (2000). Shear-wave Velocities under the Transantarctic Mountains and Terror Rift from Surface Wave Inversion. *Geophysical Research Letters*, 27(2), 281-284. doi: 10.1029/1999gl010866.
- Bannister, S., J. Yu, B. Leitner and B. L. N. Kennett, (2003). Variations in Crustal Structure across the Transition from West to East Antarctica, Southern Victoria Land. *Geophysical Journal International*, 155(3), 870-884. doi: 10.1111/j.1365-246X.2003.02094.x.
- Baranov, A., A. Morelli (2013). The Moho depth map of the Antarctica region. *Tectonophysics*, 609, 299-313. doi: 10.1016/j.tecto.2012.12.023.
- Bialas, R. W., W. R. Buck, M. Studinger, P. G. Fitzgerald, (2007) Plateau Collapse Model for the Transantarctic Mountains-West Antarctic Rift System: Insights from Numerical Experiments. *Geology*, 35(8), 687-690. doi: 10.1130/G23825A.1.
- Block, A. E., R. E. Bell, M. Studinger, (2009). Antarctic crustal thickness from satellite gravity: Implications for the Transantarctic and Gamburtsev Subglacial Mountains. *Earth and Planetary Science Letters*, 288(1-2), 194-203. doi: 10.1016/j.epsl.2009.09.022.
- Drewry, D. J., (1976) Sedimentary Basins of the East Antarctic Craton from Geophysical Evidence. *Tectonophysics*, 36(1-3), 301-314. doi: 10.1016/0040-1951(76)90023-8.
- Enright, K., (2010). *America's Natural Places: Rocky Mountains and the Great Plains*. Greenwood Publishing Group, Santa Barbra, CA.
- Farra, V., L. Vinnik, (2000). Upper Mantle Stratification by P and S Receiver Functions. *Geophysical Journal International*, 141(3), 699-712. doi: 10.1046/j.1365-246x.2000.00118.x.

- Federico, L., L. Crispini, G. Capponi, J. D. Bradshaw, (2009). The Cambrian Ross Orogeny in Northern Victoria Land (Antarctica) and New Zealand: A Synthesis. *Gondwana Research*, 15(2), 188-196. doi: 10.1016/j.gr.2008.10.004.
- Ferraccioli, F., F. Coren, E. Bozzo, C. Zanolla, S. Gandolfi, I. Tabacco, M. Frezzotti, (2001) Rifted(?) Crust at the East Antarctic Craton Margin: Gravity and Magnetic Interpretation along a Traverse Across the Wilkes Subglacial Basin Region. *Earth and Planetary Science Letters*, 192(3), 407-421. doi: 10.1016/S0012-821X(01)00459-9.
- Ferraccioli, F., E. Armadillo, T. Jordan, E. Bozzo, H. Corr, (2009). Aeromagnetic Exploration over the East Antarctic Ice Sheet: A New View of the Wilkes Subglacial Basin. *Tectonophysics*, 478(1-2), 62-77. doi: 10.1016/j.tecto.2009.03.013.
- Finotello, M., (2009) Crustal Structure Along the Transantarctic Mountains Front Using Receiver Functions. M.S. Thesis, The Pennsylvania State University.
- Fitzgerald, P. G., (1992). The Transantarctic Mountains of Southern Victoria Land: The Application of Apatite Fission Track Analysis to a Rift Shoulder Uplift. *Tectonics*, 11(3), 634-662. doi: 10.1029/91TC02495.
- Fitzgerald, P. G., (2002). Tectonics and Landscape Evolution of the Antarctic Plate Since the Breakup of Gondwana, with an Emphasis on the West Antarctic Rift System and the Transantarctic Mountains. *Royal Society of New Zealand Bulletin*, 35, 453-469.
- Fitzgerald, P. G., M. Sandiford, P. J. Barrett, and A. J. W. Gleadow (1986). Asymmetric Extension Associated with Uplift and Subsidence in the Transantarctic Mountains and Ross Embayment. *Earth and Planetary Science Letters*, 81, 67-78. doi: 10.1016/0012-821X(86) 90101-9.
- Fretwell, P., H. D. Pritchard, D.G. Vaughan and B. Consortium (2013). Bedmap2: Improved Ice Bed, Surface and Thickness Datasets for Antarctica. *Cryosphere*, 7(1), 375-393. doi: 10.5194/tc-7-375-2013.
- Goleby, B. R., R. S. Blewett, R. J. Korsch, D. C. Champion, K. F. Cassidy, L. E. A. Jones, P. B. Groenewald, P. Henson (2004). Deep seismic reflection profiling in the Archean northeastern Yilgarn Craton, Western Australia: implications for crustal architecture and mineral potential. *Tectonophysics*, 388(1-4), 119-133. doi: 10.1016/j.tecto.2004.04.032.
- Graw, J. H., S.E. Hansen, A. Adams (2014). Upper Mantle Shear Wave Velocity Structure beneath the Transantarctic Mountains and Eastern Wilkes Subglacial Basin. *Geological Society of America Conference*, Abstract 246667.
- Hansen, S. E., J. Julia, A. A. Nyblade, M. L. Pyle, D. A. Wiens, and S. Anandakrishnan, (2009). Using S wave Receiver Functions to estimate Crustal Structure beneath Ice Sheets: An Application to the Transantarctic Mountains and East Antarctic Craton. *Geochemistry, Geophysics, Geosystems*, 10. doi: 10.1029/2009gc002576.

- Hansen, S. E., A. A. Nyblade, D. S. Heeszel, D. A. Wiens, P. Shore, and M. Kanao, (2010). Crustal Structure of the Gamburtsev Mountains, East Antarctica, from S-wave Receiver Functions and Rayleigh Wave Phase Velocities. *Earth and Planetary Science Letters*, 300(3-4), 395-401. doi: 10.1016/j.epsl.2010.10.022.
- Hansen, S. E., J. H. Graw, L. M. Kenyon, A. A. Nyblade, D. A. Wiens, R. C. Aster, A. D. Huerta, S. Anandkrishnan, T. Wilson, (2014). Imaging the Antarctic Mantle using Adaptively Parameterized P-wave Tomography: Evidence for Heterogeneous Structure beneath West Antarctica. *Earth and Planetary Science Letters*, 408, 66-78. doi: 10.1016/j.epsl.2014.09.043.
- Huerta, A. D., D. L. Harry, (2007). The Transition from Diffuse to Focused Extension: Modeled Evolution of the West Antarctic Rift System. *Earth and Planetary Science Letters*, 255(1-2), 133-147. doi: 10.1016/j.epsl.2006.12.011.
- Julia, J., R. B. Herrmann, C. J. Ammon, A. Akinci, (2004). Evaluation of Deep Sediment Velocity Structure in the New Madrid Seismic Zone. *Bulletin of the Seismological Society of America*, 94(1), 334-340. doi: 10.1785/0120030081.
- Kalamarides, R. I., J. H. Berg, R. A. Hank, (1987). Lateral Isotopic Discontinuity in the Lower Crust: An Example from Antarctica. *Science*, 237(4819), 1192-1195. doi: 10.1126/science.237.4819.1192.
- Kgaswane, E. M., A. A. Nyblade, J. Julia, P. H. G. M. Dirks, R. J. Durrheim, M. E. Pasyanos (2009). Shear wave velocity structure of the lower crust in southern Africa: Evidence for compositional heterogeneity within Archaean and Proterozoic terrains. *Journal of Geophysical Research-Solid Earth*, 114, B12304. doi: 10.1029/2008JB006217.
- Kim, K. Y., M. H. Hong, J. Lee, J. K. Hong, and Y. K. Jin (2007), Seismic Experiments on the Fourcade Glacier in the King George Island, Antarctica. *Geophysical Research Abstracts*, 9, A-04755.
- Kumar, P., R. Kind, W. Hanka, K. Wylegalla, C. Reigber, X. Yuan, I. Woelbern, P. Schwintzer, K. Fleming, T. Dahl-Jensen, T. B. Larsen, J. Schweitzer, K. Priestly, O. Gudmundsson, D. Wolf, (2005). The Lithosphere-Asthenosphere Boundary in the North-West Atlantic Region. *Earth and Planetary Science Letters*, 236(1-2), 249-257. doi: 10.1016/j.epsl.2005.05.029.
- Langston, C. A., (1977). The Effect of Planar Dipping Structure on Source and Receiver Responses for a Constant Ray Parameter. *Bulletin of the Seismological Society of America*, 67(4), 1029-1050.
- Langston, C. A., (1979). Structure Under Mount Rainier, Washington, Inferred From Teleseismic Body Waves. *Journal of Geophysical Research*, 84(NB9), 4749-4762. doi: 10.1029/JB084iB09p04749.

- Last, R. J., A. A. Nyblade, C. A. Langston, and T. J. Owens, (1997). Crustal Structure of the East African Plateau from Receiver Functions and Rayleigh Wave Phase Velocities. *Journal of Geophysical Research-Solid Earth*, 102(B11), 24469-24483. doi: 10.1029/97jb02156.
- Lawrence, J. F., D. A. Wiens, A. A. Nyblade, S. Anandakrishnan, P. J. Shore, and D. Voigt, (2006a). Crust and Upper Mantle Structure of the Transantarctic Mountains and Surrounding Regions from Receiver Functions, Surface Waves, and Gravity: Implications for Uplift Models. *Geochemistry, Geophysics, Geosystems*, 7. doi: 10.1029/2006gc001282.
- Lawrence, J. F., D. A. Wiens, A. A. Nyblade S. Anandakrishnan, P. J. Shore, D. Voigt, (2006b) Rayleigh Wave Phase Velocity Analysis of the Ross Sea, Transantarctic Mountains, and East Antarctica from a Temporary Seismograph Array. *Journal of Geophysical Research-Solid Earth*, 111(B6), B06302. doi: 10.1029/2005JB003812.
- Li, X. Q., R. Kind, X. H. Yuan, I. Wolbern, W. Hanka, (2004). Rejuvenation of the Lithosphere by the Hawaiian Plume. *Nature*, 427(6977), 827-829. doi: 10.1038/nature02349.
- Ligorria, J. P., and C. J. Ammon, (1999). Iterative Deconvolution and Receiver-Function Estimation. *Bulletin of the Seismological Society of America*, 89(5), 1395-1400.
- Lisker, F., A. L. Laufer, (2013). The Mesozoic Victoria Basin: Vanished Link between Antarctica and Australia. *Geology*, 41(10), 1043-1046. doi: 10.1130/G33409.1.
- Meert, J. G., (2003) A Synopsis of Events Related to the Assembly of Eastern Gondwana. *Tectonophysics*, 362(1-4), 1-40. doi: 10.1016/S0040-1951(02)00629-7.
- Mooney, W., G. Laske, and T. Masters (1998), CRUST 5.1: A global crustal model at $5^\circ \times 5^\circ$. *Journal of Geophysical Research-Solid Earth*, 103(B1), 727-747. doi: 10.1029/97JB02122.
- Morelli, A., S. Danesi, (2004) Seismological Imaging of the Antarctic Continental Lithosphere: A Review. *Global and Planetary Change*, 42(1-4) 155-165. doi: 10.1016/j.gloplacha.2003.12.005.
- Nair, S. K., S. S. Gao, K. H. Liu, P. G. Silver (2006). Southern African crustal evolution and composition: Constraints from receiver function studies. *Journal of Geophysical Research-Solid Earth*, 115(B2), B02304. doi: 10.1029/2005JB003802.
- Nguuri, T. K., J. Gore, D. E. James, S. J. Webb, C. Write, T. G. Zengeni, O. Gwavava, J. A. Snoke (2001). Crustal structure beneath Southern Africa and its implications for the formation and evolution of the Kaapvaal and Zimbabwe cratons. *Geophysical Research Letters*, 28(13), 2501-2504. doi: 10.1029/2000GL012587.

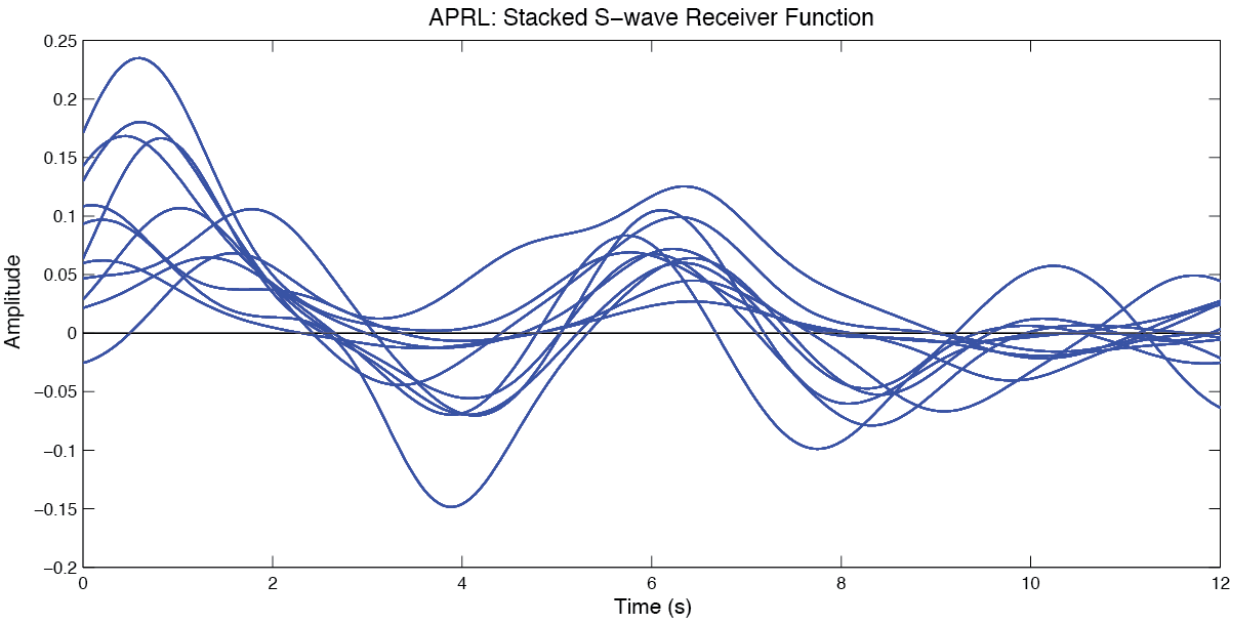
- O'Donnell, J. P., A. A. Nyblade, (2014), Antarctica's hypsometry and crustal thickness: Implications for the origin of anomalous topography in East Antarctica. *Earth and Planetary Science Letters*, 388, 143-155. doi: 10.1016/j.epsl.2013.11.051.
- Pyle, M. L., D. A. Wiens, A. A. Nyblade, S. Anandakrishnan, (2010). Crustal Structure of the Transantarctic Mountains near the Ross Sea from Ambient Seismic Noise Tomography. *Journal of Geophysical Research-Solid Earth*, 115, B11310. doi: 10.1029/2009JB007081.
- Reading, A. M., B. L. N. Kennett, M. C. Dentith (2003). Seismic structure of the Yilgarn Craton, Western Australia. *Australian Journal of Earth Sciences*, 50(3), 427-438. doi: 10.1046/j.1440-0952.2003.01000.x.
- Ritzwoller, M. H., N. M. Shapiro, A. L. Levshin, G. M. Leahy, (2001). Crustal and Upper Mantle Structure beneath Antarctica and Surrounding Oceans. *Journal of Geophysical Research-Solid Earth*, 106(B12), 30645-30670. doi: 10.1029/2001JB000179.
- Robinson, E. S., J. F. Splettstoesser, (1984). Structure of the Transantarctic Mountains Determined from Geophysical Surveys, in *Geology of the Central Transantarctic Mountains*, *Antarctic Research Series*, 36, 119-162.
- Rudnick, R., S. Gao (2003). Composition of the continental crust, in *The Crust, Treatise on Geochemistry*, 3, edited by H.D. Holland and K. K. Turekian, pp. 1-64, Elsevier, Oxford, U. K.
- Salvini, F., G. Brancolini, M. Buseti, F. Storti, F. Mazzarini, F. Coren, (1997). Cenozoic Geodynamics of the Ross Sea Region, Antarctica: Crustal Extension, Intraplate Strike-slip Faulting, and Tectonic Inheritance. *Journal of Geophysical Research-Solid Earth*, 102(B11) 24669-24696. doi: 10.1029/97JB01643.
- Smith, A. G., D. J. Drewry, (1984). Delayed Phase Change due to Hot Asthenosphere Causes Transantarctic Uplift. *Nature*, 309(5968) 536-538. doi: 10.1038/309536a0
- Stern, T. A., and U. S. ten Brink, (1989). Flexural Uplift of the Transantarctic Mountains. *Journal of Geophysical Research-Solid Earth and Planets*, 94(B8), 10315-10330. doi: 10.1029/JB094iB08p10315.
- Storti, F., M. L. Balestrieri, F. Balsamo, F. Rossetti, (2008). Structural and thermochronological constraints to the evolution of the West Antarctic Rift System in central Victoria Land. *Tectonics*, 27, TC4012. doi: 10.1029/2006TC002066.
- Studinger, M., R. E. Bell, W. R. Buck, G. D. Karner, and D. D. Blankenship, (2004). Sub-ice Geology Inland of the Transantarctic Mountains in Light of New Aerogeophysical Data. *Earth and Planetary Science Letters*, 220(3-4), 391-408. doi: 10.1016/s0012-821x(04)00066-4.

- ten Brink, U. S., T. Stern, (1992). Rift Flank Uplifts and Hinterland Basins: Comparison of the Transantarctic Mountains with the Great Escarpment of South Africa. *Journal of Geophysical Research*, 97(B1), 569-585. doi: 10.1029/91JB02231.
- ten Brink, U. S., S. Bannister, B. C. Beaudoin, T. A. Stern, (1993). Geophysical Investigations of the Tectonic Boundary between East and West Antarctica. *Science*, 261(5117), 45-50.
- ten Brink, U. S., R. I. Hackney, S. Bannister, T. A. Stern, and Y. Makovsky, (1997). Uplift of the Transantarctic Mountains and the Bedrock beneath the East Antarctic Ice Sheet. *Journal of Geophysical Research-Solid Earth*, 102(B12), 27603-27621. doi: 10.1029/97jb02483.
- Torsvik, T. H., (2003). The Rodinia Jigsaw Puzzle. *Science*, 300(5624), 1379-1381. doi: 10.1126/science.1083469.
- Turcotte, D. L., G. Schubert, (2002) *Geodynamics*, 2nd Edition, Cambridge University Press, New York, NY.
- Watson, T., A. Nyblade, D. A. Wiens, S. Anandakrishnan, M. Benoit, P. J. Shore, D. Voigt, J. VanDecar, (2006). P and S Velocity Structure of the Upper Mantle beneath the Transantarctic Mountains, East Antarctic Craton, and Ross Sea from Travel Time tomography. *Geochemistry, Geophysics, Geosystems*, 7. doi: 10.1029/2005GC001238.
- Wilson, D. C., D. A. Angus, J. F. Ni, and S. P. Grand, (2006). Constraints on the Interpretation of S-to-P Receiver Functions. *Geophysical Journal International*, 165(3), 969-980. doi: 10.1111/j.1365-246X.2006.02981.x.
- Zelt, B. C., R. M. Ellis, (1999). Receiver-Function Studies in the Trans-Hudson Orogen, Saskatchewan. *Canadian Journal of Earth Sciences*, 36(4), 585-603. doi: 10.1139/e98-109.
- Zhu, L. P., H. Kanamori, (2000). Moho Depth Variation in Southern California from Teleseismic Receiver Functions. *Journal of Geophysical Research-Solid Earth*, 105(B2), 2969-2980. doi: 10.1029/1999JB00322.

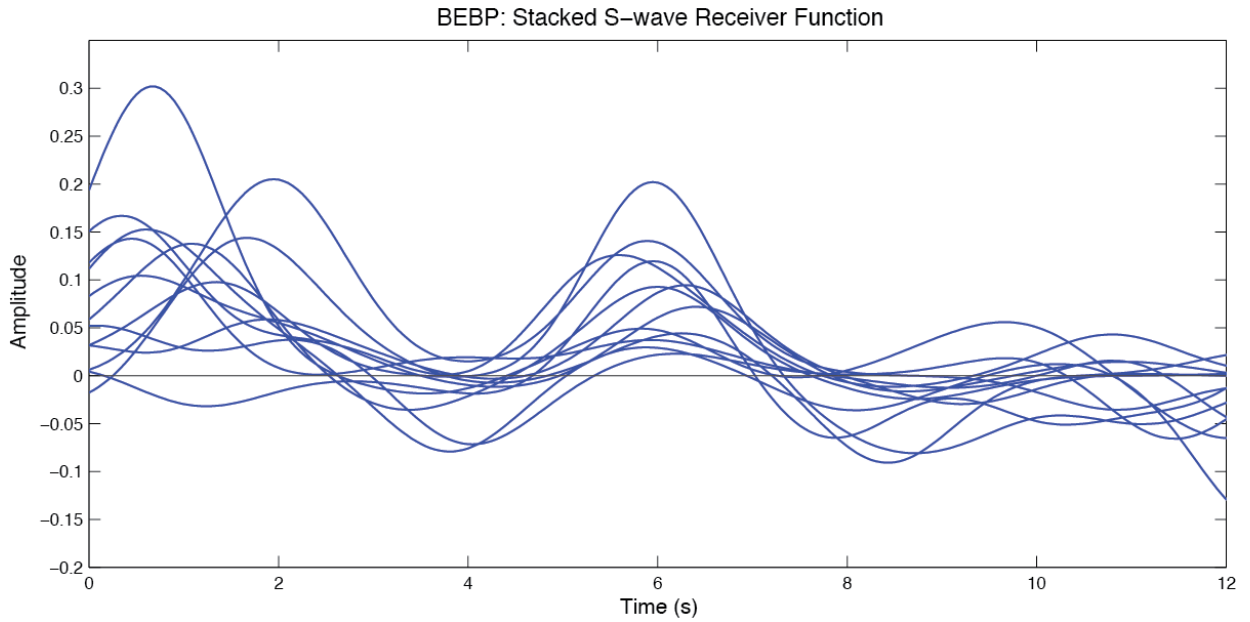
APPENDIX A

This appendix contains the pre-stacked, individual SRF responses for the analyzed TAMNNET stations. Each page includes a table, listing the events used for the given station, along with a plot showing the individual SRFs used to generate the stack. Stations are shown in alphabetical order. Since crustal thicknesses for the KOPRI stations were ultimately taken from the PRF results of Park (2014, personal communication), these stations are not included here.

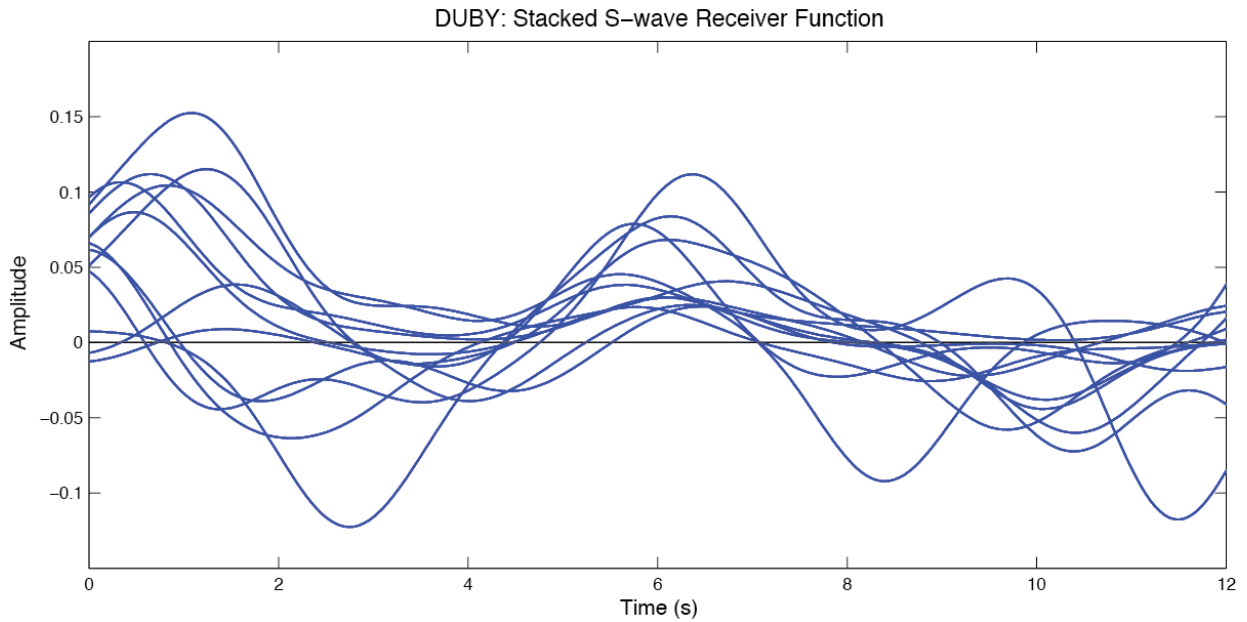
APRL Event #	Date	Julian day	Time	Latitude (°)	Longitude (°)	Depth km	Mag.
1	NOV 28 2012	333	08.56.16	-5.398	131.134	50.3	5.6
2	DEC 15 2012	350	19.30.02	-4.632	153.016	52	6.1
3	JAN 31 2013	031	03.57.56	-10.682	166.381	10	5.8
4	JAN 31 2013	031	05.18.09	-10.059	166.361	10	5.5
5	FEB 07 2013	038	08.03.40	-11.030	164.778	11	5.8
6	FEB 17 2013	048	19.23.45	-10.808	165.555	10	5.7
7	FEB 23 2013	054	08.59.08	-10.660	165.304	12	6.1
8	FEB 23 2013	054	11.09.19	-8.467	127.467	20	5.9
9	APR 14 2013	104	01.32.22	-6.475	154.607	31	6.5
10	OCT 16 2013	289	10.31.01	-6.490	154.920	58.2	7.1
11	OCT 31 2013	304	23.03.56	-30.314	-71.733	10.7	6.6



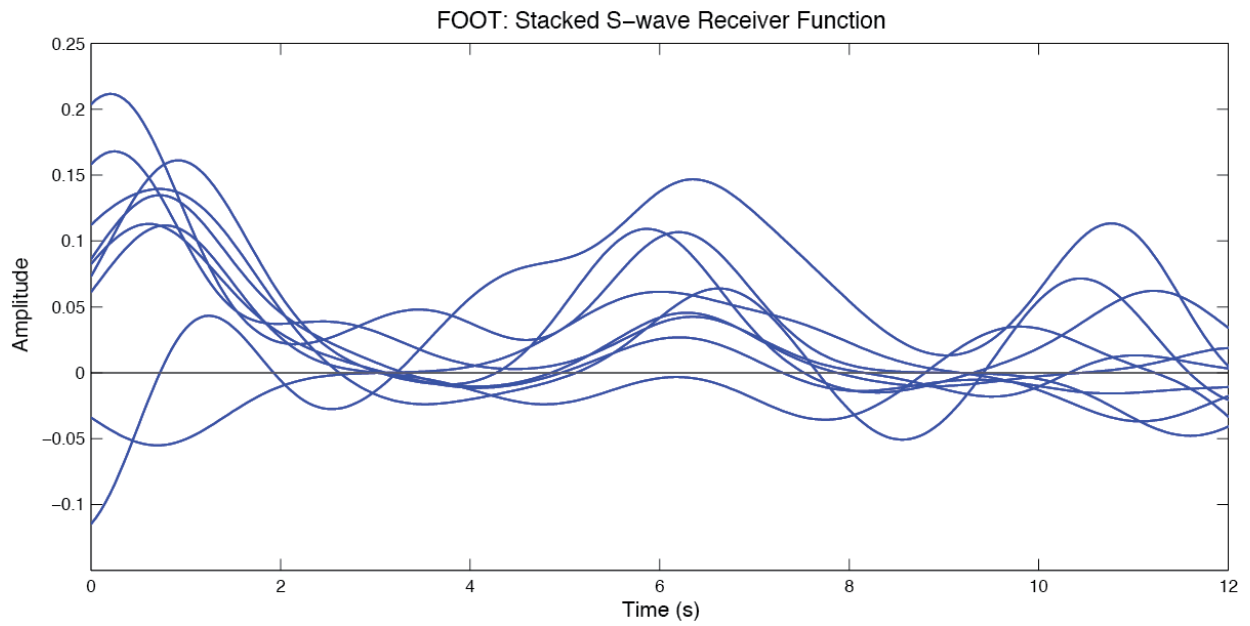
BEBP Event #	Date	Julian day	Time	Latitude (°)	Longitude (°)	Depth km	Mag.
1	DEC 10 2012	345	16.53.08	-6.533	129.825	155	7.1
2	DEC 15 2012	350	19.30.02	-4.632	153.016	52	6.1
3	JAN 30 2013	030	20.15.43	-28.094	-70.653	45	6.8
4	FEB 07 2013	038	00.30.10	-11.658	164.940	0.8	6.0
5	FEB 11 2013	042	09.40.19	-11.046	166.800	10	5.7
6	FEB 13 2013	044	10.08.50	-10.789	164.255	19.8	5.5
7	FEB 17 2013	048	19.23.45	-10.808	165.555	10	5.7
8	MAR 10 2013	069	16.49.19	-5.299	151.519	60	5.7
9	APR 20 2013	110	03.42.02	-5.002	152.111	65.3	5.6
10	OCT 16 2013	289	10.31.01	-6.490	154.920	58.2	7.1
11	OCT 30 2013	303	02.51.50	-35.297	-72.930	17.8	6.2
12	NOV 02 2013	306	15.52.46	-23.566	-112.610	.53	5.8



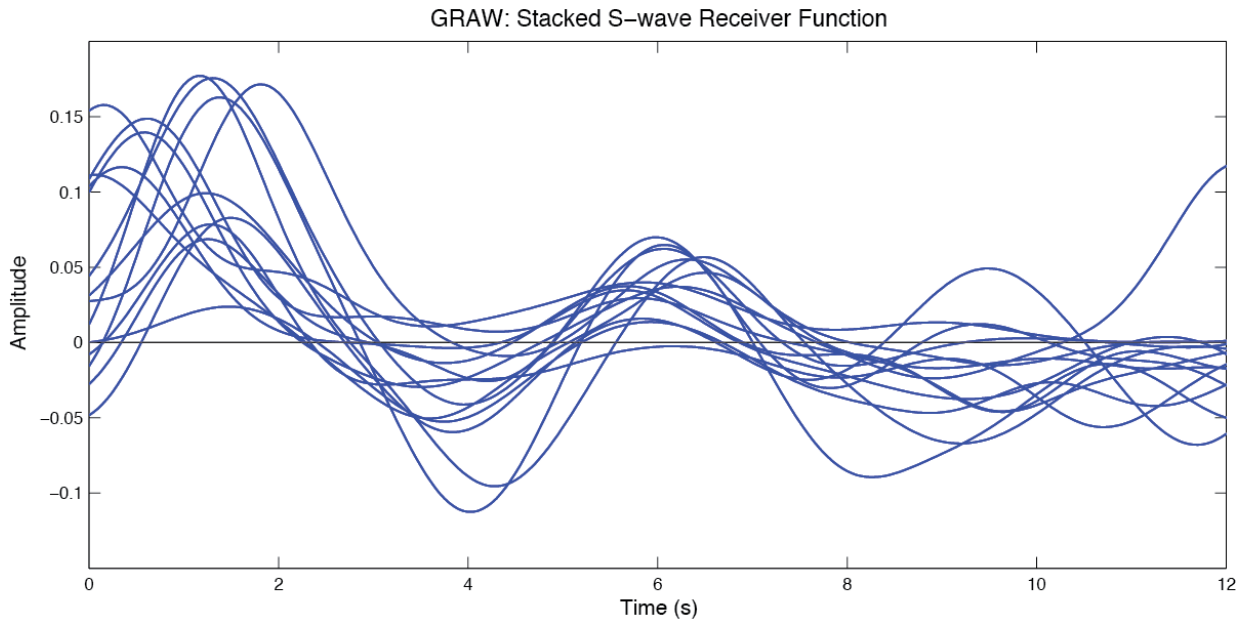
DUBY Event #	Date	Julian day	Time	Latitude (°)	Longitude (°)	Depth km	Mag.
1	DEC 10 2012	345	16.53.08	-6.533	129.825	155	7.1
2	DEC 11 2012	346	06.18.27	0.533	126.231	30	6.0
3	JAN 27 2013	027	09.59.29	-16.117	-173.235	19	5.7
4	FEB 01 2013	032	05.36.41	-11.104	165.532	15	6.0
5	FEB 07 2013	038	18.59.16	-10.997	165.655	11	6.7
6	FEB 23 2013	054	08.59.08	-10.660	165.304	12	6.1
7	APR 06 2013	096	04.42.35	-3.517	138.476	66	7.0
8	JUN 05 2013	156	04.47.26	-11.401	166.299	39	6.1
9	AUG 12 2013	224	00.53.43	-7.147	129.813	95	6.1
10	SEP 01 2013	244	11.52.29	-7.437	128.218	112	6.5
11	SEP 05 2013	248	15.27.02	-7.240	144.057	7.3	5.5
12	OCT 31 2013	304	23.03.56	-30.314	-71.733	10.7	6.6



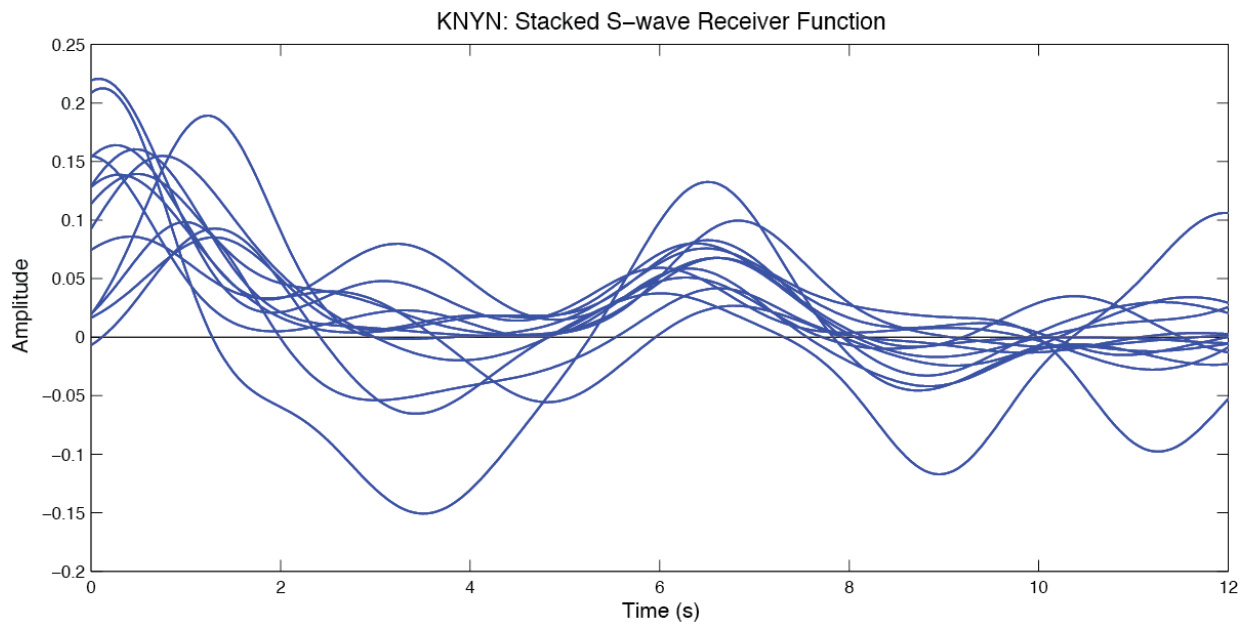
FOOT Event #	Date	Julian day	Time	Latitude (°)	Longitude (°)	Depth km	Mag.
1	JAN 30 2013	030	20.15.43	-28.094	-70.653	45	6.8
2	FEB 01 2013	032	02.17.27	-6.957	147.676	44.1	5.8
3	FEB 01 2013	032	05.36.41	-11.104	165.532	15	6.0
4	FEB 02 2013	033	18.58.06	-10.887	165.284	6	5.9
5	FEB 06 2013	037	11.53.55	-11.243	165.728	14	6.0
6	MAR 11 2013	070	17.12.13	-11.531	165.186	10	5.5
7	APR 14 2013	104	01.32.22	-6.475	154.607	31	6.5
8	OCT 16 2013	289	10.31.01	-6.490	154.920	58.2	7.1
9	OCT 31 2013	304	23.03.56	-30.314	-71.733	10.7	6.6



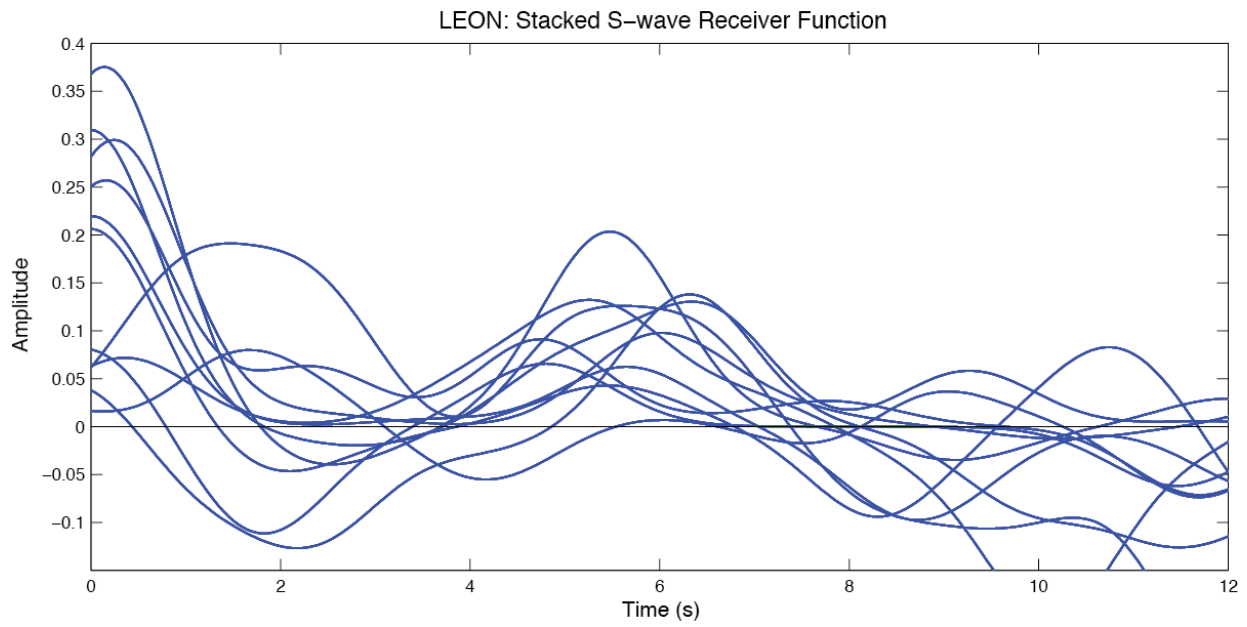
GRAW Event #	Date	Julian day	Time	Latitude (°)	Longitude (°)	Depth km	Mag.
1	NOV 19 2012	324	09.44.34	-5.705	151.602	13	6.0
2	NOV 21 2012	326	21.36.22	-33.939	-71.868	18	5.9
3	DEC 07 2012	342	19.50.23	-7.661	146.954	139.8	5.7
4	DEC 08 2012	343	16.35.16	-7.211	143.973	10	5.6
5	DEC 15 2012	350	19.30.02	-4.632	153.016	52	6.1
6	FEB 01 2013	032	05.36.41	-11.104	165.532	15	6.0
7	FEB 23 2013	054	11.09.19	-8.467	127.467	20	5.9
8	APR 14 2013	104	01.32.22	-6.475	154.607	31	6.5
9	APR 16 2013	106	22.55.26	-3.214	142.542	13	6.6
10	APR 20 2013	110	04.51.12	-6.292	130.218	108.1	6.0
11	JUL 07 2013	188	20.30.06	-6.029	149.706	56	6.6
12	OCT 16 2013	289	10.31.01	-6.490	154.920	58.2	7.1
13	OCT 31 2013	304	23.03.56	-30.314	-71.733	10.7	6.6
14	NOV 19 2013	323	13.32.54	2.646	128.402	63.5	6.3



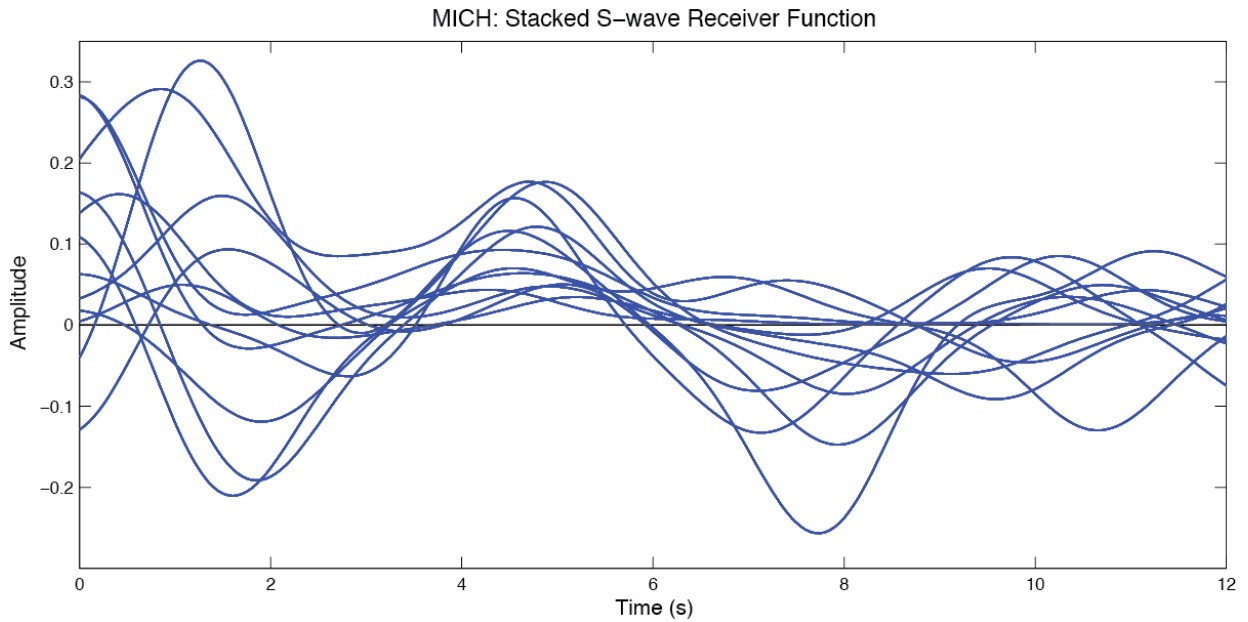
KNYN Event #	Date	Julian day	Time	Latitude (°)	Longitude (°)	Depth km	Mag.
1	DEC 20 2000	355	11.23.54	-39.019	-74.732	11	6.2
2	DEC 21 2000	356	01.01.34	-5.849	151.132	96.4	6.4
3	DEC 28 2000	363	04.34.28	-4.066	152.409	33	6.0
4	JAN 15 2001	015	03.47.24	-8.841	114.854	93.4	6.8
5	FEB 15 2001	046	12.46.59	-5.580	148.338	162	5.6
6	DEC 22 2001	356	00.40.04	-10.914	165.856	73.3	6.0
7	JAN 02 2002	002	15.21.23	-15.2	172.500	10	5.8
8	JAN 15 2002	015	09.01.17	-5.583	151.154	49.6	6.2
9	DEC 08 2012	343	16.35.16	-7.211	143.973	10	5.6
10	DEC 10 2012	345	16.53.08	-6.533	129.825	155	7.1
11	DEC 15 2012	350	19.30.02	-4.632	153.016	52	6.1
12	JUL 02 2013	183	20.04.55	-23.851	-66.516	198.9	5.6
13	JUL 07 2013	188	20.30.06	-6.029	149.706	56	6.6



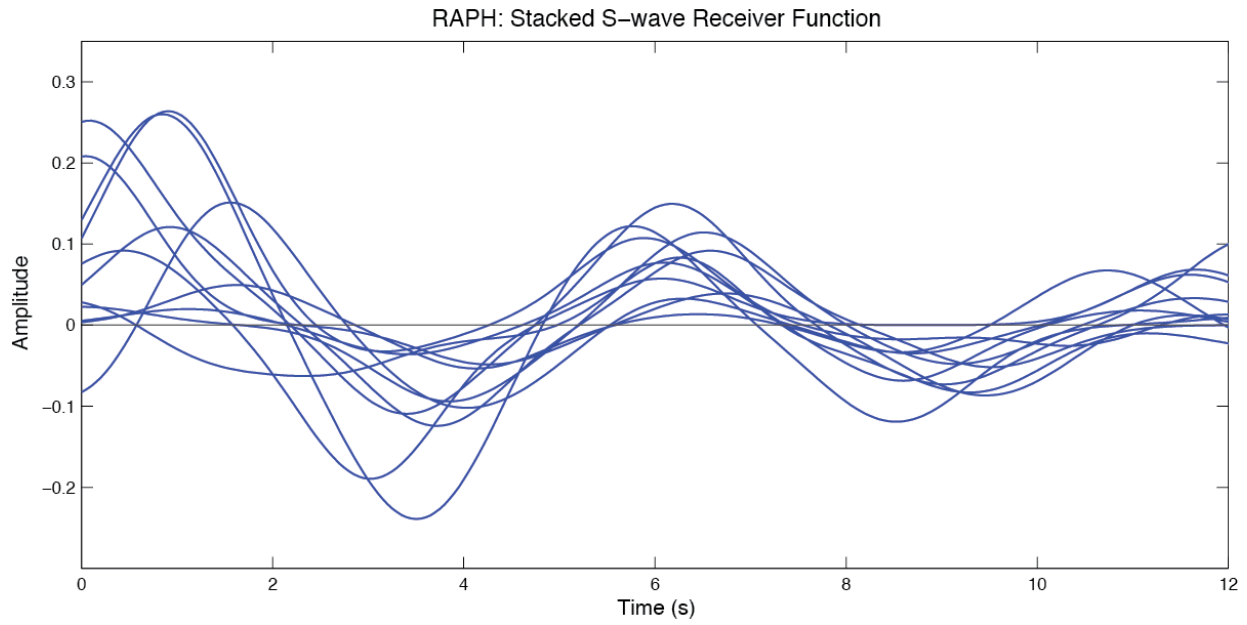
LEON Event #	Date	Julian day	Time	Latitude (°)	Longitude (°)	Depth km	Mag.
1	DEC 29 2012	364	07.59.41	-3.563	148.899	40	6.0
2	FEB 01 2013	032	02.17.27	-6.957	147.676	44.1	5.8
3	FEB 07 2013	038	08.03.40	-11.030	164.778	11	5.8
4	FEB 28 2013	059	18.07.48	-10.892	165.921	39	5.8
5	APR 14 2013	104	01.32.22	-6.475	154.607	31	6.5
6	APR 19 2013	109	17.51.41	-11.976	121.632	15.2	5.8
7	MAY 10 2013	130	19.56.04	-28.983	-13.229	3.9	5.7
8	AUG 17 2013	229	16.32.31	-34.885	54.098	10	6.1
9	AUG 23 2013	235	08.34.06	-22.274	-68.593	111	5.8
10	SEP 01 2013	244	11.52.29	-7.437	128.218	112	6.5
11	OCT 31 2013	304	23.03.56	-30.314	-71.733	10.7	6.6



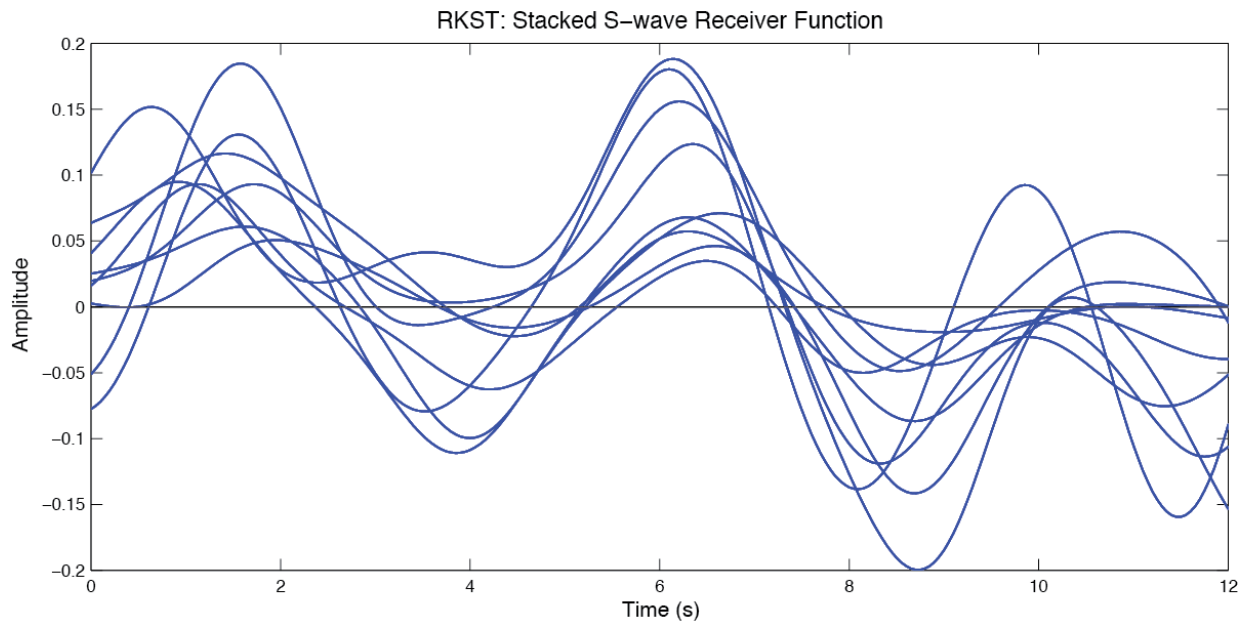
MICH Event #	Date	Julian day	Time	Latitude (°)	Longitude (°)	Depth km	Mag.
1	DEC 10 2012	345	16.53.08	-6.533	129.825	155	7.1
2	DEC 29 2012	364	07.59.41	-3.563	148.899	40	6.0
3	FEB 06 2013	037	22.20.20	-11.099	165.632	24.5	5.6
4	FEB 28 2013	059	18.07.48	-10.892	165.921	39	5.8
5	APR 20 2013	110	03.42.02	-5.002	152.111	65.3	5.6
6	APR 23 2013	113	19.56.04	-28.983	-13.229	10	6.5
7	MAY 10 2013	130	19.56.04	-28.983	-13.229	3.9	5.7
8	MAY 25 2013	145	10.32.54	-7.510	127.916	10	5.5
9	JUN 26 2013	177	22.59.00	-0.041	125.054	32.7	5.5
10	JUL 04 2013	185	17.15.54	-7.028	155.726	29	6.1
11	AUG 12 2013	224	00.53.43	-7.147	129.813	95	6.1
12	OCT 31 2013	304	23.03.56	-30.314	-71.733	10.7	6.6



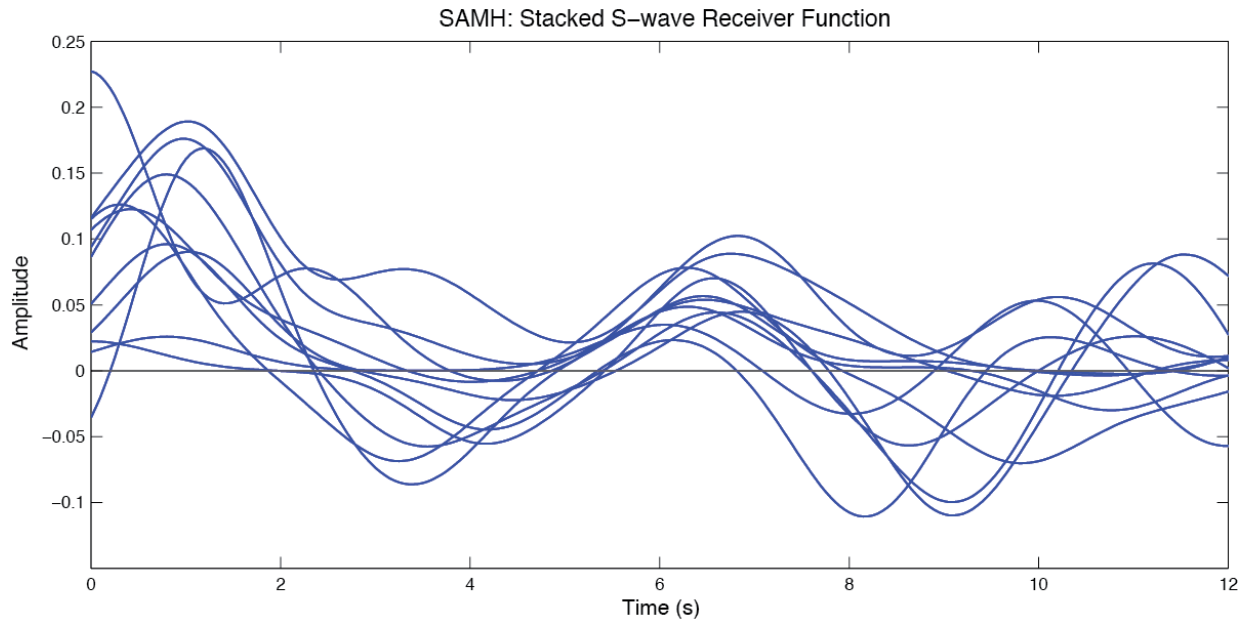
RAPH Event #	Date	Julian day	Time	Latitude (°)	Longitude (°)	Depth km	Mag.
1	DEC 15 2012	350	19.30.02	-4.632	153.016	52	6.1
2	FEB 17 2013	048	19.23.45	-10.808	165.555	10	5.7
3	MAR 05 2013	064	06.06.34	-5.214	152.559	22	5.8
4	APR 14 2013	104	01.32.22	-6.475	154.607	31	6.5
5	APR 17 2013	107	05.05.03	-2.768	138.750	50.4	5.6
6	JUN 19 2013	170	06.52.38	-3.766	151.400	10	5.5
7	JUL 04 2013	185	17.15.54	-7.028	155.726	29	6.1
8	JUL 07 2013	188	20.30.06	-6.029	149.706	56	6.6
9	JUL 09 2013	190	17.04.15	-3.359	100.458	17.5	5.5
10	AUG 23 2013	235	08.34.06	-22.274	-68.593	111	5.8
11	SEP 02 2013	245	04.30.16	-6.620	155.131	35	5.9



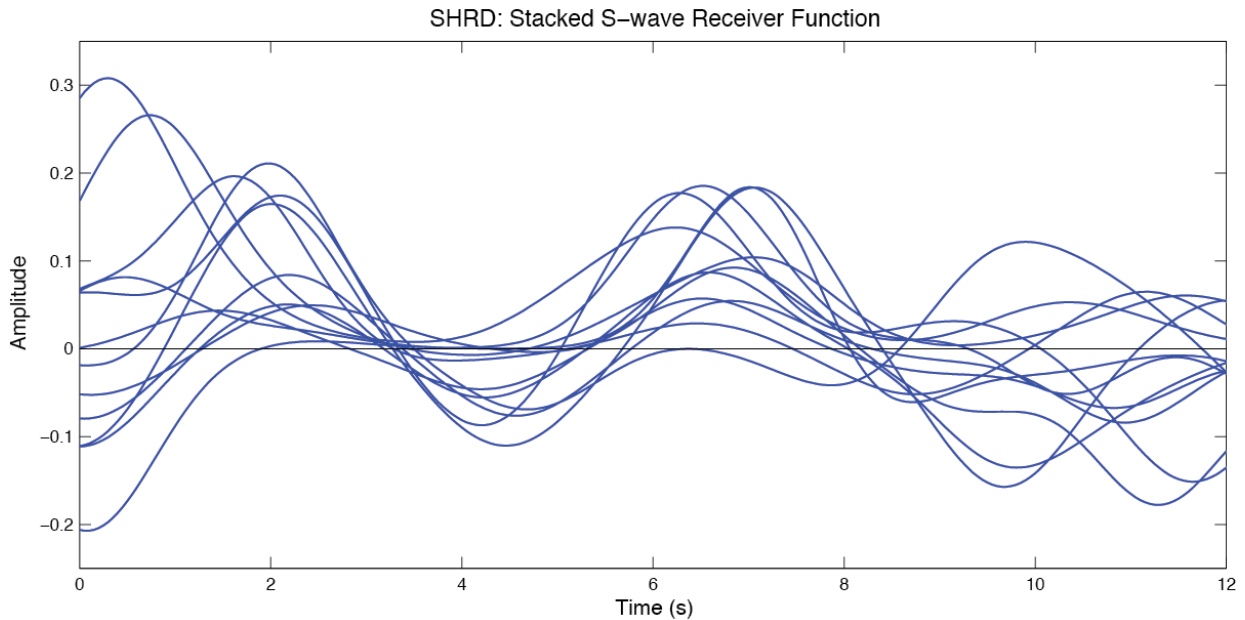
RKST Event #	Date	Julian day	Time	Latitude (°)	Longitude (°)	Depth km	Mag.
1	DEC 07 2012	342	19.50.23	-7.661	146.954	139.8	5.7
2	DEC 08 2012	343	16.35.16	-7.211	143.973	10	5.6
3	DEC 14 2012	349	16.52.38	-15.307	-178.186	10	5.8
4	FEB 06 2013	037	13.54.54	-10.808	166.526	13.7	5.8
5	FEB 06 2013	037	22.20.20	-11.099	165.632	24.5	5.6
6	FEB 23 2013	054	08.59.08	-10.660	165.304	12	6.1
7	JUL 08 2013	189	02.13.40	-8.803	113.002	60	5.7
8	JUL 16 2013	197	09.35.53	-6.288	154.768	40	5.9
9	OCT 16 2013	289	10.31.01	-6.490	154.920	58.2	7.1



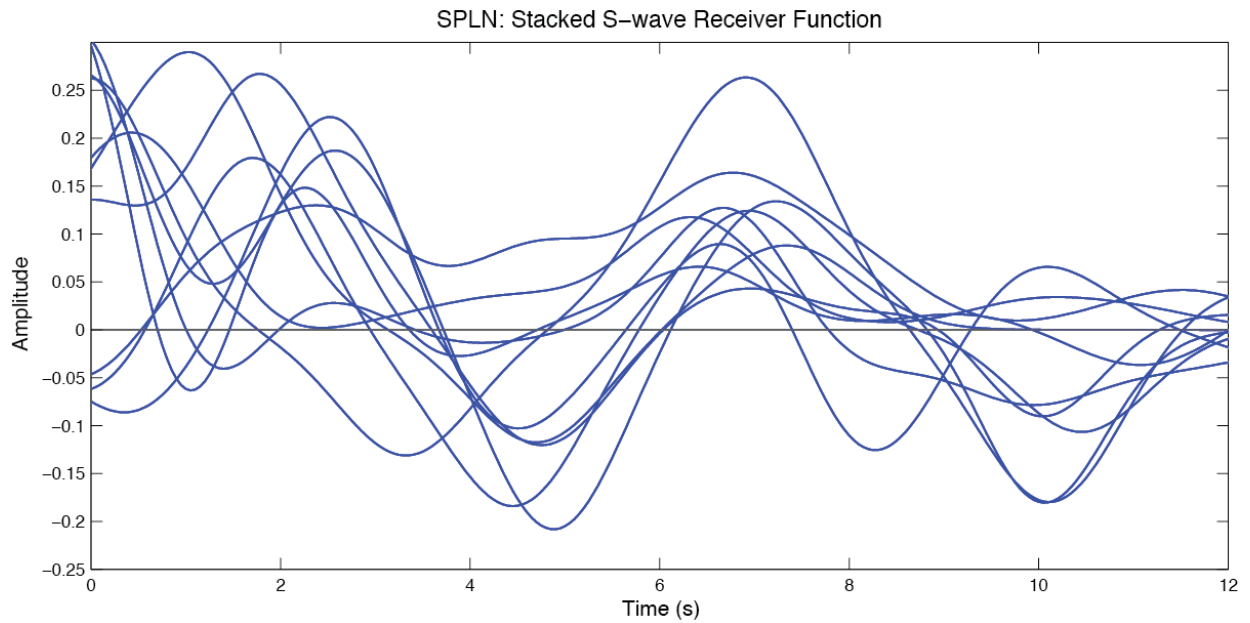
SAMH Event #	Date	Julian day	Time	Latitude (°)	Longitude (°)	Depth km	Mag.
1	DEC 08 2012	343	16.35.16	-7.211	143.973	10	5.6
2	DEC 28 2012	363	17.32.18	-14.500	122.918	112.1	5.5
3	FEB 23 2013	054	14.31.03	-11.689	165.023	10	5.6
4	APR 14 2013	104	01.32.22	-6.475	154.607	31	6.5
5	APR 19 2013	109	17.51.41	-11.976	121.632	15.2	5.8
6	JUL 08 2013	189	02.13.40	-8.803	113.002	60	5.7
7	AUG 12 2013	224	00.53.43	-7.147	129.813	95	6.1
8	SEP 05 2013	248	15.27.02	-7.240	144.057	7.3	5.5
9	OCT 16 2013	289	10.31.01	-6.490	154.920	58.2	7.1
10	OCT 31 2013	304	23.03.56	-30.314	-71.733	10.7	6.6
11	NOV 03 2013	307	02.42.54	-5.885	148.799	88.8	5.6



SHRD Event #	Date	Julian day	Time	Latitude (°)	Longitude (°)	Depth km	Mag.
1	DEC 10 2012	345	16.53.08	-6.533	129.825	155	7.1
2	DEC 29 2012	364	07.59.41	-3.563	148.899	40	6.0
3	FEB 07 2013	038	00.30.10	-11.658	164.940	8	6.0
4	APR 16 2013	106	22.55.26	-3.214	142.542	13	6.6
5	MAY 17 2013	137	06.43.15	-11.066	165.080	7	5.7
6	JUN 19 2013	170	06.52.38	-3.766	151.400	10	5.5
7	JUN 24 2013	175	08.01.39	-6.453	148.684	10	5.7
8	JUN 24 2013	175	09.55.44	-6.446	148.576	28.9	5.7
9	JUL 06 2013	187	05.05.06	-3.269	100.564	21	6.0
10	JUL 16 2013	197	09.35.53	-6.288	154.768	40	5.9
11	SEP 01 2013	244	11.52.29	-7.437	128.218	112	6.5
12	NOV 19 2013	323	13.32.54	2.646	128.402	63.5	6.3



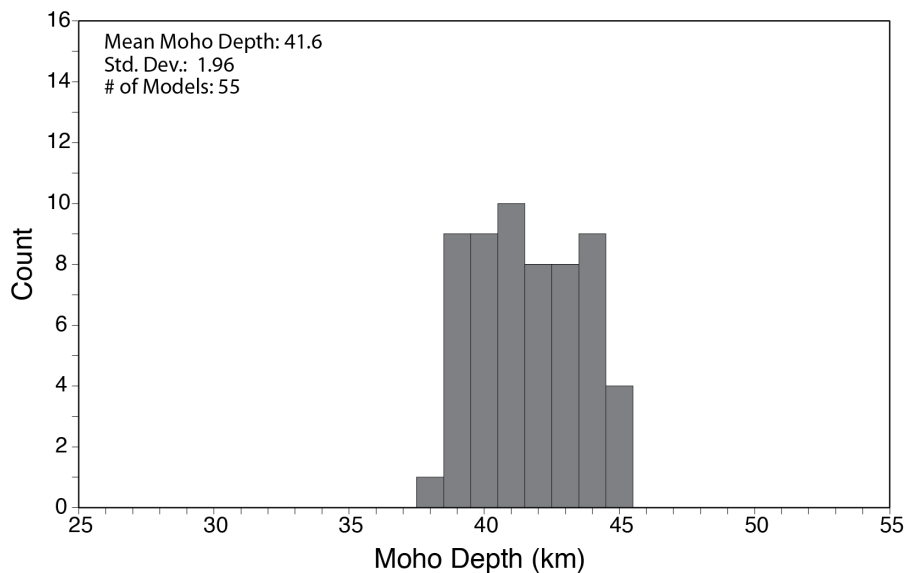
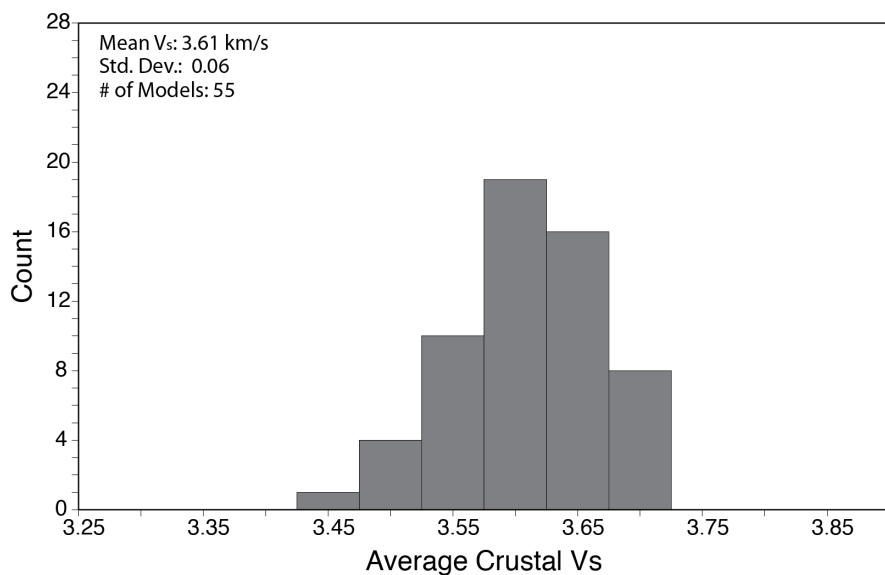
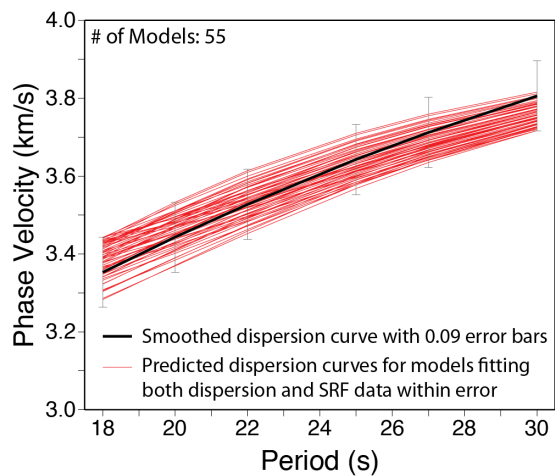
SPLN Event #	Date	Julian day	Time	Latitude (°)	Longitude (°)	Depth km	Mag.
1	DEC 08 2012	343	16.35.16	-7.211	143.973	10	5.6
2	DEC 10 2012	345	16.53.08	-6.533	129.825	155	7.1
3	DEC 28 2012	363	17.32.18	-14.500	122.918	112.1	5.5
4	FEB 02 2013	033	04.16.17	-10.956	165.357	22.2	5.9
5	FEB 10 2013	041	01.30.46	-11.012	166.788	10	5.6
6	FEB 13 2013	044	10.08.50	-10.789	164.255	19.8	5.5
7	FEB 23 2013	054	11.09.19	-8.467	127.467	20	5.9
8	APR 19 2013	109	17.51.41	-11.976	121.632	15.2	5.8
9	JUN 26 2013	177	22.59.00	-0.041	125.054	32.7	5.5
10	JUL 09 2013	190	17.04.15	-3.359	100.458	17.5	5.5



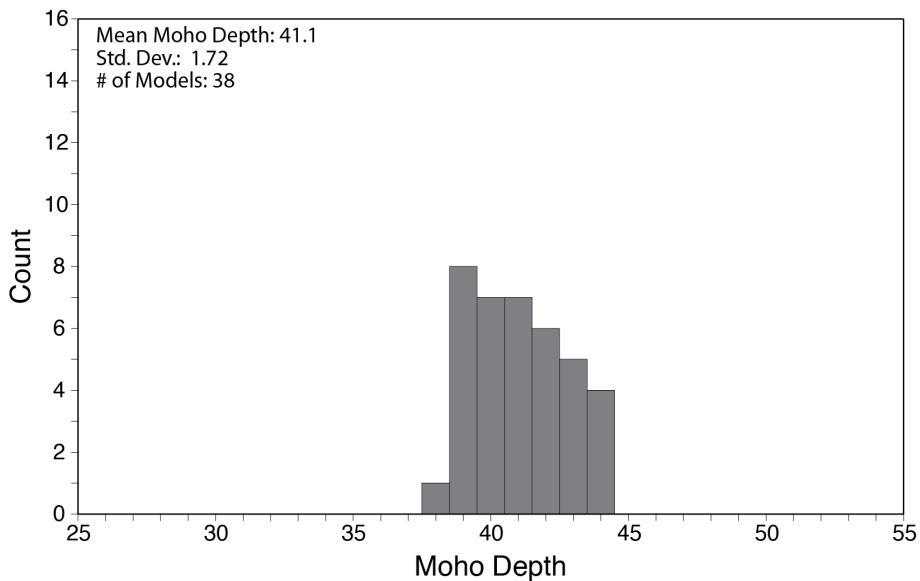
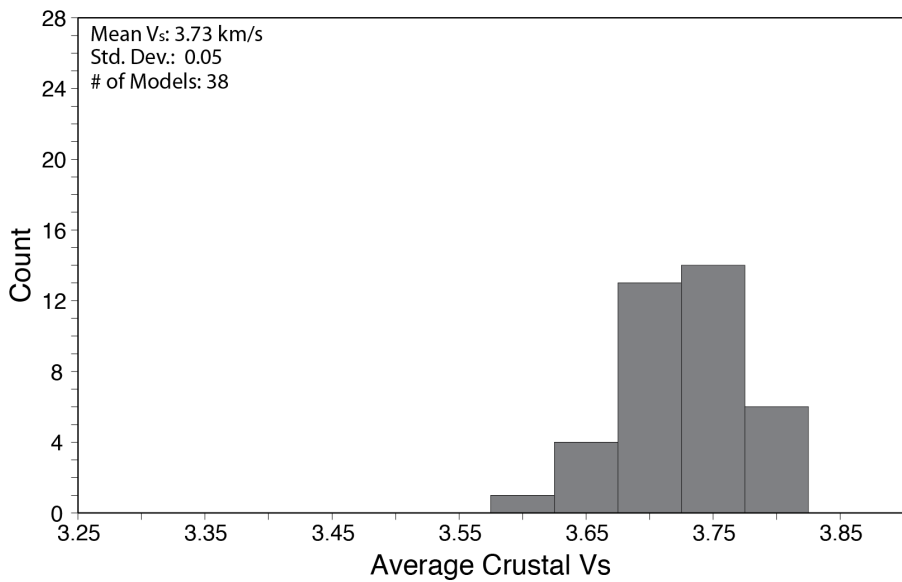
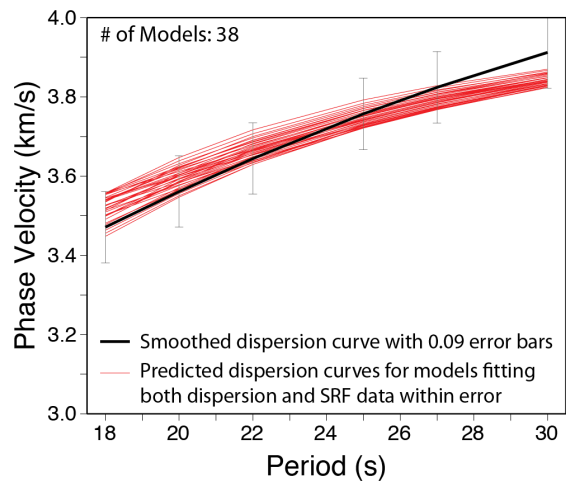
APPENDIX B

This appendix contains the data modeling and grid search results, similar to Figure 10, but for all analyzed stations. Each following page includes three panels. The top panel shows predicted Rayleigh wave phase velocity dispersion curves (red lines) for models that fit both the smoothed dispersion data (black line with error bars; Graw et al., 2014) and the Moho S-to-P conversion time from the stacked SRFs (Fig. 8). The middle panel shows a histogram plot of all average crustal S-wave velocities encompassed by the “fit” models, with the mean V_s , standard deviation, and number of models indicated in the upper left corner. Similarly, the bottom panel shows a histogram plot of all Moho depths (including ice thickness) encompassed by the “fit” models, again with the mean value, standard deviation, and the number of the models indicated on the upper left. Stations are shown in alphabetical order, except for station FOOT, which is shown in Figure 10.

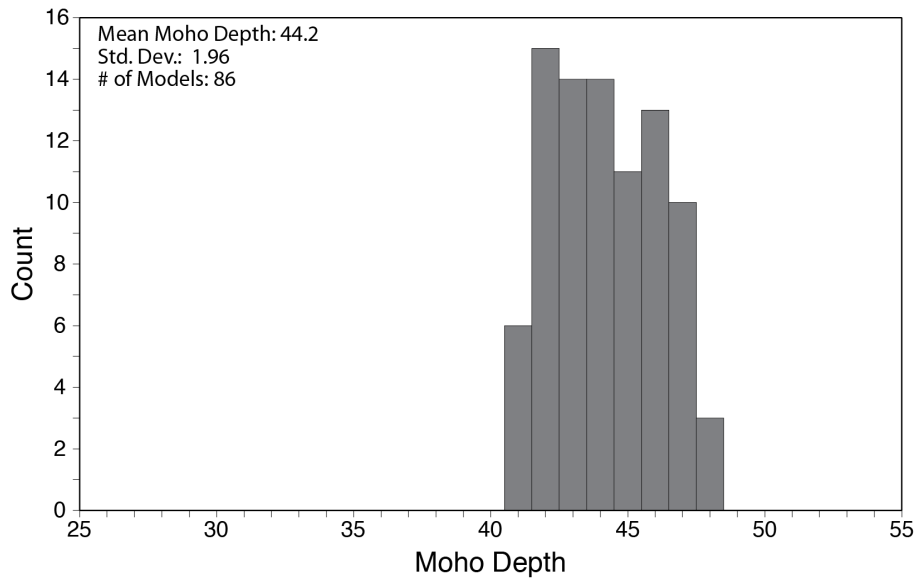
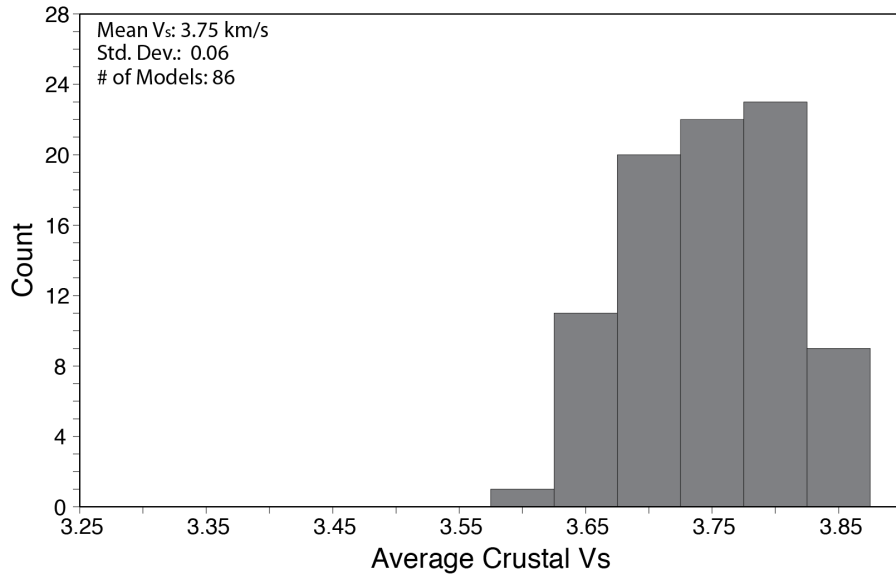
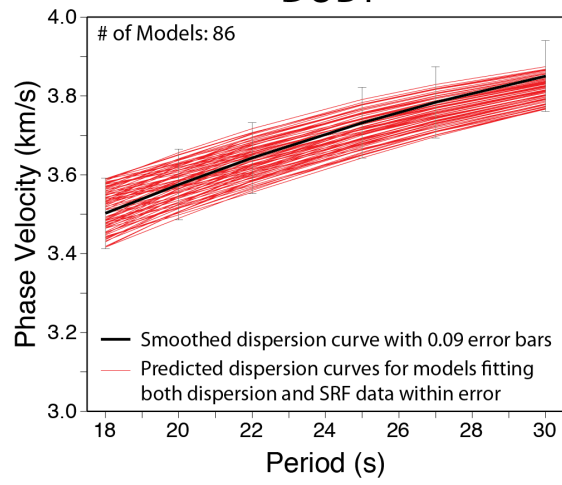
APRL



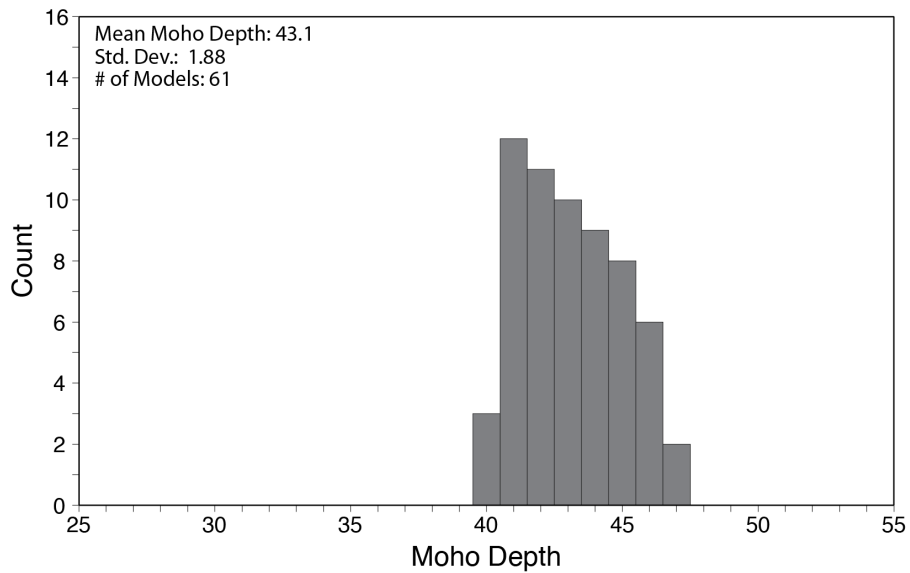
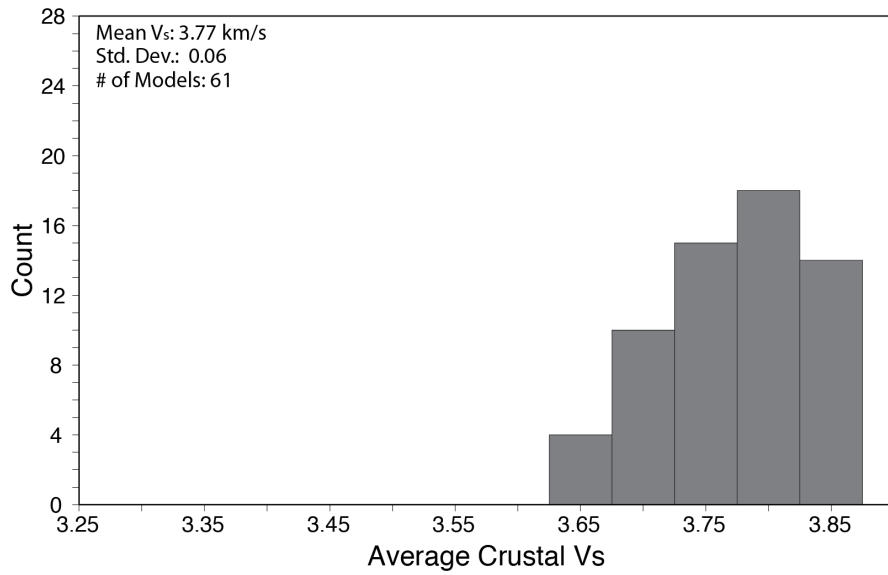
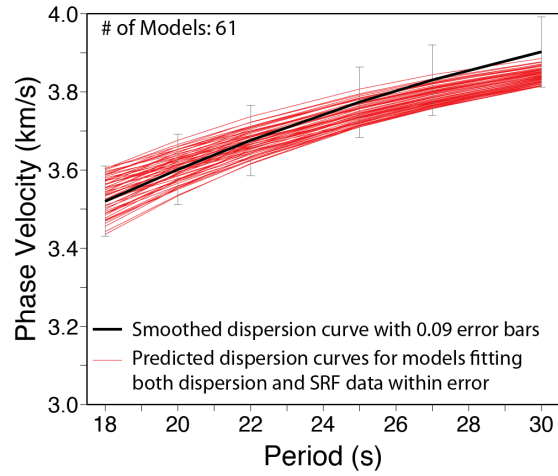
BEBP



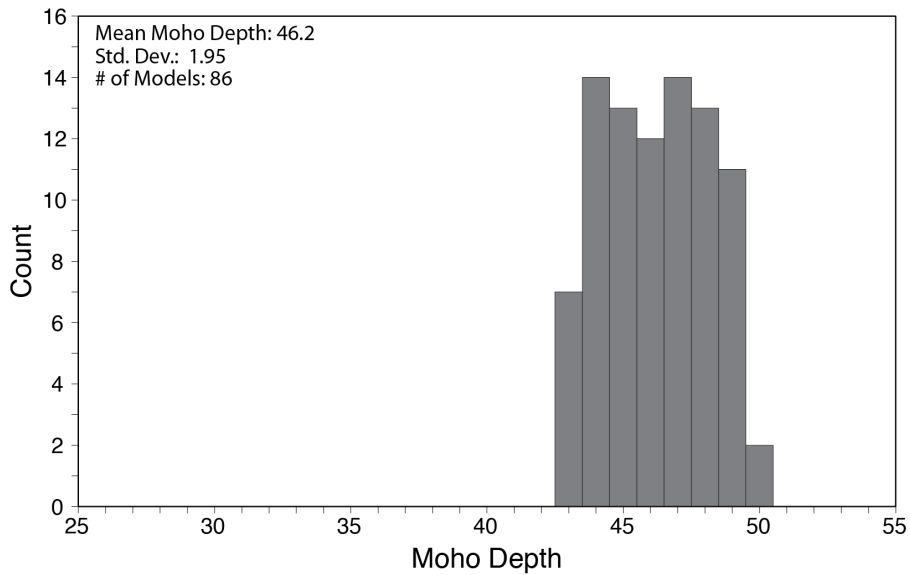
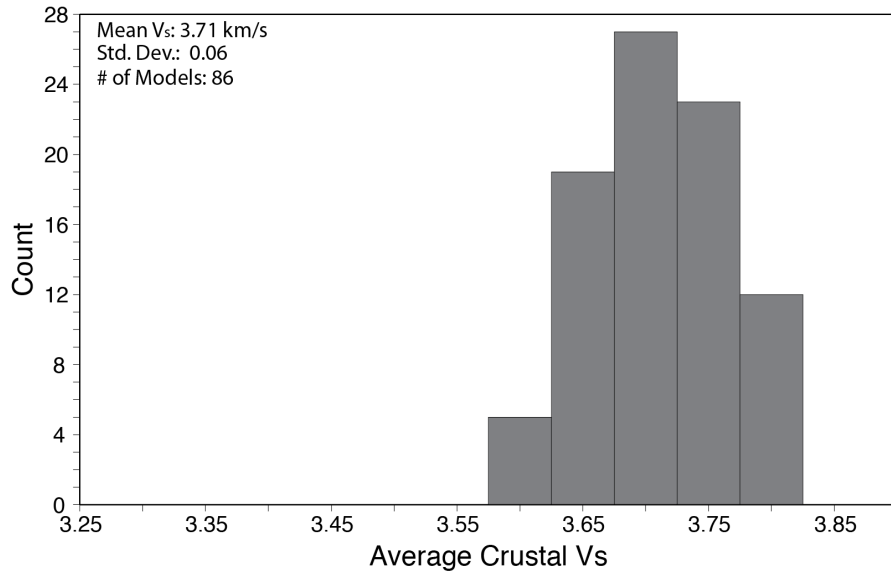
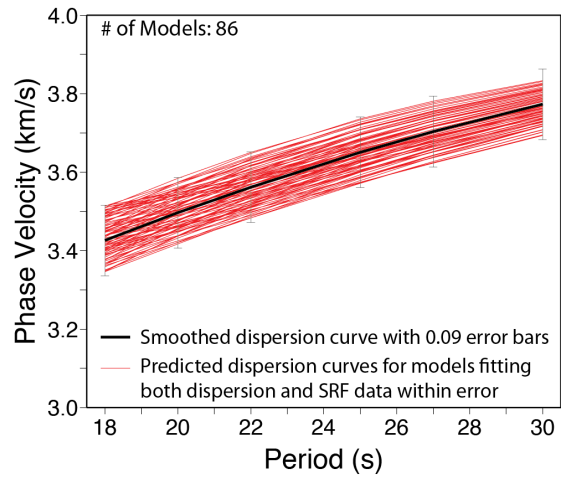
DUBY



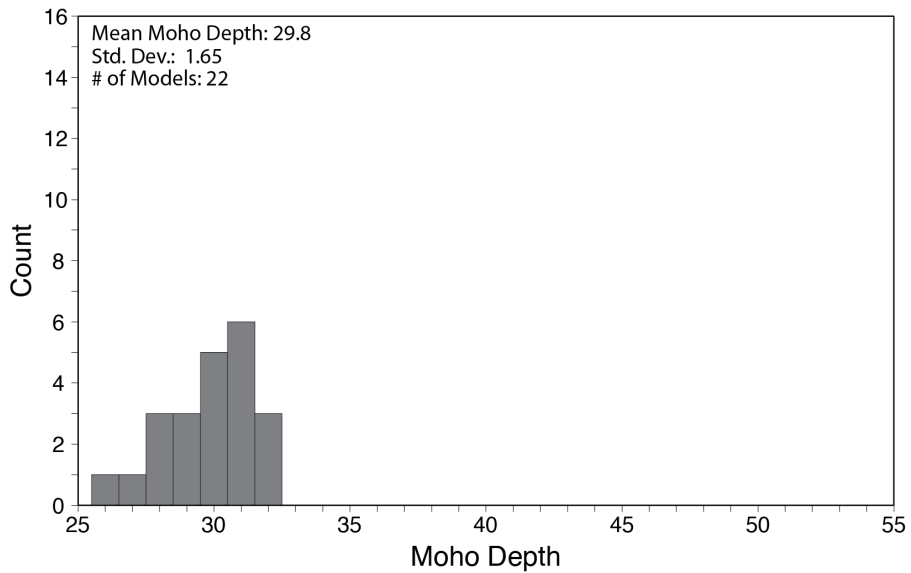
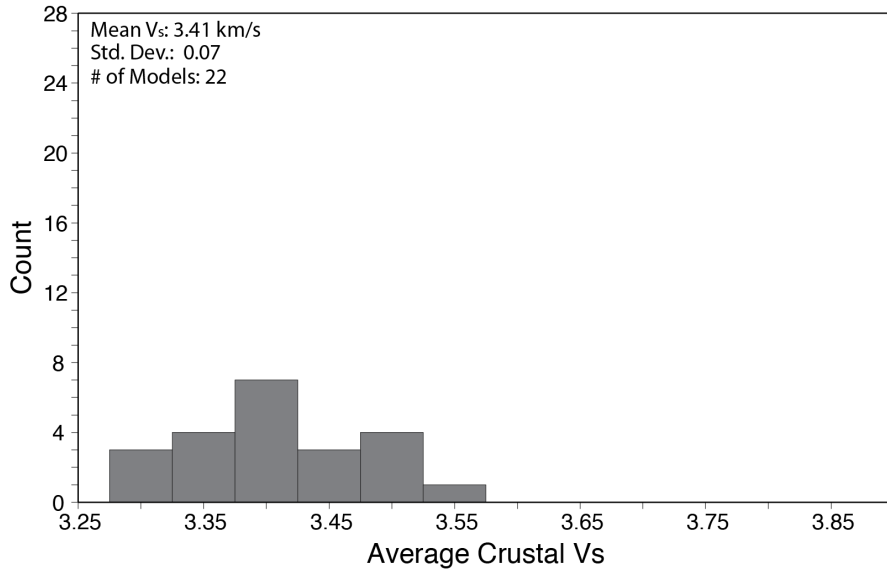
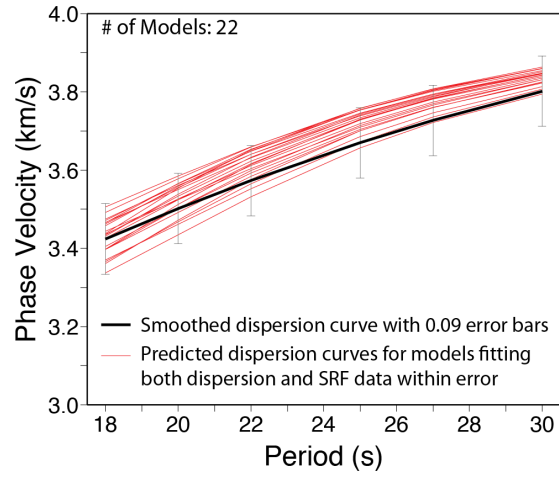
GRAW



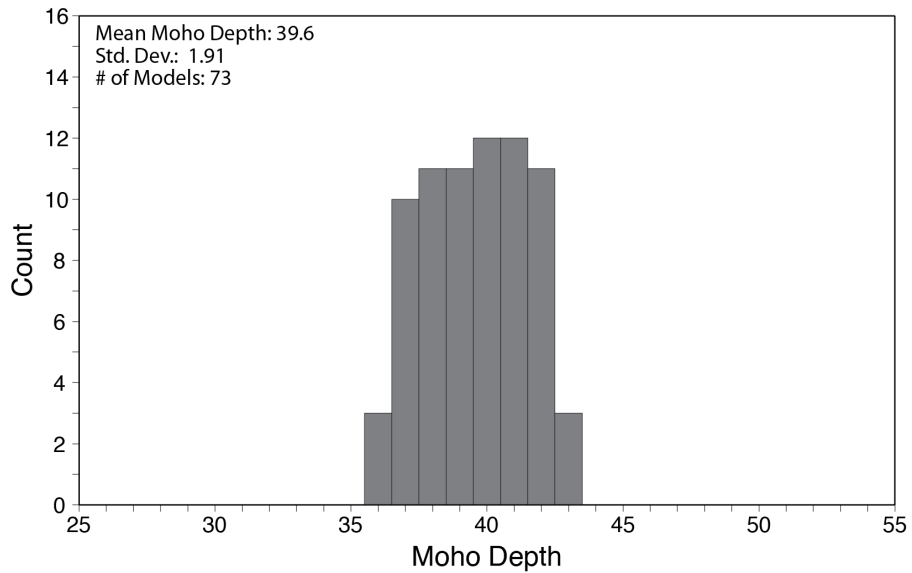
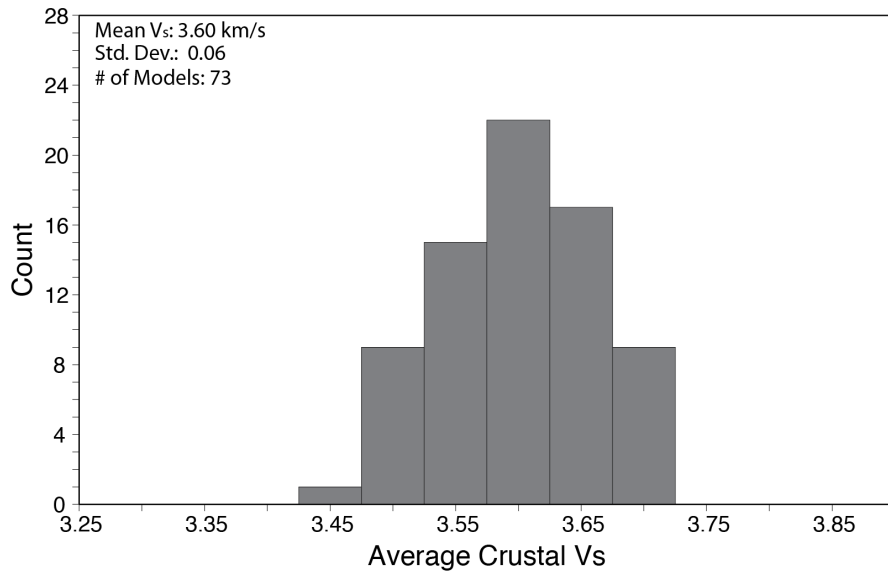
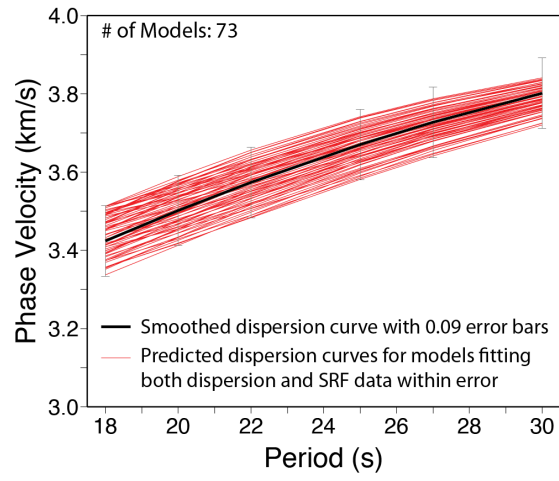
KNYN



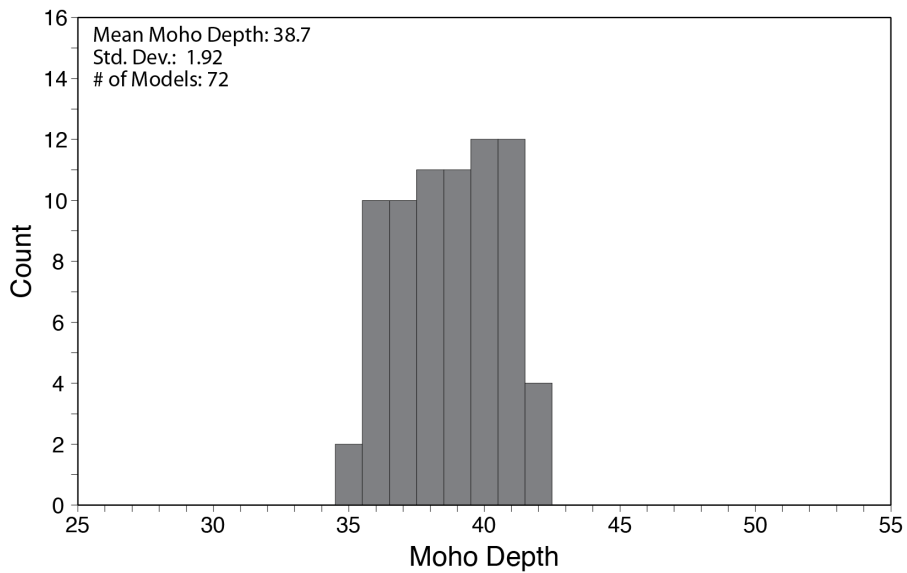
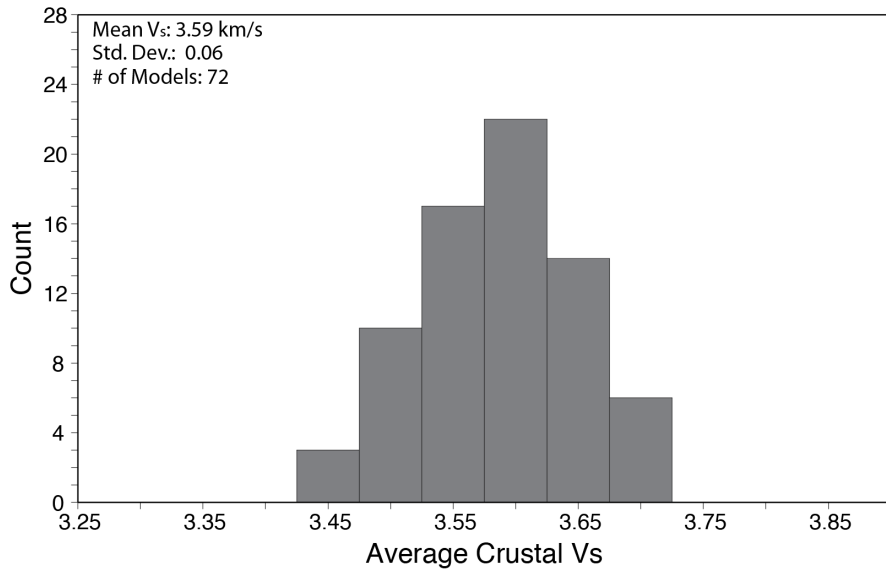
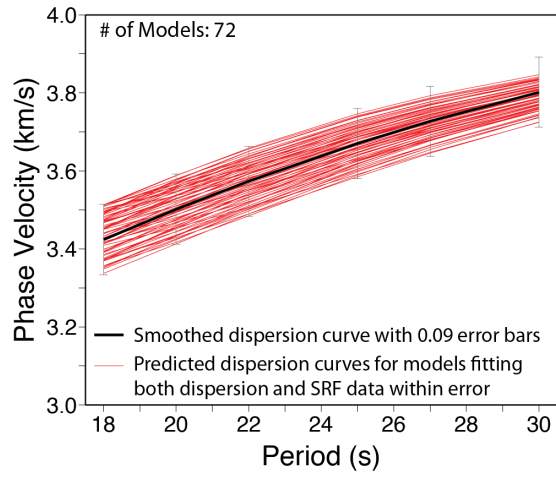
KP01



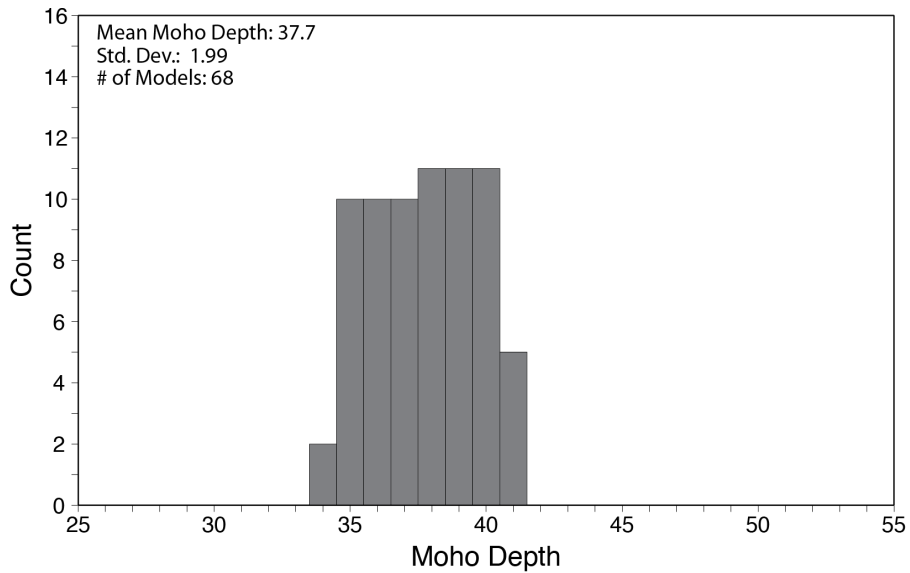
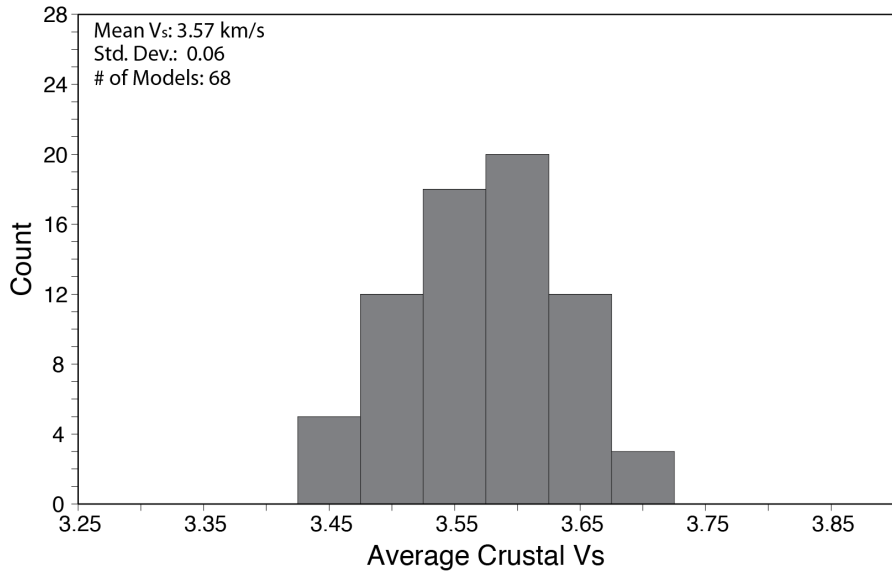
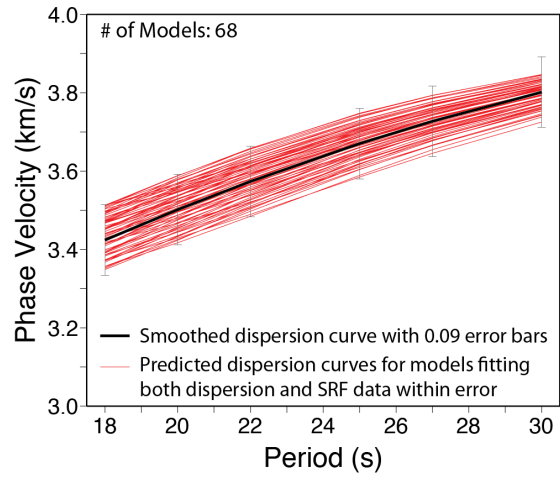
KP02



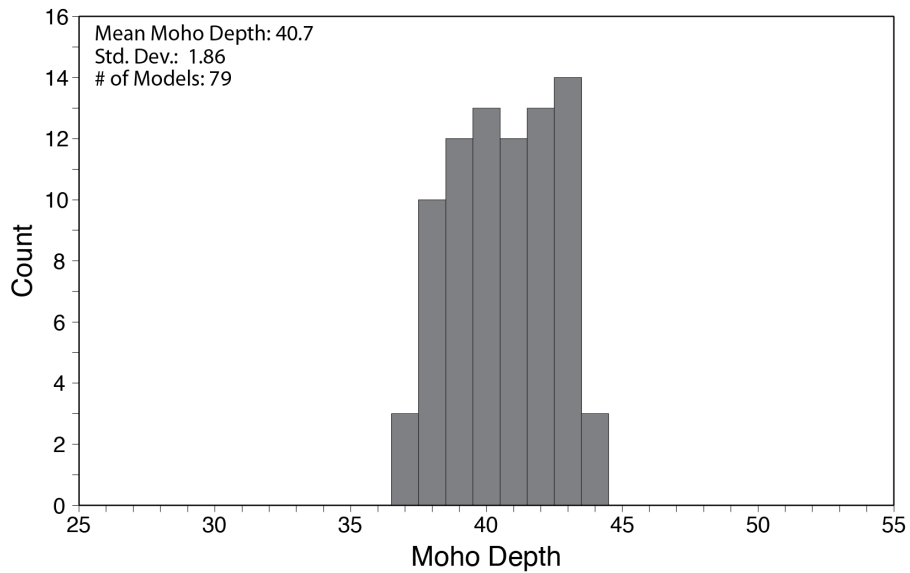
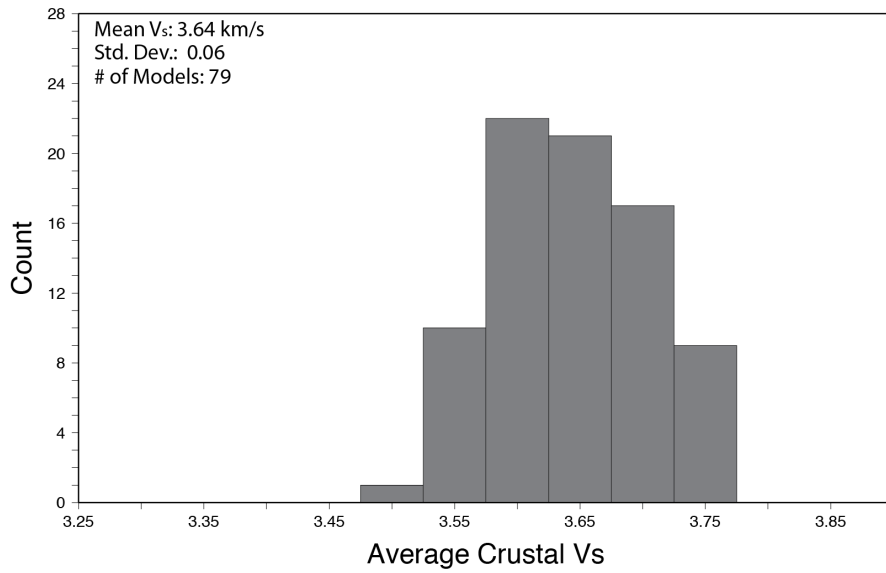
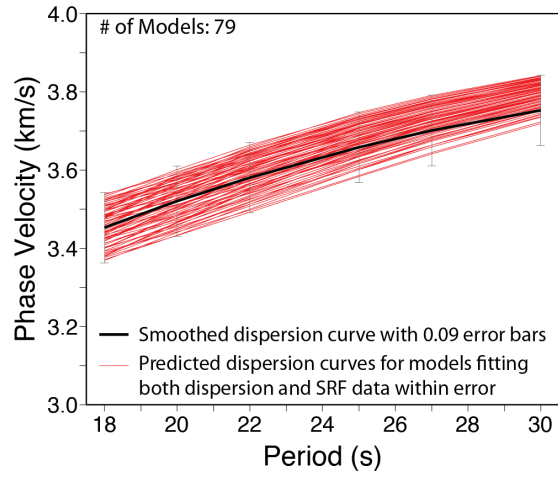
KP03



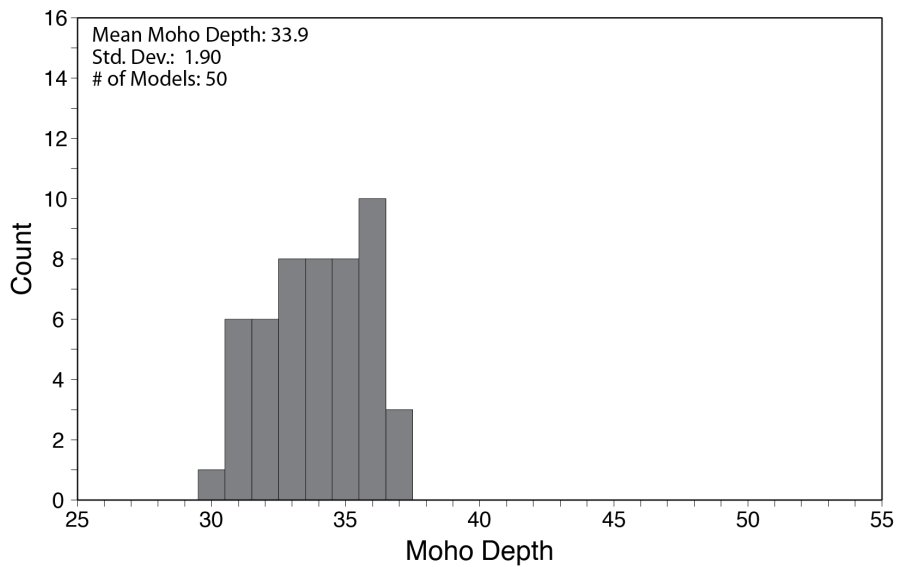
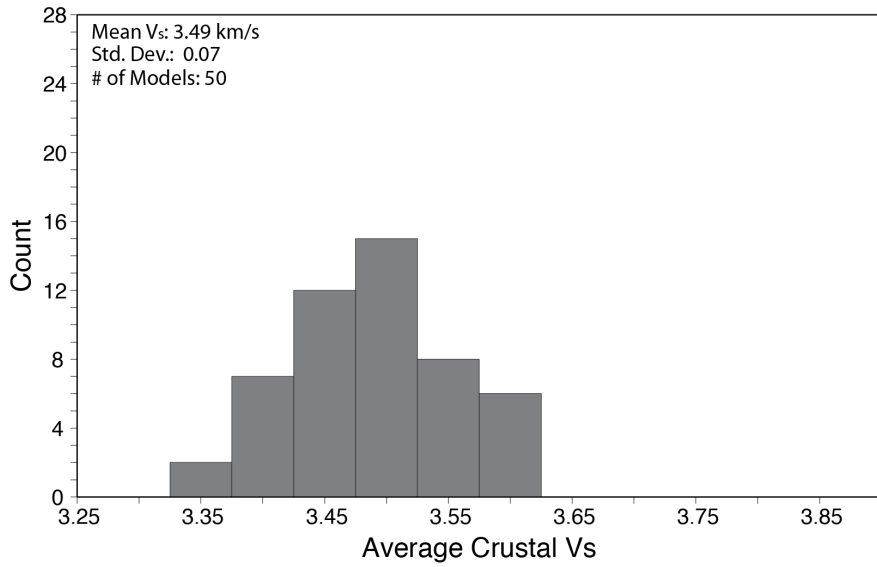
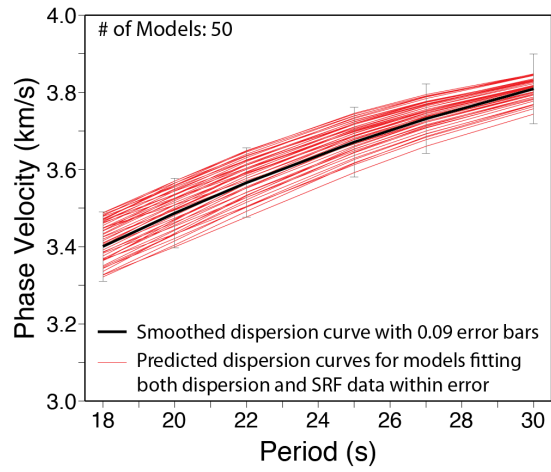
KP04



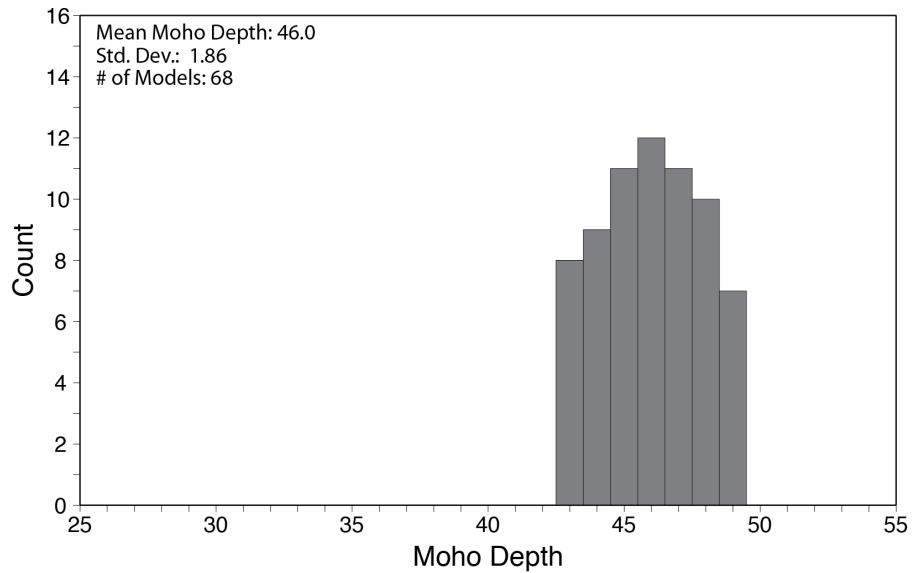
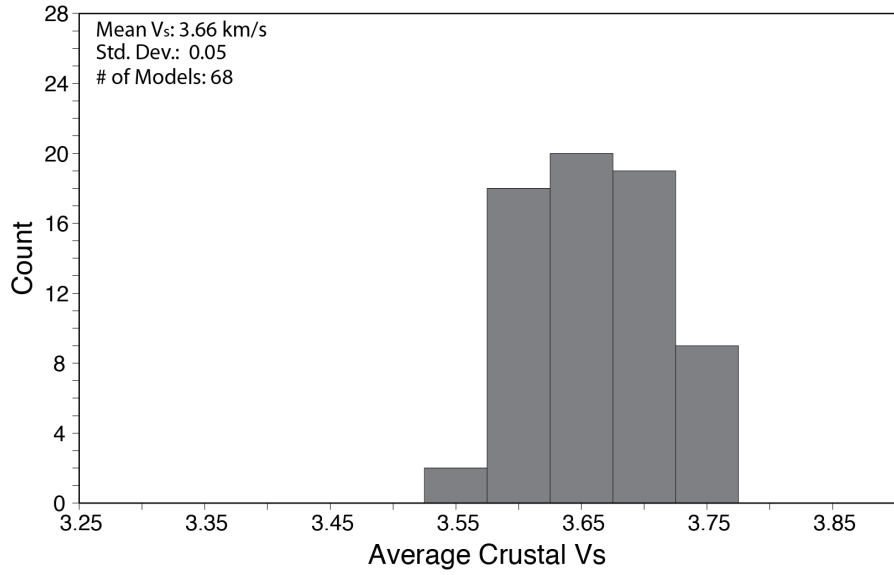
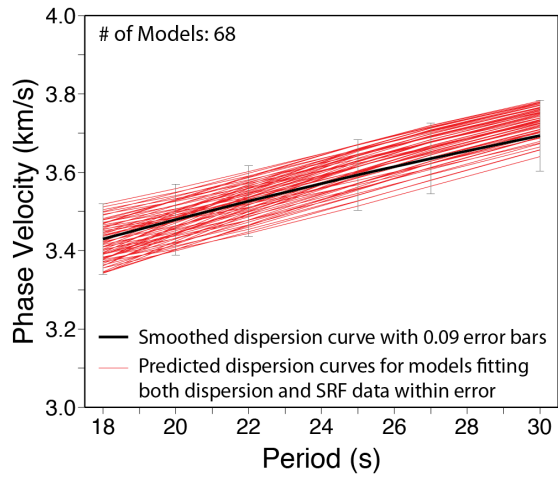
LEON



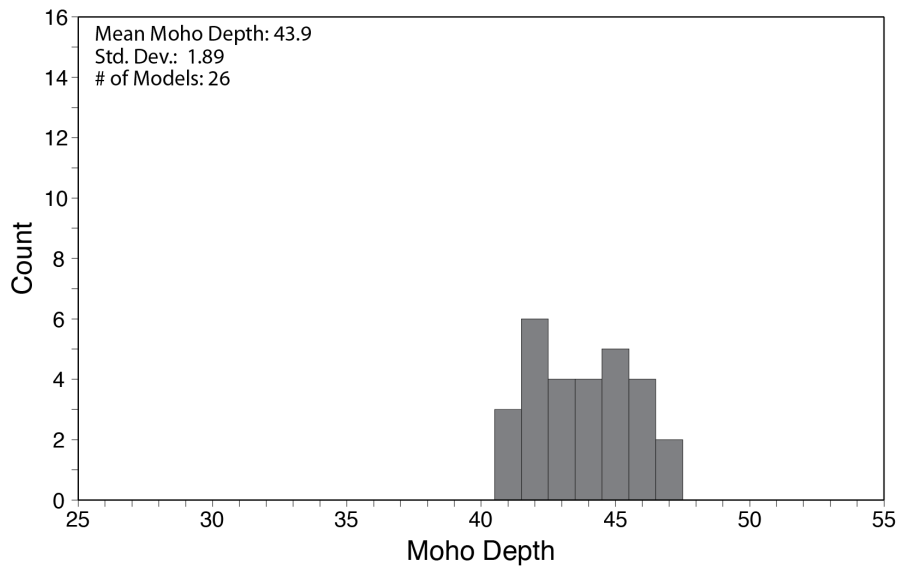
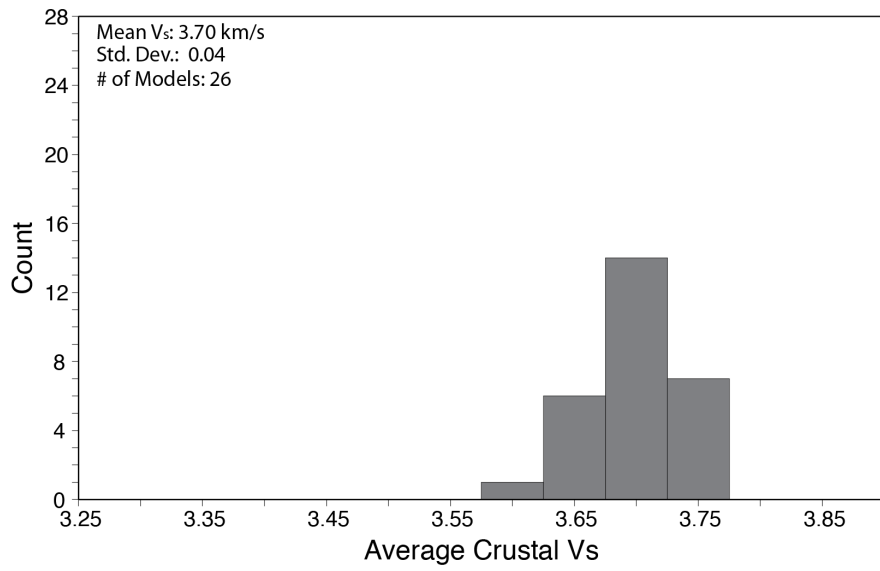
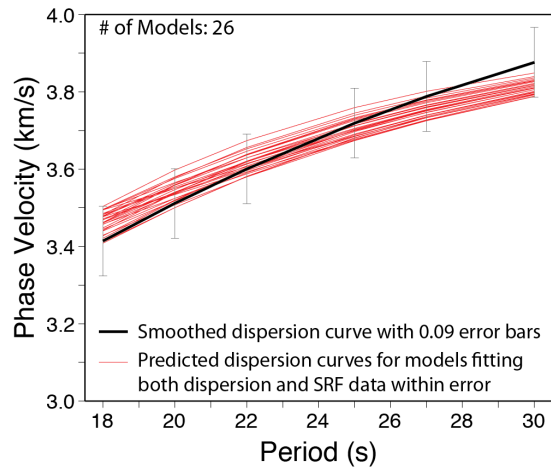
MICH



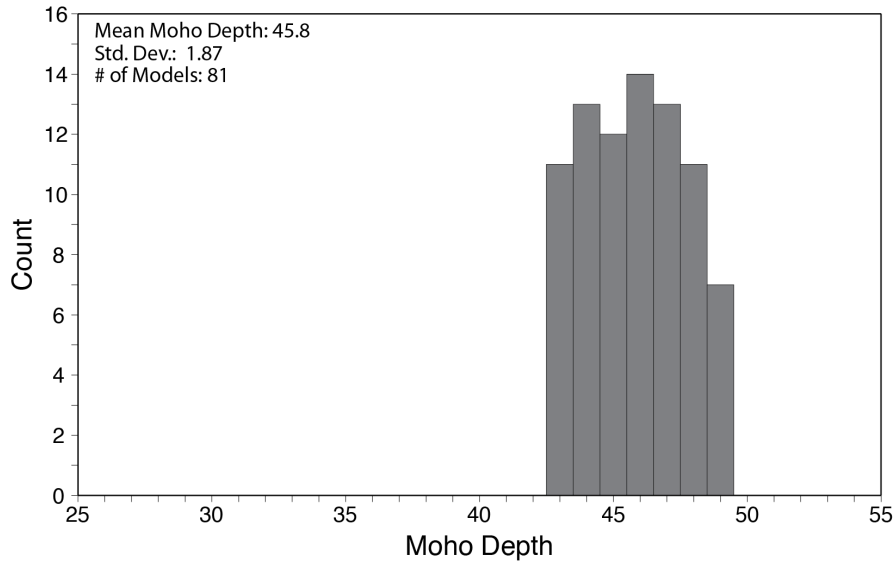
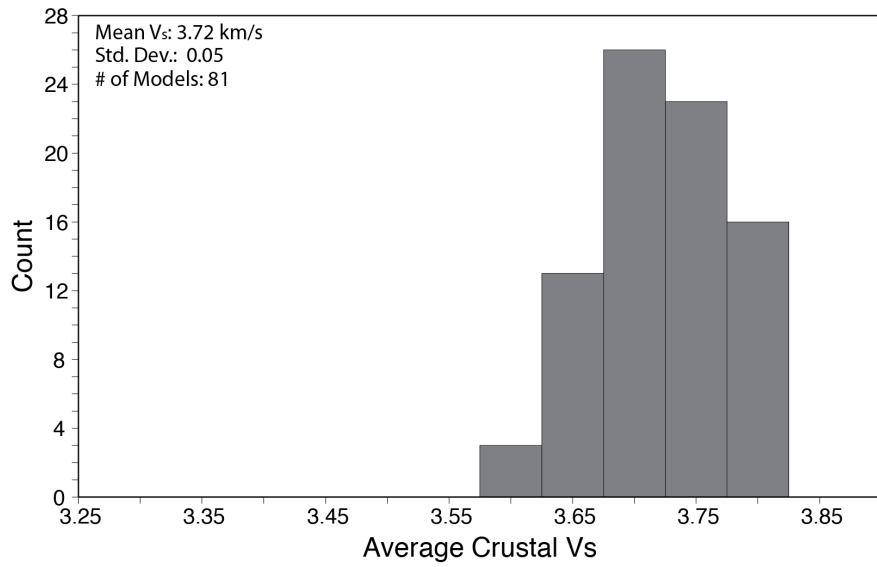
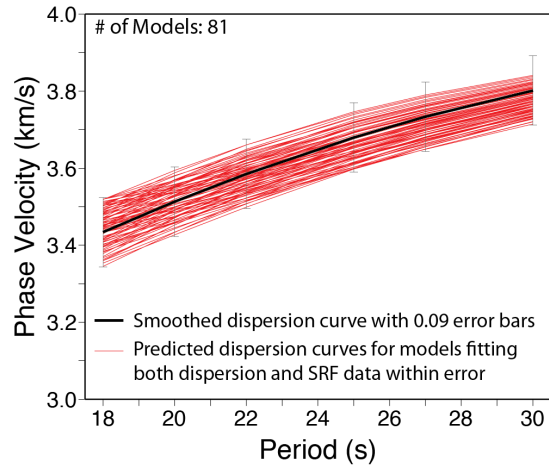
RAPH



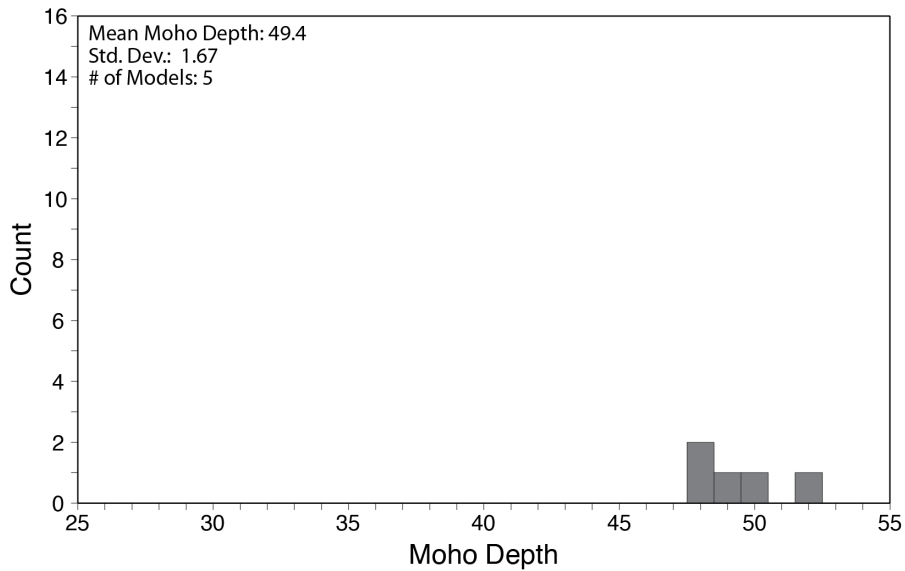
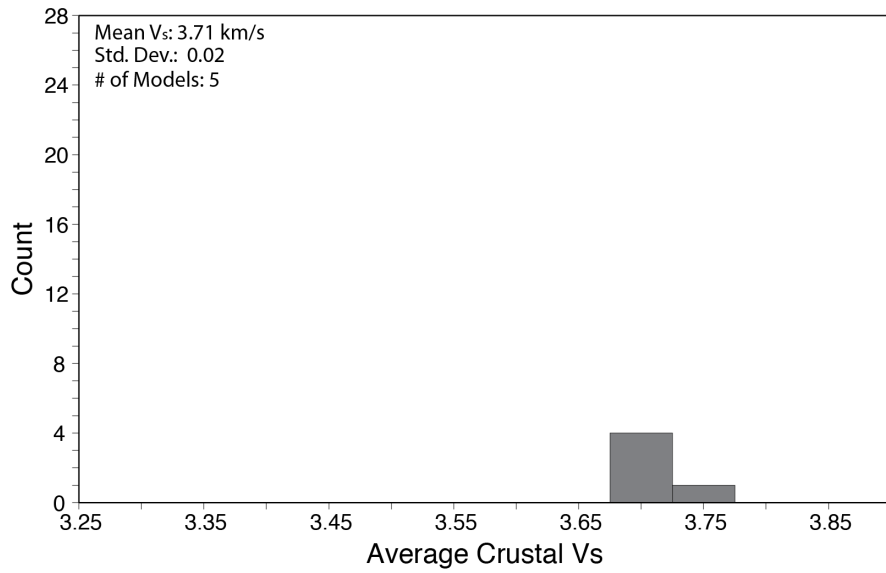
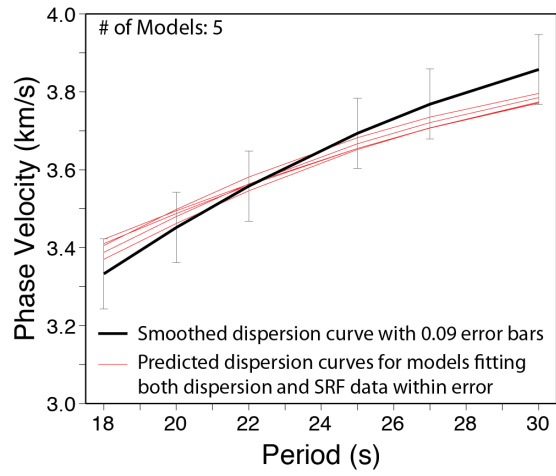
RKST



SAMH



SHRD



SPLN

